THÈSE POUR OBTENIR LE GRADE DE DOCTEUR
DE L'UNIVERSITÉ DE MONTPELLIER

En Physique

École doctorale Information, Structure et Systèmes (I2S)

Unité de recherche UMR5221

Deep-UV hyperspectral microscopy of hexagonal boron nitride : from monolayer to polytypes

Présentée par Adrien ROUSSEAU
Le 08 décembre 2023

Sous la direction de Guillaume CASSABOIS
et Bernard GIL

Devant le jury composé de

TALIERCIO Thierry, Professeur, IES-Montpellier	Président du jury
ZOBELLI Alberto, Maître de conférences, LPS-Paris	Rapporteur
BAUDIN Emmanuel, Maître de conférences, LPENS-Paris	Rapporteur
JAMET Matthieu, Ingénieur, CEA-Grenoble	Examinateur
CASSABOIS Guillaume, Professeur, L2C-Montpellier	Directeur de thèse
GIL Bernard, Directeur de recherche, L2C-Montpellier	Membre invité

UNIVERSITÉ
DE MONTPELLIER

À ma femme, Daria, et à mes parents.

Acknowledgments

This thesis represents the culmination of three amazing years at the *Laboratoire Charles Coulomb* in Montpellier, where I had the privilege to work and interact with outstanding people, both scientifically and humanely. Notably, I had the great chance to be a member of the S2QT team, which is like a family, with whom I shared many memorable moments, including picnics in the sun, beer times, and cake times. The unique atmosphere within the team makes it an ideal working and learning environment where going to work is a pleasure.

First and foremost, I would like to extend my warmest thanks to my two supervisors and mentors, Bernard Gil and Guillaume Cassabois, for their patience, kindness, scientific expertise, and all the discussions through which I have learned so much. Thank you, Guillaume, for trusting me and supporting me throughout these years since the M1 in Nanosciences, and for giving me the opportunity to pursue this doctorate with you. Thank you, Bernard, for your kindness and generosity, for providing me with the opportunity to participate in numerous conferences or research works, and for introducing me to the wonderful group theory. My thanks also go to research engineer Pierre Valvin, with whom I worked closely on the UV microscope, who shared with me his vast knowledge of optics and his passion for astronomy, and who had to put up with my bubbling impulsiveness. It was a real pleasure to work alongside you, and I still remember our stormy discussions around the board.

Secondly, I'd like to thank all the members of the S2QT team, with whom I've had a wonderful time, starting with my PhD and postdoc colleagues and friends. Alrik Durand, who trained me in coding, and with whom we had a lot of great times, in bars, at teknivals, and on the beaches of the Landes. Yohan Baron and his hilarious third degree. The S2QTroll team, Florentin Fabre and Maxime Rollo, whose grotesque pranks brought joy and good humor to the team. The relief of the UV team, Juliette Plo and Alexandre Ibanez, as well as Félix Cache, Tristan Clua-Provost, Elias Sfeir, Zhao Mu, and Pawan Kumar. Finally, I'd like to thank the permanent staff, Anaïs Dréau, Vincent Jacques, Isabelle Philip and Aurore Finco.

Furthermore, this thesis would not have been possible without the many scientific collaborations around the world, so many thanks to James H. Edgar, Sergei Novikov, Jong Kyu Kim, Andrzej Wysmolek, and Johannes Binder. I'd also like to thank all the staff at the *Laboratoire Charles Coulomb* and IES with whom I interacted or collaborated closely during my thesis. So

a big thanks to Mathieu Moret, Wilfried Desrat, Sebastien Nanot, Adrien Noury, Thierry Guillet, Thierry Michel, Christian Lhenoret, Thomas Cohen, Michel Ramonda, Khalid Dinar and Hassen Souissi, for their collaboration and scientific advice. Thanks also to the L2C administrative department, notably Béatrice Tomberli, Jean-Christophe Art, and Stéphanie Martegoutes, and to the management, Pierre Lefebvre and Elodie Gayet, notably for enabling us to set up the non-permanent days. Thanks to Lucyna Firlej of the I2S doctoral school. Finally, a big thank you to my thesis jury, Thierry Taliercio, Alberto Zobelli, Emmanuel Baudin, and Mathieu Jamet, for their feedback and question session.

Finally, I'd like to extend my eternal thanks to my parents and family, who have supported me throughout all these years of study. I would like to end this long list by thanking the woman of my life, the one who is constantly by my side and who supported me by here unfailing love, my wife Daria.

Contents

Contents ii

Introduction 3

1 Fundamentals 7
- 1.1 Monolayer hBN . . . 8
  - 1.1.1 Microscopic structure and symmetries . . . 8
  - 1.1.2 Vibrational properties . . . 10
  - 1.1.3 Electronic properties . . . 11
  - 1.1.4 Optical properties . . . 12
- 1.2 hBN polytypes . . . 15
  - 1.2.1 Microscopic structures and symmetries . . . 15
  - 1.2.2 Vibrational properties . . . 20
  - 1.2.3 Electronic properties . . . 23
  - 1.2.4 Optical properties . . . 25
- 1.3 Conclusion . . . 29

2 Hyperspectral microscopy in the deep-UV 31
- 2.1 Context . . . 31
  - 2.1.1 Luminescence microscopy in the deep-UV . . . 31
  - 2.1.2 Physical processes . . . 34
- 2.2 Deep-UV microscope . . . 37
  - 2.2.1 Deep-UV excitation . . . 37
  - 2.2.2 Sample cryogenic environment . . . 39
  - 2.2.3 Signal collection and detection . . . 43
  - 2.2.4 Software control and hyperspectral acquisition . . . 44
- 2.3 Conclusion . . . 46

3 Monolayer hBN 47
- 3.1 Optical properties of monolayer hBN . . . 47
- 3.2 Exfoliated monolayer hBN . . . 51
  - 3.2.1 Sample topography . . . 51
  - 3.2.2 Hyperspectral imaging in the deep-UV . . . 54

3.2.3 Indirect bandgap emission in few-layer hBN . . . 56
3.3 Epitaxial monolayer hBN . . . 59
3.3.1 Samples topography . . . 59
3.3.2 Hyperspectral imaging in the deep-UV . . . 61
3.4 Direct bandgap emission in monolayer hBN . . . 66
3.4.1 Model . . . 66
3.4.2 Epitaxial monolayer hBN . . . 67
3.4.3 Exfoliated monolayer hBN . . . 73
3.4.4 The origin of the PL doublet . . . 75
3.5 Conclusion . . . 76

4 Bernal boron nitride **79**
4.1 hBN polytypes in the literature . . . 79
4.2 Optical identification of a AB-hBN crystal . . . 83
4.2.1 Macroscopic characterization . . . 83
4.2.2 Microscopic characterization . . . 87
4.3 Optical properties of AB-hBN . . . 92
4.3.1 Direct and indirect bandgap emission . . . 92
4.3.2 The polariton effect in AB-hBN . . . 95
4.3.3 Thermal broadening . . . 97
4.3.4 Deep levels emission in the UVB . . . 102
4.4 Conclusion . . . 107

Bibliography **112**

Abstract **121**

Publications

- **Determination of the optical bandgap of the Bernal and rhombohedral boron nitride polymorphs**
  Physical Review Materials, **5**(6):064602 (2021).
  Adrien Rousseau, Matthieu Moret, Pierre Valvin, Jiahan Li, Eli Janzen, Lianjie Xue, James Howard Edgar, and Guillaume Cassabois.

- **Hexagonal boron nitride: optical properties in the deep ultraviolet**
  Comptes Rendus. Physique, **22**(S4):69-76 (2021).
  Guillaume Cassabois, **Adrien Rousseau**, Christine Elias, Thomas Pelini, Phuong Vuong, Pierre Valvin, Bernard Gil.

- **Monolayer Boron Nitride: Hyperspectral Imaging in the Deep Ultraviolet**
  Nano Letters, **21**(23):10133–10138 (2021).
  Adrien Rousseau, Lei Ren, Alrik Durand, Pierre Valvin, Bernard Gil, Kenji Watanabe, Takashi Taniguchi, Bernhard Urbaszek, Xavier Marie, Cédric Robert, and Guillaume Cassabois.

- **Rhombohedral and turbostratic boron nitride: X-ray diffraction and photoluminescence signatures**
  Applied Physics Letters, **119**(26):262102, (2021).
  Matthieu Moret, **Adrien Rousseau**, Pierre Valvin, Sachin Sharma, Laurent Souqui, Henrik Pedersen, Hans Högberg, Guillaume Cassabois, Jianhan Li, J. H. Edgar, and Bernard Gil.

- **Bernal Boron Nitride Crystals Identified by Deep-Ultraviolet Cryomicroscopy**
  ACS Nano, **16**(2):2756-2761, (2022).
  Adrien Rousseau, Pierre Valvin, Wilfried Desrat, Lianjie Xue, Jiahan Li, James Howard Edgar, Guillaume Cassabois, and Bernard Gil.

- **Exciton and Phonon Radiative Linewidths in Monolayer Boron Nitride**
  Phys. Rev. X **12**:011057, (2022).
  Guillaume Cassabois, Giorgia Fugallo, Christine Elias, Pierre Valvin, **Adrien Rousseau**, Bernard Gil, Alex Summerfield, Christopher J. Mellor, Tin S. Cheng, Laurence Eaves, C. Thomas Foxon, Peter H. Beton, Michele Lazzeri, Alfredo Segura, and Sergei V. Novikov.

- **Polytypes of sp^2-Bonded Boron Nitride**
  Crystals, **12**(6):782, (2022).
  Bernard Gil, Wilfried Desrat, **Adrien Rousseau**, Christine Elias, Pierre Valvin, Matthieu Moret, Jiahan Li, Eli Janzen, James Howard Edgar, and Guillaume Cassabois.

- **Phonon-assisted broadening in Bernal boron nitride: A comparison between indirect and direct excitons**
  Physical Review B, **106**(3):035203, (2022).
  Adrien Rousseau, Pierre Valvin, Lianjie Xue, Jianhan Li, James Howard Edgar, Bernard Gil, and Guillaume Cassabois.

- **Stacking-dependent deep level emission in boron nitride**
  Physical Review Materials, **6**(9):094009, (2022).
  Adrien Rousseau, Pierre Valvin, Christine Elias, Lianjie Xue, Jianhan Li, James Howard Edgar, Bernard Gil, and Guillaume Cassabois.

- **High p Doped and Robust band structure in Mg-doped Hexagonal Boron Nitride**
  Nanoscale Adv. **5**:3225-3232 , (2023).
  Lama Khalil, Cyrine Ernandes, José Avila, **Adrien Rousseau**, Pavel Dudin, Nikolai D. Zhigadlo, Guillaume Cassabois, Bernard Gil, Fabrice Oehler, Julien Chastea and Abdelkarim Ouerghi.

- **Boron and Nitrogen Isotope Effects on Hexagonal Boron Nitride Properties**
  Adv. Mater. 2023 2306033, (2023).
  Eli Janzen, Hannah Schutte, Juliette Plo, **Adrien Rousseau**, Thierry Michel, Wilfried Desrat, Pierre Valvin, Vincent Jacques, Guillaume Cassabois, Bernard Gil, James Howard Edgar.

Introduction

In the current context of pandemic crises and the imperative to phase out mercury-based lamps from the market due to their toxicity, there is a growing demand for the development of mercury-free large-scale and low-cost light emitters operating in the ultraviolet (UV) for harmless and efficient bacterial and virus disinfection [1–4]. However, the well-established AlGaN technology at the heart of most UV optoelectronics faces a significant drop in efficiency below wavelength of ∼250 nm [5]. Alternatively, hexagonal boron nitride (hBN) is a wide bandgap semiconductor exhibiting robust emission at a typical wavelength of ∼210 nm, emerging as a pivotal material for future deep-UV optoelectronic applications [6–8].

hBN is a graphite-like lamellar material that consists of weakly stacked honeycomb atomic layers of tightly bound boron and nitrogen atoms, the so-called hBN monolayers [9]. As many other 2D materials, the lamellar structure of hBN offers great flexibility in the atomic configuration allowing layers separation down to a single hBN monolayer or the existence of various stackings leading to the formation of hBN polytypes. The degrees of freedom permitted by the lamellar structure of hBN, namely the reduction of dimensionality and the layers stacking, may influence the hBN properties through the alteration of the crystal symmetry and interlayer coupling, which disappears for a single hBN monolayer. This results in distinctive hBN properties that could be tailored by controlling the thickness and stacking arrangements of hBN layers for specific applications. However, precise control of the properties requires a good understanding of the impact of the structural modifications on the hBN properties and how they can be controlled throughout the fabrication.

One important effect associated with the reduction of dimensionality is the so-called indirect-to-direct bandgap crossover, where the indirect bandgap of a bulk semiconductor becomes direct at the monolayer limit [10]. This results generally in a drastic enhancement of the bandgap emission of monolayers compared to thicker layers, allowing the spatial identification of exfoliated monolayers with typical lateral size of 10-100 µm using spatially-resolved luminescence microscopy [11]. This effect has been observed in many 2D semiconductors including transition metal dichalcogenides (TMDs) or black phosphorus (BP) using photoluminescence (PL) microscopy [11, 12]. Accordingly, spatially-resolved PL microscopy has become a standard approach to study the optical properties of 2D materials. However, due to the technical challenge that represents PL microscopy in the deep-UV, the optical properties of monolayer hBN have

been studied only recently from macroscopic measurements on epitaxial monolayers [13, 14]. Remarkably, the indirect-to-direct bandgap in hBN has been demonstrated by *Elias et al.* on epitaxial monolayers from the absence of stokes shift between the PL signal measured at ∼6.08 eV and the dip in reflectivity associated to the direct bandgap resonance [13]. Yet, our understanding of the optical properties of monolayer hBN remains limited, necessitating PL microscopy in the deep-UV on high-quality exfoliated monolayers, a milestone achieved for the first time in this thesis. A pivotal question arises regarding the origin of the intricate emission profile at approximately ∼6.08 eV in hBN monolayers [15].

The lamellar structure of 2D materials enables the existence of various stackings which can also modify the material properties. Manipulating the stacking of 2D materials has unveiled remarkable properties such as ferroelectricity, superconductivity, and topological effects, offering great flexibility in tailoring 2D material properties, and giving rise to the emerging field of twistronics [16–19]. Moreover, this also leads to polytypism where different stacking orders of the same 2D material may naturally exist under similar conditions, namely the polytypes [20]. Polytypism is observed in various types of materials like SiC [21], II-VI compounds [22], hydroxides complex [23], transition-metal triborides [24], but more importantly in 2D materials including TMDs or graphene [25–29]. This is facilitated by the weak interlayer interaction in 2D materials leading to polytypes with similar formation energy. Polytypes are likely to coexist in 2D materials making the growth of single polytype crystals challenging, where other polytypes may alter their properties. Moreover, a good understanding of the properties and growth conditions of polytypes requires advanced characterization techniques, while conventional techniques like X-ray or Raman spectroscopy could not provide a complete picture due to the structural similarity of polytypes. While hBN is commonly observed in the AA' stacking (AA'-hBN), two other polytypes are predicted to be also stable with similar formation energy, namely rhombohedral boron nitride (ABC-hBN) and bernal boron nitride (AB-hBN) [30, 31]. Furthermore, calculations predict modifications of the optical properties of hBN with hBN polytypes in the deep-UV [32]. Therefore, hBN appears as an ideal platform for studying polytypism in 2D materials. Despite many theoretical studies about polytypism in hBN, there have been very few reports on the identification of high-quality hBN polytype single crystals to date. Consequently, while the optical properties of AA'-hBN have been studied extensively this last decade on high-quality crystals, little is known about the optical properties of other hBN polytypes. Interestingly, the small micrometer size inclusions of hBN polytypes typically observed in polytypic crystals could be studied using spatially-resolved PL microscopy in the deep-UV. Consequently, there is a significant need for PL microscopy in the deep-UV to study the optical properties of both hBN monolayers and polytypes. In the context of polytypes, this could improve our understanding of the impact of stacking on the optical properties of hBN as well as provide novel characterization techniques of hBN polytypes that can be used for monitoring crystal growth.

During my thesis, I developed an original hyperspectral PL microscope operating in deep-UV at cryogenic temperatures (∼4 K) to study the optical properties of hBN monolayers and polytypes. This deep-UV microscope was upgraded from a first version, which had been developed by the former PhD student *Thomas Pelini*, and was operating in the UVB to study deep-level emission around ∼300 nm in hBN [33]. The upgraded version of the microscope reaches a spatial resolution of ∼250 nm in the deep-UV allowing the study of sub-micrometric crystal domains. Furthermore, hyperspectral imaging provides information about the spatial variations of the different spectral components. Finally, the hyperspectral microscope allows to combine PL spectroscopy with other optical techniques, such as second-harmonic generation (SHG) microscopy, providing complementary information about the samples properties. In the first year of my thesis, this microscope has allowed me to study the optical properties in the deep-UV of exfoliated and epitaxial hBN monolayers with a micrometer resolution. This allowed me to unravel and quantitatively describe the coexistence of PL and Raman signals at ∼6.1 eV induced by the quasi-resonant excitation in monolayer hBN. In the second year of my thesis, I used the deep-UV microscope to isolate for the first time a AB-hBN crystal and I performed an in-depth study of its optical properties. I thus unraveled the impact of polytypes on the optical properties of hBN, leading to the emergence of exotic properties in AB-hBN such as the simultaneous direct and indirect bandgap emissions.

Thesis outline

Chapter 1 is dedicated to an overview of the microscopic properties of monolayer hBN and hBN polytypes that will be required to understand the results presented in Chapters 3 and 4, respectively. The properties of hBN polytypes stemming from the ones of the monolayer hBN building block, I first introduce monolayer hBN in Part 1.1 and then hBN polytypes in Part 1.2 where I focus mostly on AA-hBN, AA'-hBN, AB-hBN and ABC-hBN.

Chapter 2 is dedicated to the description of the deep-UV microscope. In Part 2.1, I first introduce the challenge that represents luminescence microscopy in the deep-UV through a state-of-the-art review of the different deep-UV microscopes that have been developed and used over the years, highlighting their main technical limitations (Section 2.1.1). Subsequently, I briefly introduce the main physical processes that will be studied along this thesis via our deep-UV microscope (Section 2.1.2). In Part 2.2, I provide a complete description of the deep-UV microscope that I have developed during my thesis. For each part of the microscope, I address the main technical challenge that I have overcome to obtain the best performance. Finally, the biggest part of my work was to develop a *Python* software that controls the experiments and, notably, enables hyperspectral acquisition and exploration.

Chapter 3 is dedicated to the study of the optical properties of exfoliated (Part 3.2) and epitaxial (Part 3.3) hBN monolayers. My results unravel the coexistence of PL and second-order

Raman signals at ∼6.1 eV induced by the quasi-resonant excitation in hBN monolayers. In Part 3.3, I perform a quantitative analysis of the PL/Raman coexistence by fitting my experimental data from a linear combination of functions representing PL and Raman signals. This quantitative analysis allows me to study how the optical properties of hBN monolayers vary in space and with fabrication. This leads me to a complete and universal description of the emission spectrum at ∼6.1 eV, providing better insight into the long-debated nature of the optical bandgap of monolayer hBN [13, 14, 34].

Chapter 4 is dedicated to the study of the optical properties of a AB-hBN crystal that has been spatially isolated within an hBN flake. In Part 4.2, I demonstrate the spatial isolation of AB-hBN using all-optical techniques combining PL and SHG microscopy. This allows me in Part 4.3 to study for the first time the optical properties of a pure AB-hBN crystal in both deep-UV (UVC) and UVB spectral ranges. In the deep-UV (Section 4.3.1), I unravel the simultaneous observation of direct and indirect bandgap emissions in AB-hBN that I explain by the quasi-degeneracy of the fundamental direct and indirect excitons which was predicted by *ab initio* calculations. In Section 4.3.3, I study the dependence on temperature of the direct and indirect bandgap emission in AB-hBN which present very different thermal broadening, that I explain by the effect of the strong light-matter coupling on the phonon-dephasing processes. Finally, in Section 4.3.4, I study the deep-level emission in the UVB associated with the so-called "4.1 eV defect" in hBN that allows me to conclude on the potential microscopic nature of this defect that appears to be influenced by the stacking.

Chapter 1

Fundamentals

Boron nitride (BN) is a III-V compound semiconductor made of a stoichiometric distribution of B and N atoms which can crystallize into various polymorphs, illustrated in Fig.1.1, that consist of either sp^2 or sp^3 hybridized atomic bonds. The most stable sp^3 hybridized polymorph is cubic boron nitride (cBN) which is isostructural with diamond. Another less stable, sp^3 hybridized polymorph is wurtzite boron nitride (wBN) whose structure corresponds to the one of technologically important aluminum nitride (AlN) and gallium nitride (GaN). Conversely, sp^2 hybridized polymorphs consist of a graphite-like lamellar structure where atomic planes of tightly bound boron and nitrogen atoms sitting in a honeycomb lattice, namely hBN monolayers, are weakly stacked through van der Waals interactions. The most stable and commonly observed of the sp^2 polymorph is hexagonal boron nitride (hBN), whose atomic structure is shown in Fig.1.1 [9].

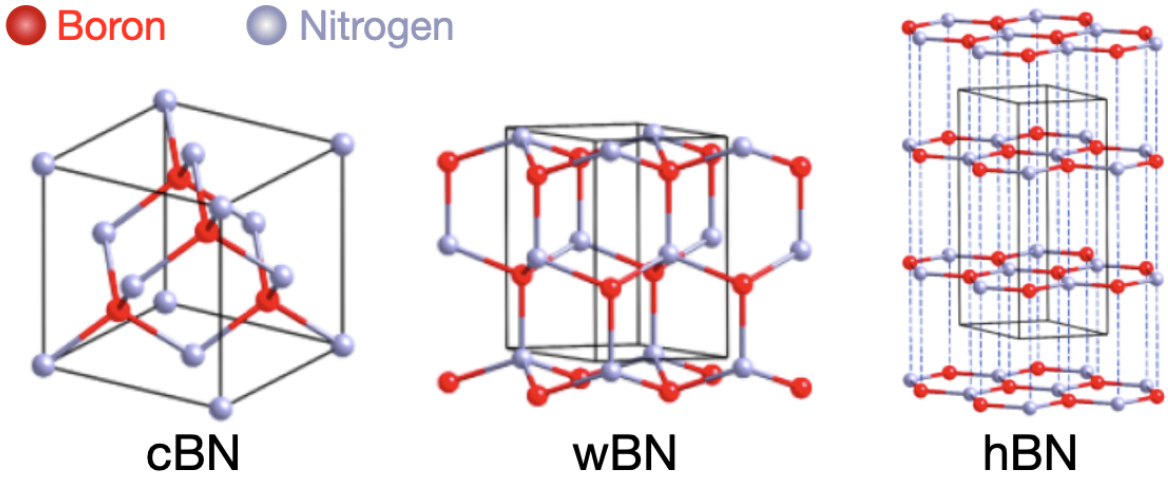

Figure 1.1: Schematic representation of the main BN polymorphs [35].

The weak interlayer interaction in the lamellar structure of hBN allows the formation of various hBN polytypes, which differ by the stacking order, potentially offering a great wealth of properties. Although the physical properties of hBN polytypes mainly derive from the ones of hBN monolayers, the stacking order directly influences both the interlayer interaction and symmetry, thus leading to variations of the physical properties of hBN polytypes. Polytypism has been extensively studied, both theoretically and experimentally, in many materials like SiC, II-VI compounds, hydroxides, and transition-metal triborides. In contrast, despite several theo-

retical investigations, there have been very few experimental studies about polytypism in hBN, largely due to the prevalence of AA' stacking in hBN crystals. However, theoretical studies have shown that other hBN polytypes can also exist under similar conditions, such as rhombohedral boron nitride (ABC-hBN) or bernal boron nitride (AB-hBN) [30, 31, 36–41].

This chapter aims to provide an overview of the microscopic properties of monolayer hBN (Part 1.1) and hBN polytypes (Part 1.2) which will be required to understand the results presented in Chapter 3 and Chapter 4, respectively. The properties of hBN polytypes stemming from the ones of the monolayer hBN building block, I first introduce monolayer hBN in Part 1.1 and then hBN polytypes in Part 1.2 where I mainly focus on AA-hBN, AA'-hBN, AB-hBN and ABC-hBN.

1.1 Monolayer hBN

In this part, I present the main microscopic properties of monolayer hBN that will be used in Chapter 3 which is dedicated to the investigation of the optical properties of monolayer hBN.

1.1.1 Microscopic structure and symmetries

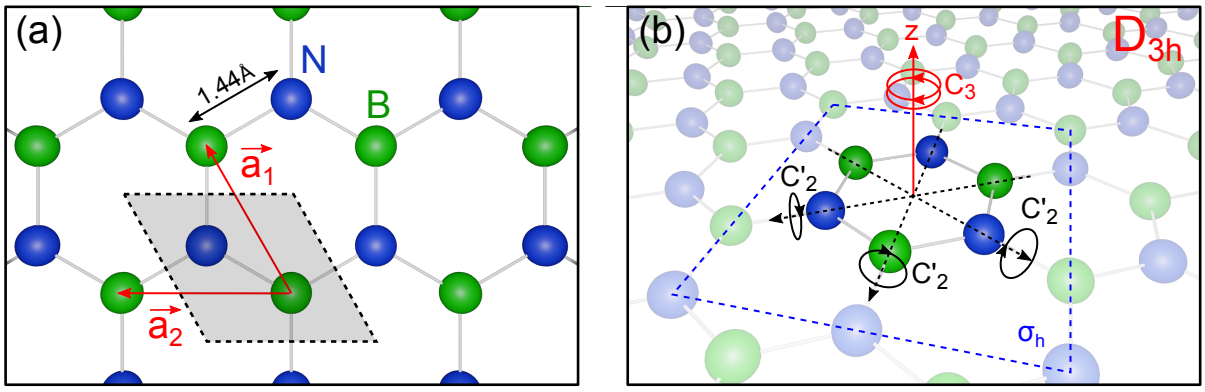

Figure 1.2: (a) Top view representation of monolayer hBN with the B and N atoms in green and blue, respectively, where the black shaded diamond represents the unit cell and the two red arrows represent the two in-plane primitive vectors of the 2D hexagonal lattice. (b) Main symmetries of the D_{3h} point group of monolayer hBN represented for a given hBN hexagon.

A single atomic layer of hBN, so-called monolayer hBN, consists of sp^2 bound B and N atoms in a honeycomb lattice, as represented in Fig.1.2(a). The honeycomb lattice is made through the combination of two 2D hexagonal sublattices connecting all sites of B and N atoms, respectively, described in the language of solid-state physics as a 2D hexagonal Bravais lattice with a unit cell of one B and one N atom, represented by the dashed grey diamond in Fig.1.2(a). The hexagonal Bravais lattice is defined by the two primitive vectors $\vec{a_1} = a.(\frac{1}{2}, \frac{\sqrt{3}}{2})$ and $\vec{a_2} = a.(-\frac{1}{2}, \frac{\sqrt{3}}{2})$ differing by an angle of 60° with the same length ($a = 2.45$Å) corresponding to the in-plane lattice parameter. The interatomic distance between B and N atoms in a unit cell is then

$a_0 = \frac{a}{\sqrt{3}} \sim 1.44$Å. Remarkably, monolayer hBN is isostructural to graphene with an in-plane lattice parameter mismatch of only 1.7%.

The main symmetries of monolayer hBN are illustrated in Fig.1.2(b). The honeycomb lattice of monolayer hBN possesses a 3-fold symmetry (i.e. 120° rotational symmetry) [C_3 in Fig.1.2(b)] due to the distinct boron and nitrogen sublattices. Alternatively, the two equivalent carbon sublattices of graphene lead to a 6-fold symmetry (i.e. 60° rotational symmetry). Additionally, the free-standing monolayer hBN possesses in-plane mirror symmetry along its basal plane [σ_h in Fig.1.2(b)]. Finally, the honeycomb lattice also possesses three equivalent two-fold symmetries [C_2' in Fig.1.2(b)] along the three diagonals of the hexagon. Consequently, the point group symmetry of free-standing monolayer hBN is D_{3h}. Nonetheless, in the general case of non-free-standing monolayer hBN, both C_2' and σ_h are broken by the underlying substrate so that the point group symmetry becomes C_3. The space group of monolayer hBN, obtained from the combination of the point group symmetry D_{3h} (C_3 for non-free-standing monolayer hBN) and the symmetry of the 2D hexagonal lattice, is then $P\bar{6}2m$ ($P3$).

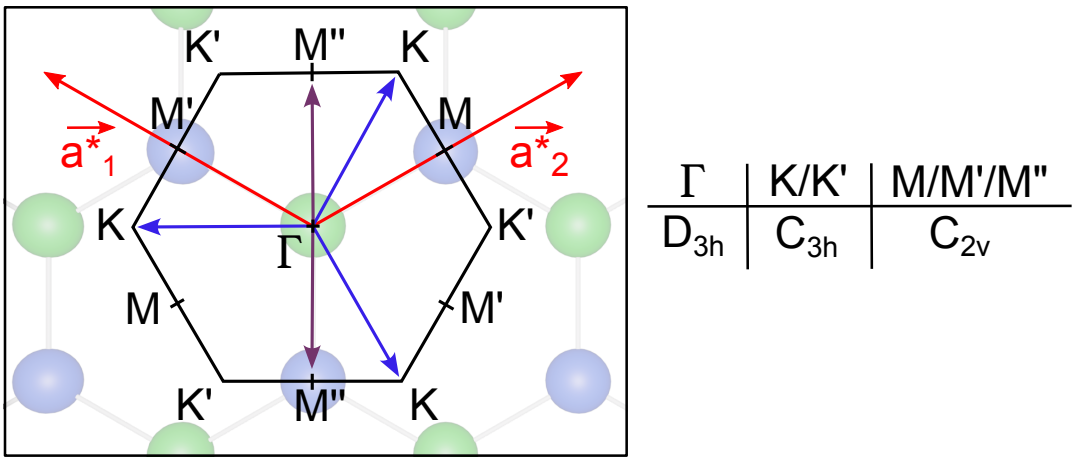

Figure 1.3: First Brillouin zone of monolayer hBN superimposed on the monolayer hBN top view with the high symmetry points and the reciprocal primary vectors in red. On the right side: the table of the small point group symmetry at the different high symmetry points.

The reciprocal lattice of monolayer hBN is also hexagonal and is defined by the two primitive vectors $\vec{a_1}^* = \frac{2\pi}{a}.(-1, \frac{1}{\sqrt{3}})$ and $\vec{a_2}^* = \frac{2\pi}{a}.(1, \frac{1}{\sqrt{3}})$ differing by an angle of 120°, and having the same length. The first Brillouin zone (BZ) and its high symmetry points are represented in Fig.1.3. The high symmetry point Γ corresponds to the center of the BZ ($\vec{k} = \vec{0}$). At this point, the plane wave component of the Bloch states is constant and the small point group corresponds to the crystal point group (D_{3h}). The corners of the BZ ($|\vec{k}| = \frac{4\pi}{3a}$) are divided into two non-equivalent sets of high symmetry points, labeled K and K', induced by the two sublattices. As a consequence, the plane wave components at these points lose the C_2' symmetry, and the small point group becomes C_{3h}. Finally, the middle of the BZ edges ($|\vec{k}| = \frac{2\pi}{\sqrt{3}a}$) are divided into three non-equivalent sets of high symmetry points, labeled M, M' and M''. Consequently, the plane

wave components at these points lose the C_3 symmetry, and their symmetry is given by the small point group C_{2v} [42].

1.1.2 Vibrational properties

With one boron and one nitrogen atom, the unit cell of monolayer hBN has six normal modes which decompose into three acoustic modes (LA/TA/ZA) and three optical modes (LO/TO/ZO), represented in Fig.1.4(a), corresponding to the in-phase and anti-phase vibrations of the atoms of the unit cell along the three directions of space, respectively. Because of the planar symmetry of monolayer hBN, the acoustic (optical) modes split into the two-degenerate in-plane modes LA/TA (LO/TO) and the out-of-plane mode ZA (ZO). Moreover, the symmetry of the in-plane and out-of-plane modes correspond to the ones of the irreducible representations E' and $A"_2$ of D_{3h}, respectively.

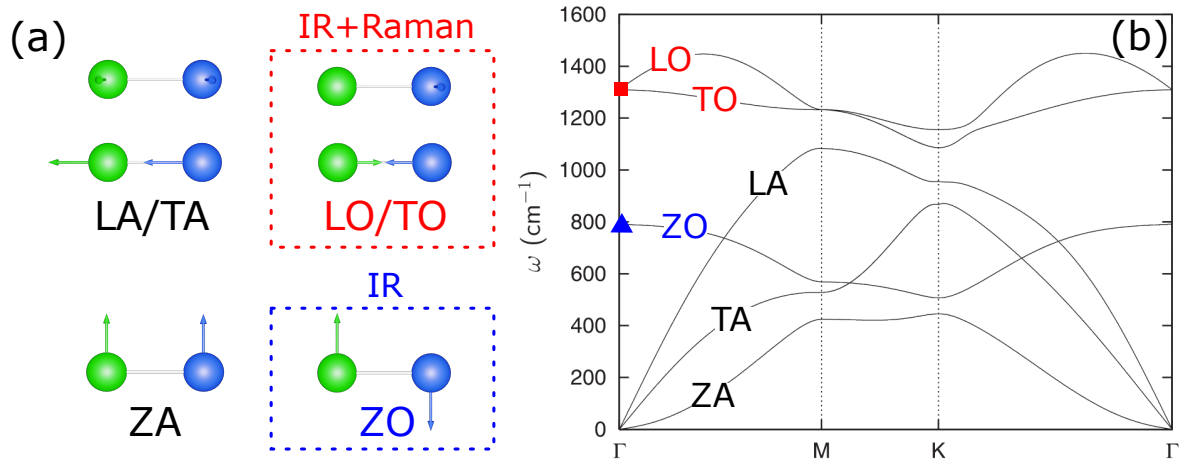

Figure 1.4: (a) Schematic representation of the normal modes of the monolayer hBN unit cell with the optical activity of their corresponding phonons. (b) Phonon dispersion of monolayer hBN calculated by *Michel et al.* [43].

Due to the in-plane periodicity, the normal modes of monolayer hBN are Bloch waves of wavevector $\vec{k}$ in which the periodic component is built from the unit cell normal modes. The phonon dispersion of monolayer hBN, shown in Fig.1.4(b), features six phonon branches splitting into three acoustic branches, arising from LA, TA and ZA, and three optical branches, arising from LO, TO and ZO [43]. Acoustic phonons (LA/TA/ZA) are characterized by a linear dispersion at small $|\vec{k}|$ and a zero energy at Γ while optical phonons (LO/TO/ZO) are characterized by a finite energy at Γ and a globally larger energy than their acoustic counterpart. Furthermore, because of the planar geometry of monolayer hBN, the out-of-plane phonons (ZA and ZO) are softer than the in-plane ones (LA/TA and LO/TO). At Γ, the plane wave component vanishes and the phonons have the symmetry of the normal modes which determine their periodic components. Therefore, the two-degenerate in-plane phonons correspond to the E' symmetry while the out-of-plane phonons correspond to the $A"_2$ symmetry. At finite $|\vec{k}|$ (i.e. outside Γ), the

doubly-degenerate in-plane phonons split between longitudinal phonons (LA and LO), in which the atomic vibrations are parallel to $\vec{k}$, and transverse phonons (TA and TO), in which the atomic vibrations are orthogonal to $\vec{k}$.

The anti-phase vibrations of optical phonons give rise to an electrical polarization that allows them to interact with light, hence the name. Optical phonons are able to interact with light in two distinct ways: through the dipolar interaction by absorbing or emitting a photon, rendering them infrared (IR) active, or through inelastic light scattering known as Raman scattering, making them Raman active. Accordingly, IR active phonons can be measured using linear optical spectroscopy in the IR, such as absorption, reflection or transmission measurements, while Raman active phonons can be measured via Raman spectroscopy. In the first order approximation, only optical phonons at Γ are allowed to interact with light due to momentum conservation. IR and Raman active phonons at Γ are characterized by a dipolar and quadrupolar symmetry along the polarization axis of the incident light. Therefore, for an in-plane light polarization, LO and TO are both IR and Raman active while, for an out-plane light polarization, only ZO is IR active. The IR and Raman signatures of LO/TO have been measured at $\sim$170 meV by several groups [44, 45]. In contrast, the IR signature of ZO, predicted at $\sim$100 meV($\sim$12 µm) in the far-IR (FIR), has not been reported yet requiring an out-of-plane light polarization.

1.1.3 Electronic properties

The electronic configurations of B($1s^2 2s^2 2p^1$) and N($1s^2 2s^2 2p^3$) share the same valence states $2s$, $2p_x$, $2p_y$ and $2p_z$ occupied by 3 and 5 valence electrons, respectively. The honeycomb lattice of monolayer hBN arises from the sp^2 hybridization of $2s$, $2p_x$ and $2p_y$ states in any B and N atom, resulting in sp^2 hybridized atomic orbitals with a trigonal geometry. The hybridized states then overlap with the ones of the nearest atoms forming strong σ-like sp^2 hybridized bounds. Additionally, the unhybridized p_z states in B and N atoms interact laterally with the ones of the nearest atoms forming weaker π-like bounds.

The electronic states of the crystal are Bloch states in which the periodic component can be described through the linear combination of atomic orbitals (LCAO) approximation for each atom of the unit cell. The electronic band structure of hBN has been investigated since 1952 and has been the subject of many studies until today using either ab initio or semi-empirical methods [34, 46–49]. The electronic band structure of free-standing monolayer hBN calculated using density functional theory (DFT) is represented in Fig.1.5(a) [34]. The electronic bands with energies below and above the Fermi level correspond to the valence and conduction bands, respectively. The separation between the conduction bands minimum (CBM) and the valence bands maximum (VBM) corresponds to the so-called electronic (or free-carriers) bandgap. Because of the strong polarity of its atomic bounds, monolayer hBN is a wide bandgap semiconductor with $E_g \sim$7-8 eV [32,34,50–53]. The exact nature of the electronic bandgap of monolayer hBN has long been debated because of the proximity in energy of the direct and indirect bandgaps.

The bandgap is generally found to be direct in K [blue solid arrow in Fig.1.5(a)] under the independent particle approximation, while the indirect bandgap between K and Γ lies slightly above [red dashed arrow in Fig.1.5(a)]. However, by including many-particle interactions via the GW formalism, the direct bandgap energy increases above the indirect one, making the fundamental bandgap indirect [34]. Interestingly, the dispersion of the highest valence band and the lowest conduction band is almost flat along K-M because of the enhanced electronic localization on B and N atoms, respectively, due to their large ionicity difference [54]. Furthermore, the electronic properties of 2D materials are strongly influenced by their environment. In non-free-standing monolayer hBN, the electronic bandgap is significantly reduced due to the dielectric screening of the Coulomb interaction induced by the substrate. The reduction of the electronic bandgap has been estimated around ∼1 eV for monolayer hBN on graphite [55].

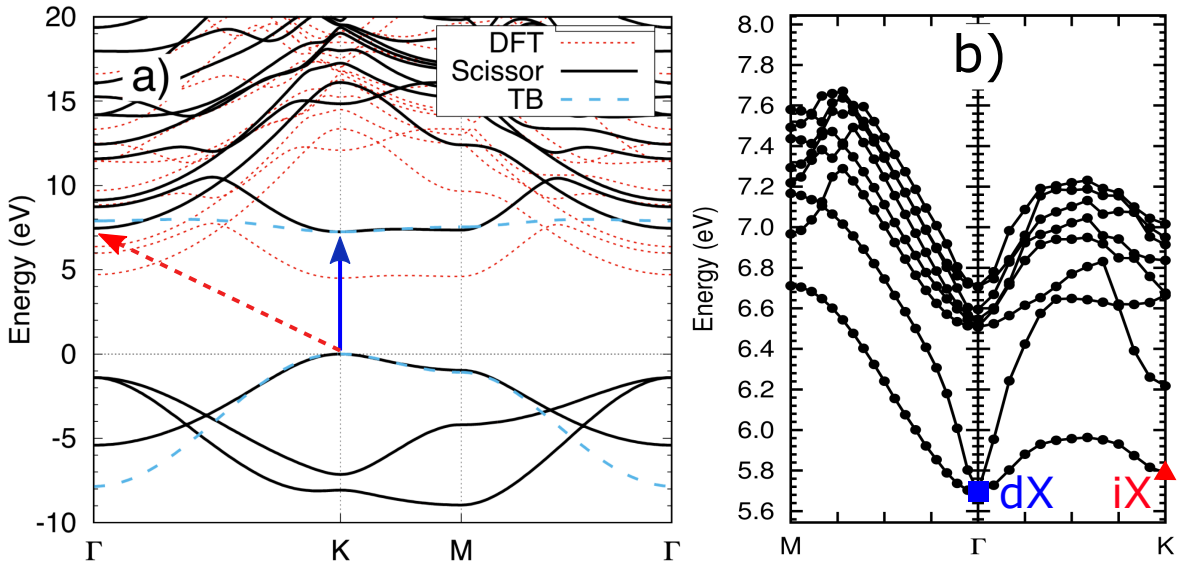

Figure 1.5: (a) Electronic band structure of monolayer hBN calculated by *Sponza et al.* where the direct and indirect electronic bandgaps are represented by the blue solid and red dashed arrows, respectively [32]. (b) Excitonic dispersion of monolayer hBN calculated by *Lechifflart et al.* with the fundamental direct (dX) and indirect (iX) excitons represented by the blue circle and red triangle, respectively [34].

1.1.4 Optical properties

For an intrinsic semiconductor in its ground state, i.e. under thermodynamic equilibrium at T∼0 K, the valence bands are fully occupied by electrons whereas the conduction bands are completely empty. Subsequently, the absorption of a photon by the material simultaneously creates an electron and a hole in the conduction and valence bands, respectively. The oppositely charged particles can then bind to each other through their mutual Coulomb interaction in order to form a new quasiparticle called exciton with an energy lower than the one of the unbound electron-hole pair. Similar to a hydrogen atom, the exciton is a two-body system in which the motion can be separated into the center of mass motion and the relative motion associated with

the total mass $M_X = m_e + m_h$ and reduced mass $1/\mu_X = 1/m_e + 1/m_h$, respectively, with m_e and m_h the electron and hole effective masses. The center of mass motion is characterized by the excitonic wavevector $\vec{K}_X = \vec{k}_e + \vec{k}_h$, with $\vec{k}_e$ and $\vec{k}_h$ the electron and hole wavevectors, respectively. Besides, the relative motion gives rise to bound states of energy E_X^n defined by their binding energy $E_b^n = E_X^n - E_X^\infty$, where E_X^∞ is the ionized state energy. Notably, the bound states are defined by a Bohr radius a_X^n which is inversely proportional to E_b^n. In many inorganic semiconductors, a_X is larger than the lattice parameter, corresponding to E_b generally below $\sim$100 meV, and the exciton wavefunction is delocalized over many unit cells, these are the so-called Wannier excitons. On the contrary, in wide bandgap and organic semiconductors, a_X is on the order or smaller than the lattice parameter, corresponding to E_b generally larger than $\sim$100 meV, and the exciton wavefunction is localized on few atoms only, these are the so-called Frenkel excitons. Finally, excitons can recombine to the vacuum state via radiative or non-radiative recombination processes, leading to the annihilation of the electron-hole pair. Notably, excitons lying inside the light cone, that is the direct excitons, can radiatively recombine via efficient direct recombination processes involving the emission of a photon. On the contrary, excitons lying outside the light cone, that is the indirect excitons, can only recombine via indirect recombination processes requiring the emission of one or several phonons to fulfill the momentum conservation, resulting in less efficient radiative processes.

Fig.1.5(b) represents the calculated excitonic dispersion of free-standing monolayer hBN obtained from *ab-initio* calculations using the Bethe-Salpeter equation (BSE) [32]. The lowest lying exciton at Γ corresponds to the fundamental direct exciton (dX) [blue circle in Fig.1.5(b)] arising from the direct bandgaps at K and K' [blue solid arrow in Fig.1.5(a)]. Additionally, the lowest lying exciton at K corresponds to the fundamental indirect exciton (iX) [red triangle in Fig.1.5(b)] arising from the indirect bandgap between K and Γ [red dashed arrow in Fig.1.5(a)]. Remarkably, dX and iX are predicted at almost the same energy ($E_{dX} \sim$5.7 eV, $E_{iX} \sim$5.8 eV) then raising the question on the exact nature of the excitonic (or optical) bandgap [15, 52]. Recent results obtained by *Elias et al.* on epitaxial hBN monolayers suggest the direct nature of the bandgap of monolayer hBN, where they observed no stokes shift between the PL signal at $\sim$6.08 eV and the dip in reflectivity associated to the direct bandgap resonance [13]. Therefore, the energy of dX is estimated experimentally at $\sim$6.08 eV. However, the physical origin of the PL doublet is still debated and has been tentatively attributed either to the emission of the two inequivalent direct excitons built from carriers in K and K' valleys or to the phonon replicas from the phonon-assisted indirect emission of iX in monolayer hBN [14, 56, 57].

Both iX and dX are found to have binding energy E_b of about $\sim$2 eV, much larger than for most of the excitons in other inorganic semiconductors such as in silicon ($\sim$10 meV), carbon nanotubes (0.2-0.5 eV) or transition metal dichalcogenides (0.2-0.9 eV) [45]. The reason for this ultra-large binding energy in monolayer hBN is two-fold : (1) the reduced screening of the Coulomb interaction due to the lower dimensionality in 2D materials ; (2) the tight localization

of the exciton wavefunction on a few atoms due to the strong ionicity of the atomic bounds, thus resulting in Frenkel-type excitons. Furthermore, as for E_g (Section 1.1.3), the dielectric screening of the electron-hole pair Coulomb interaction induced by the substrate in non-free-standing monolayer hBN leads to lower binding energy E_b that varies between 1-2 eV with the substrate relative permittivity [55]. Notably, the dielectric screening introduces compensatory effects on both the repulsive electron-electron renormalization affecting E_g and the attractive electron-hole binding of excitons affecting E_b. As a result, the energy of dX ($E_{dX} = E_g - E_b$) remains largely unaffected by the dielectric screening as depicted in Fig.1.6. Fig.1.6 shows the variations of E_g [blue squares], E_b [red circles] and E_{dX} [green triangles] as a function of the interlayer distance between hBN monolayers, resulting in a virtual modification of the monolayers dielectric environment, calculated from *ab initio* calculations in the GW formalism [58]. Accordingly, the compensatory effects of the dielectric screening lead to similar dX energy in monolayer and bulk hBN [13], as it will be shown in Section 1.2.4.

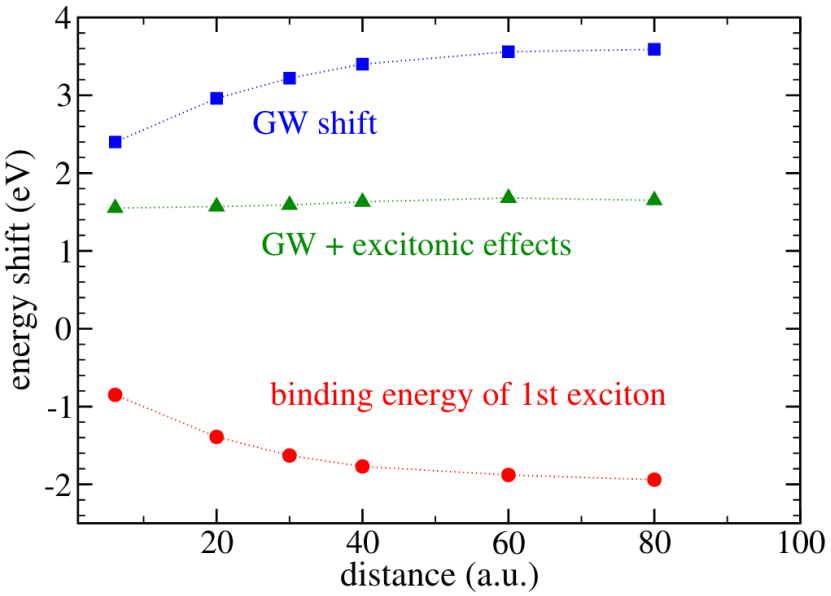

Figure 1.6: Dependence of the bandgap energy (E_g - blue squares), the exciton binding energy of dX (E_b - red circles) and the dX energy (E_{dX} - green triangles) of monolayer hBN as a function of the interlayer distance between hBN monolayers calculated in the GW formalism [58].

Finally, the radiative linewidth of dX has been estimated at ~20 meV by *Cassabois et al.* from deep-UV reflectivity measurements [45]. This value is at least 4 times larger than in other 2D materials and suggests a large oscillator strength for dX. Interestingly, the flat dispersion along K-M in the electronic band structure around both the VBM and the CBM leads to many almost degenerate direct electronic transitions contributing to the large oscillator strength of dX [45].

Up to now, the optical properties of monolayer hBN are still very partially understood, notably regarding the origin of the PL doublet around 6.1 eV measured by *Elias et al.* [13], as well as the structured emission profile around this doublet. In Chapter 3, I will introduce the main experimental challenge that represents the study of the optical properties of monolayer hBN and I will present the results obtained on different hBN monolayers using our home-built deep-UV microscope. My results will provide a better understanding of the optical properties of monolayer hBN in the deep-UV.

1.2 hBN polytypes

In this part, I present the main microscopic properties of hBN polytypes that derive from the ones of monolayer hBN presented in Part 1.1. This part will be required to understand our results of Chapter 4 where we realize an in-depth study of the optical properties of the bernal boron nitride (AB-hBN) polytype.

1.2.1 Microscopic structures and symmetries

As seen at the beginning of this chapter, hBN is a lamellar material where hBN monolayers are weakly stacked through van der Waals interactions. The weak interlayer interaction in hBN allows various stackings of hBN monolayers leading to the formation of the so-called hBN polytypes, which only differ by their periodic stacking sequence. Therefore, in addition to the in-plane periodicity of monolayer hBN, hBN polytypes present an out-of-plane periodicity given by the primitive vector $\vec{c} = (0, 0, nc_0)$, where c_0 is the interlayer distance and n is the number of monolayers in the stacking sequence. hBN polytypes are 3D crystals with a unit cell that builds from the unit cell of each layer of the stacking sequence, thus containing $2n$ atoms per unit cell.

θ \ δ	$-\frac{a}{\sqrt{3}}$	0	$\frac{a}{\sqrt{3}}$
0°	AB n=2 / ABC n=3	AA n=1	AB n=2 / ABC n=3
60°	A'B n=2	AA' n=2	AB' n=2

Table 1.1: Nomenclature of the hBN polytypes represented in Fig.1.8 based on the discrete values of n(1,2,3), θ(0°,60°) and $\delta(0, \pm\frac{a}{\sqrt{3}})$

The stacking between two consecutive layers is characterized by two parameters: the twist angle (θ) and the in-plane shift (δ) along one of the honeycomb diagonals [see Fig.1.8]. The stacking sequence of hBN polytypes can then be defined by n, θ and δ. Moreover, the stability of hBN polytypes depends on the interlayer interaction which varies with the stacking sequence. Therefore, stable hBN polytypes correspond to discrete values of n, θ and δ for which the stack-

ing energy due to the interlayer interaction is a minimum. It turns out that the most stables polytypes are only obtained for $n = 1, 2, 3$ and for parallel (θ =0°) and anti-parallel (θ =60°) stackings, other values of n and θ leading to instabilities of the stacking because of the interlayer repulsion [30, 31, 41]. Fig.1.7 displays the variations of the stacking energy (ΔE) as a function of δ calculated for different values of c_0 by *Constantinescu et al.* for parallel [panel (b)] and anti-parallel [panel (a)] periodic stackings of n=2 layers [30]. The hBN polytypes corresponding to the extrema of Fig.1.7 are represented in Fig.1.8. Remarkably, for each family of stackings (parallel/anti-parallel), the layers in the stacking sequence of these specific polytypes are either well aligned ($\delta = 0$), or staggered by one-half of the hexagon diagonal ($\delta = \pm\frac{a}{\sqrt{3}}$). These polytypes are then defined using the nomenclature of Tab.1.1 based on the discrete values of n(1,2,3), θ(0°,60°) and $\delta(0, \pm\frac{a}{\sqrt{3}})$ of their stacking sequence.

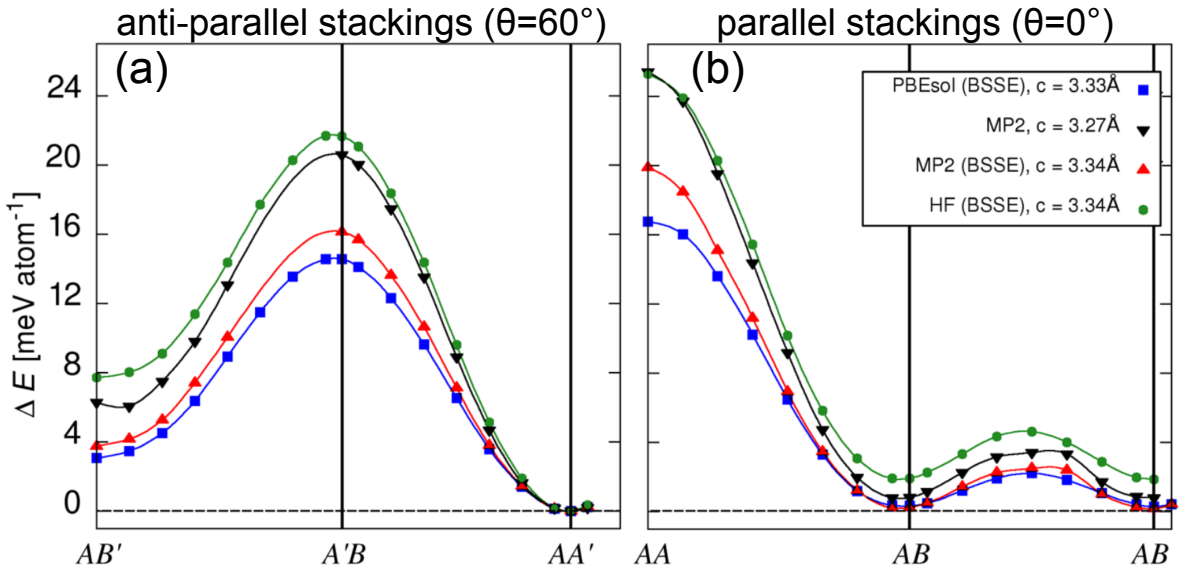

Figure 1.7: Plot of the variations of the polytypes energy as a function of δ calculated for different value of c_0 by *Constantinescu et al.* for parallel (θ =0°) [panel (a)] and anti-parallel (θ =60°) [panel (a)] periodic stackings of 2 layers [30].

The most stable of the anti-parallel polytypes is AA'-hBN ($\delta = 0$) [AA' in Fig.1.7(a)] which consists of well-aligned 60° rotated hBN monolayers where B and N atoms alternate along the c-axis [AA'-hBN in Fig.1.8]. The high stability of the AA' stacking is explained by the alternation of oppositely charged B and N atoms along the c-axis resulting in an interlayer attraction. Accordingly, AA'-hBN is the most commonly observed and studied of the hBN polytypes and its physical properties are globally well understood. A less stable anti-parallel polytype is AB'-hBN ($\delta = \frac{a}{\sqrt{3}}$) [AB' in Fig.1.7(a)], with ΔE ~3-8 meV, which consists of staggered 60° rotated hBN monolayers where B atoms sit on top of each other along the c-axis while N atoms sit in the middle of the hexagons of the surrounding layers [AB'-hBN in Fig.1.8]. The stability of AB' could be explained by the relatively small atomic repulsion between B atoms compensated by the attraction of the neighboring N atoms. On the contrary, in A'B-hBN, where N atoms sit on

top of each other along the c-axis, the atomic repulsion between N atoms dominates resulting in a large instability [A'B in Fig.1.7(a)], with ΔE ~12-21 meV. In contrast to its anti-parallel counterpart AA'-hBN, AA-hBN ($\delta = 0$) is the most unstable of the hBN polytypes [AA in Fig.1.7(b)], with ΔE ~16-~24 meV, because of the perfect alignment of B and N atoms along the c-axis [AA-hBN in Fig.1.8] resulting in a strong interlayer repulsion. Calculations predict similar stability for AA'-hBN and AB-hBN [AB in Fig.1.7], ΔE ~0-4 meV, which consists of hBN monolayers staggered every two layers by one-half of the hexagon diagonal ($\delta = \pm\frac{a}{\sqrt{3}}$) [AB-hBN in Fig.1.7]. Therefore, half of the B and N atoms of each layer alternate along the c-axis as in AA'-hBN thus explaining the high stability predicted for AB-hBN. With similar stability as AB-hBN, another stable parallel polytype is ABC-hBN [not calculated in Fig.1.8] which consists of hBN monolayers consecutively staggered by one-half of the hexagon diagonal [ABC-hBN in Fig.1.7], leading to a unit cell of 3 layers in contrast to AB-hBN. Therefore, ABC-hBN and AB-hBN are predicted as two stable alternatives of AA'-hBN and are prone to coexist in hBN crystals under usual conditions. However, there have been very few reports on the observation of these polytypes. A state-of-the-art review of the few observations of AB-hBN and ABC-hBN in hBN crystals will be presented in Chapter 4.

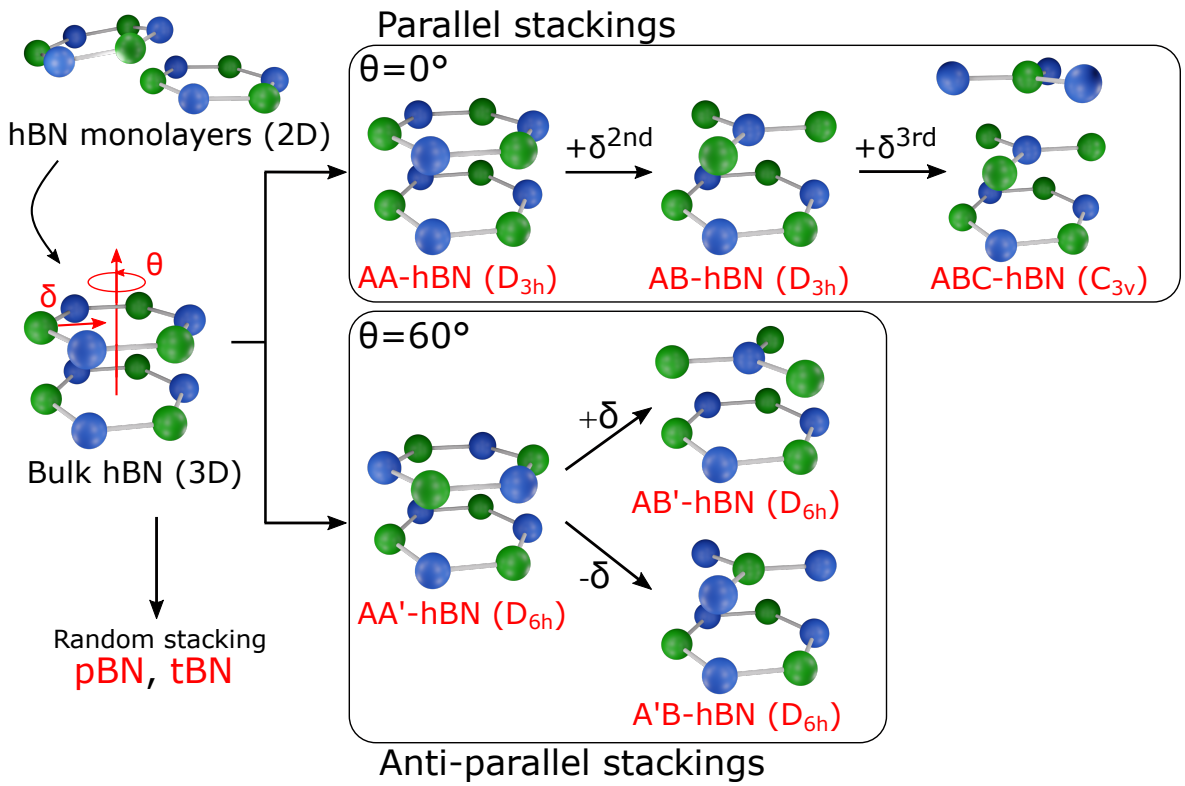

Figure 1.8: hBN polytypes arranged with respect to n, θ and δ, with $\delta = \frac{a}{\sqrt{3}}$, with their corresponding point group symmetry.

Tab.1.2 summarizes the values of ΔE, a_0 and c_0 estimated, from calculations or experimentally, for each polytype by different groups. Interestingly, since ΔE increases with the interlayer repulsion, the interlayer distance c_0 seems to vary with ΔE and thus, depends on hBN polytypes. In contrast, the interatomic distance a_0 is unaffected by the interlayer interaction because of the stronger in-plane bounds. Therefore, the in-plane primitive vectors of hBN polytypes $\vec{a_1}$ and $\vec{a_2}$ are found to be the same as in monolayer hBN while $\vec{c}$ depend on both n and c_0 with the stacking.

The point group symmetry of each hBN polytype is given in Fig.1.8. Remarkably, the anti-parallel polytypes acquire the six-fold symmetry (C_6) whereas parallel polytypes preserve the C_3 symmetry of monolayer hBN. Moreover, all periodic stackings of one and two layers systematically also keep the in-plane mirror symmetry σ_h. Therefore, every anti-parallel polytype (AA'-hBN, AB'-hBN and A'B-hBN) has the point group symmetry D_{6h} which includes the inversion symmetry (i) characteristic of centrosymmetric crystals. Switching to parallel polytypes, AA-hBN and AB-hBN, with 1 and 2 layers per unit cell, respectively, have the point group symmetry D_{3h}. In contrast, with 3 layers per unit cell, ABC-hBN loses the symmetry σ_h and is reduced to the point group symmetry C_{3v}. Since D_{3h} and C_{3v} do not include the inversion symmetry, parallel polytypes are non-centrosymmetric crystals. From our analysis, we remark that the symmetry of polytypes only depends on θ (parallel or anti-parallel) and n while it does not depend on δ.

Importantly, second-order processes, and more generally even-order processes, are symmetry-forbidden in centrosymmetric crystals like for anti-parallel stackings of hBN. Reciprocally, they are allowed in non-centrosymmetric crystals such as hBN with parallel stacking. Therefore, this effect can be used to probe the type of stackings, parallel or anti-parallel, of a given polytype by using second-harmonic generation (SHG) microscopy as it will be demonstrated in Chapter 4. Moreover, the lack of the in-plane mirror symmetry allows the emergence of ferroelectricity in ABC-hBN. Accordingly, the different symmetries induced by the stacking have an important impact on the properties of hBN polytypes, regardless of their chemical similarity.

The space groups of hBN polytypes, derived from the combination of the Bravais lattice and the point group symmetry, are $P6_3/mmc$, $P\bar{6}2m$, and $R3m$ for point groups D_{6h}, D_{3h}, and C_{3v}, respectively. The out-of-plane reciprocal lattice vector writes $\vec{c}^* = (0, 0, \frac{2\pi}{nc_0})$ which is inversely proportional to the number of layers (n) in the stacking sequence of hBN polytypes. On the contrary, the in-plane reciprocal lattice vectors $\vec{a_1}^*$ and $\vec{a_2}^*$ are similar to the one of monolayer hBN and they do not depend on n. Fig.1.9 represents the BZ of hBN polytypes with its high symmetry points, where only the height varies oppositely with the number of monolayers n in the stacking period of hBN polytypes. The middle plane of the BZ corresponds to the 2D BZ of monolayer hBN with the corresponding high symmetry points Γ, K/K' and M/M'/M". The projection of these points on the top and bottom faces of the BZ correspond to A, H/H' and L/L'/L", respectively.

Polytypes	Groups	ΔE (meV/atom)	a_0 (Å)	c_0 (Å)
AA-hBN	Gil et al. [59]	∼15	1.430	3.468
	Constantinescu et al. [30]	17	1.430	3.33
	Mosuang et al. [60]	13	1.443	3.791
	Liu et al. [61]	14	1.435	3.456
	Hu et al. [62]	13.5	1.440	3.535
	Haga et al. [63]	13	-	3.585
AB-hBN	Gil et al. [59]	∼0	1.430	3.160
	Constantinescu et al. [30]	0	1.430	3.34
	Liu et al. [61]	0	1.435	3.212
	Hu et al. [62]	0	1.437	3.223
	Haga et al. [63]	0	-	3.227
	Gao et al. [41]	0	1.433	2.990
ABC-hBN	**Experiment** [36]	-	**1.446**	**3.33**
	Gil et al. [59]	∼0	1.430	3.226
	Furthmüller et al. [64]	-8.1	2.495	3.228
	Albe et al. [65]	0	1.439	3.231
	Haga et al. [63]	0.08	-	3.231
AA'-hBN	**Experiment** [36]	-	**1.446**	**3.328**
	Gil et al. [59]	∼0	1.430	3.177
	Constantinescu et al. [30]	0	1.430	3.33
	Mosuang et al. [60]	0	1.445	3.419
	Liu et al. [61]	0	1.435	3.245
	Hu et al. [62]	0.62	1.437	3.241
	Albe et al. [65]	0	1.441	3.245
	Gao et al. [41]	0.75	1.434	3.002
	Haga et al. [63]	0.725	-	3.247
A'B-hBN	Gil et al. [59]	∼0	1.430	3.192
	Constantinescu et al. [30]	3	1.430	3.33
	Liu et al. [61]	2	1.434	3.244
	Hu et al. [62]	1.290	2.489	3.262
	Gao et al. [41]	3.5	1.432	3.028
AB'-hBN	Gil et al. [59]	∼15	1.430	3.192
	Constantinescu et al. [30]	14	1.430	3.33
	Mosuang et al. [60]	3	1.443	3.546
	Liu et al. [61]	12	1.434	3.524
	Hu et al. [62]	13.39	1.440	3.503
	Gao et al. [41]	27	1.432	3.451

Table 1.2: State-of-the-art review of the calculated values of ΔE, a_0 and c_0 obtained by *ab-initio* calculations for each hBN polytypes [30, 41, 59–63, 65]. The experimental values of a_0 and c_0 measured by *Kurdyumov et al.* for AA'-hBN and ABC-hBN are also given [36].

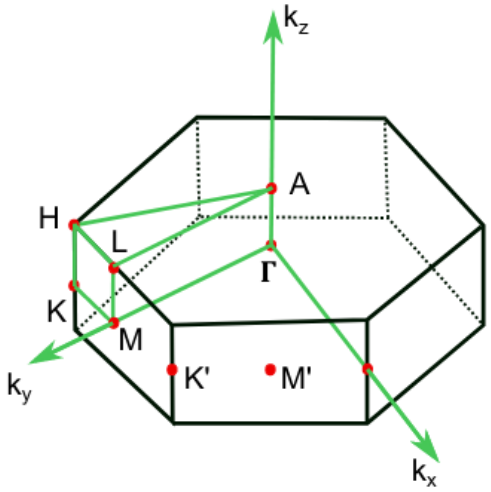

	Γ	K/K'	M/M'/M"
AA	D_{3h}	C_{3h}	C_{2v}
AA'	D_{6h}	D_{3h}	D_{2h}
AB	D_{3h}	C_{3h}	C_{2v}
ABC	C_{3v}	C_3	C_2

Figure 1.9: First Brillouin zone of bulk hBN with the high symmetry points and, on the right, the small point groups at each high symmetry point for the different hBN polytypes.

The small point group symmetry at the different high symmetry points of AA-hBN, AA'-hBN, AB-hBN and ABC-hBN are summarized in Fig.1.9. The symmetry of the plane wave components at the high symmetry points depends on the point group symmetry of hBN polytypes. For AA-hBN and AB-hBN corresponding to D_{3h}, the symmetry of the plane wave components is identical to monolayer hBN which is C_{3h} in K/K' (or H/H') and C_{2v} in M/M'/M" (or L/L'/L"). For ABC-hBN, without σ_h the symmetry becomes C_3 in K/K' (or H/H') and C_2 in M/M'/M" (or L/L'/L"). Because of the higher symmetry of anti-parallel polytypes, the symmetry of the plane wave components in AA'-hBN is increased to D_{3h} in K/K' (or H/H') and D_{2h} in M/M'/M" (or L/L'/L").

1.2.2 Vibrational properties

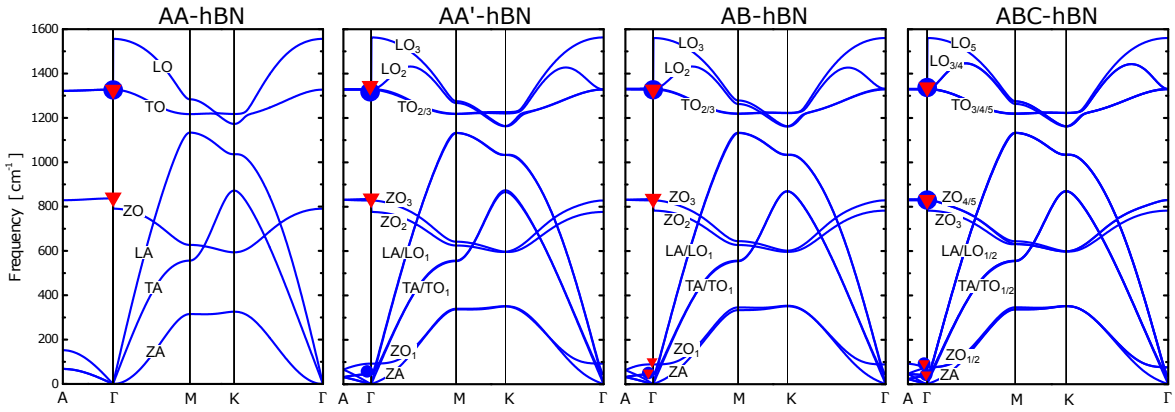

Figure 1.10: Phonon dispersions of AA-hBN, AA'-hBN, AB-hBN and ABC-hBN, respectively, calculated by *W. Desrat* in *Gil et al.* [59].

With $2n$ atoms per unit cell, the unit cell of hBN polytypes has $6n$ normal modes arising from the different in-phase and anti-phase combinations of the monolayer normal modes (LA, TA, ZA, LO, TO and ZO) for each layer in the unit cell. Correspondingly, each branch in the phonon dispersion of monolayer hBN gives rise to n branches in the phonon dispersion of hBN polytypes. Fig.1.10 shows the phonon dispersions of AA-hBN, AA'-hBN, AB-hBN and ABC-hBN [59]. The number of branches is 6 in AA-hBN ($n = 1$), 12 in AA'-hBN and AB-hBN ($n = 2$), and 18 in ABC-hBN ($n = 3$). For any hBN polytype, the in-plane dispersion [Γ-M-K-Γ paths in Fig.1.10] displays the same general structure as in monolayer hBN that is due to the weak interlayer coupling. Importantly, a striking difference with monolayer hBN is the large splitting between transverse and longitudinal optical phonons at 1300 and ∼1550 cm^{-1} near Γ. This transverse-longitudinal splitting arises from the light-matter coupling of IR active phonons in bulk crystals induced by the 3D translational invariance. In contrast, such splitting is not observed for IR active phonons in monolayer hBN due to the weak light-matter coupling due to the lack of translational symmetry along the out-of-plane direction [66]. Finally, the out-of-plane dispersion [Γ-A paths in Fig.1.10] is globally flat along Γ-A because of the weak interlayer interaction.

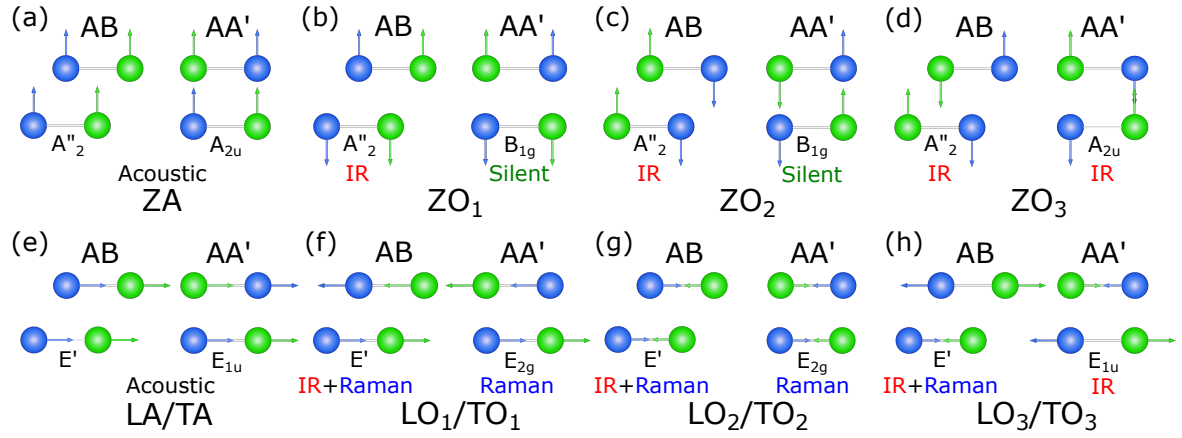

Figure 1.11: Schematic representation of the unit cell normal modes of the AB-hBN (AB) and AA'-hBN (AA') with their symmetry and optical properties (IR, Raman or silent).

As for monolayer hBN, we focus on the first-order optical properties of optical phonons at Γ dictated by the symmetry of the normal modes that compose their periodic components. Importantly, whereas in non-centrosymmetric crystals (parallel polytypes) the optical phonons can be either IR or Raman active or both, in centrosymmetric crystals (anti-parallel polytypes) they must be distinctly either IR or Raman active or optically inactive (silent). With one hBN monolayer in its unit cell, AA-hBN has the same symmetry and presents the same normal modes as in monolayer hBN resulting in similar optical properties for the phonons. Therefore, LO/TO (E') are both IR and Raman active for an in-plane polarized light, while ZO ($A"_2$) is only IR active for an out-of-plane polarized light. With two hBN monolayers per unit cell, AB-hBN and

AA'-hBN have different normal modes from the ones in monolayer hBN. The unit cell normal modes of AB-hBN and AA'-hBN are represented schematically with their symmetry and optical properties in Fig.1.11. Due to its similar symmetry D_{3h} as monolayer hBN, the normal modes of AB-hBN present the same symmetries as the monolayer modes which they arise from. Similarly, LO_1/TO_1, LO_2/TO_2 and LO_3/TO_3, which derive either from LA/TA or LO/TO, have the E' symmetry and are both IR and Raman active for an in-plane polarized light while $ZO_{1/2/3}$ ($A"_2$), which derive either from ZA or ZO, have the $A"_2$ symmetry and are only IR active for an out-of-plane polarized light. Things get more complicated for AA'-hBN where the higher symmetry D_{6h} compared to monolayer hBN leads to different symmetry of normal modes corresponding to distinct optical properties due to the centrosymmetry. LO_1/TO_1 and LO_2/TO_2, which derive from the anti-phase combination of LA/TA and the in-phase combination of LO/TO, respectively, have the E_{2g} symmetry and are Raman active for an in-plane polarized light only. LO_3/TO_3, which derive from the anti-phase combination of LO/TO, have the E_{1u} symmetry and are IR active only for an in-plane polarized light. Then, ZO_1 and ZO_2, which derive from the anti-phase combination of ZA and the in-phase combination of ZO, respectively, have the B_{1g} symmetry and are silent, while ZO_3, which derives from the anti-phase combination of ZO, is IR active for an out-of-plane polarized light. Finally, with three hBN monolayers per unit cell, ABC-hBN presents 12 normal modes that differ from monolayer hBN. However, due to the lower symmetry C_{3v} of ABC-hBN, all in-plane and out-of-plane normal modes of ABC-hBN are both IR and Raman active for an in-plane and out-of-plane polarized light, respectively.

Polytypes	$50-60cm^{-1}$ ($6-8meV$)	$90-110cm^{-1}$ ($10-15meV$)	$750-850cm^{-1}$ ($90-100meV$)	$1360-1370cm^{-1}$ ($168-170meV$)
AA-hBN	None	None	ZO(IR)	LO/TO(IR+R)
AA'-hBN	LO_1/TO_1(R) $\sim 52cm^{-1}$ [67]	ZO_1(S)	ZO_2(S) ZO_3(IR) $\sim 783cm^{-1}$ [68]	LO_2/TO_2(R) LO_3/TO_3(IR) $\sim 1370cm^{-1}$ [68]
AB-hBN	LO_1/TO_1(IR+R)	ZO_1(IR)	$ZO_{2/3}$(IR)	$LO_{2/3}/TO_{2/3}$(IR+R)
ABC-hBN	$LO_{1/2}/TO_{1/2}$(IR+R)	$ZO_{1/2}$(IR+R)	$ZO_{3/4/5}$(IR+R)	$LO_{3/4/5}/TO_{3/4/5}$(IR+R)

Table 1.3: Optical properties of the different normal modes as a function of energy for the four hBN polytypes (AA-hBN, AA'-hBN, AB-hBN and ABC-hBN). [59]

Table 1.3 summarizes the optical properties of phonons at Γ organized with their energy in AA-hBN, AA'-hBN, AB-hBN and ABC-hBN [59]. The most important differences lie in the energy ranges 90-110 cm^{-1}(10-15 meV) and 750-850 cm^{-1}(90-100 meV), corresponding to the

out-of-plane optical phonons whose symmetry is more affected by the stackings. Around 90-110 cm^{-1}, neither IR nor Raman activity can be observed in AA-hBN and AA'-hBN while IR and both IR and Raman signals are observable in AB-hBN and ABC-hBN, respectively. Therefore, the observation of an IR resonance at 90-110 cm^{-1}(10-15 meV) along with the absence of Raman activity at the same spectral range could be an indication for the presence of AB-hBN. Around 750-850 cm^{-1}, while IR signal is observed for any polytype, Raman signal is only observed in ABC-hBN. Therefore, the observation of a Raman peak at $\sim$800 cm^{-1}($\sim$100 meV) gives a direct indication for the presence of ABC-hBN in hBN crystals. Importantly, such identification techniques of hBN polytypes based on the optical response of out-of-plane phonons require an out-of-plane light polarization which can be obtained using finite incident angles [69]. Alternatively, the optical response of in-plane phonons can be studied at $\sim$50 cm^{-1}(6-8 meV) and $\sim$1370 cm^{-1}(168-170 meV). Remarkably, the IR and Raman signals arising from in-plane optical phonons at $\sim$1370 cm^{-1}(168-170 meV) do not change with polytypes. Around $\sim$50 cm^{-1}(6-8 meV), while both IR and Raman signals are observed in AB-hBN and ABC-hBN, only a Raman signal is observed in AA'-hBN. Therefore, the observation of a Raman signal along with the absence of IR signal at $\sim$50 cm^{-1} could indicate the presence of AA'-hBN [59].

1.2.3 Electronic properties

Similar to phonons, the electronic states of hBN polytypes arise from different combinations of the electronic states of each layer in the unit cell [47]. Therefore, each electronic band of monolayer hBN splits into n bands corresponding to different combinations of the monolayer electronic states. The electronic band structures of AA'-hBN, AB-hBN and ABC-hBN calculated using *ab-initio* calculations including the many-body interaction (GW-DFT) are shown in Fig.1.12 [32, 49]. Again, the weak interlayer interaction in hBN polytypes leads to an in-plane electronic dispersion [Γ-K-M-Γ in Fig.1.12] displaying the same general structure as the one of monolayer hBN. This is particularly the case for valence bands which are very similar in polytypes and monolayer hBN both displaying a VBM around K (K') [see Fig.1.12]. In contrast, the interlayer interaction induces a red-shift of the CBM at M in monolayer hBN below the ones at Γ and K (K'), thus transforming the direct bandgap at K (K') of monolayer hBN ($E_g$$\sim$8 eV) to an indirect bandgap between K (K') and M for any hBN polytypes ($E_g$$\sim$6 eV) in the GW formalism, resulting in a bandgap crossover [32, 70]. Moreover, the alteration of the interlayer interaction caused by the stacking arrangement leads to a shift in energy of the CBM at M while keeping the VBM almost unchanged, resulting in a change in the value of E_g depending on the stacking configuration. In contrast, the CBM at K (K') is weakly modified by the stacking and always lies above the CBM at M in AA'-hBN, AB-hBN and ABC-hBN. Accordingly, all the stable hBN polytypes present a fundamental indirect bandgap between K(K') and M where only the value of E_g varies with polytypes.

Fig.1.12(d,e,f) show the band structures along the path $\Gamma - K - M - K' - \Gamma$ in the BZ zoomed in the region of the bandgap in order to better see the electronic dispersion for the

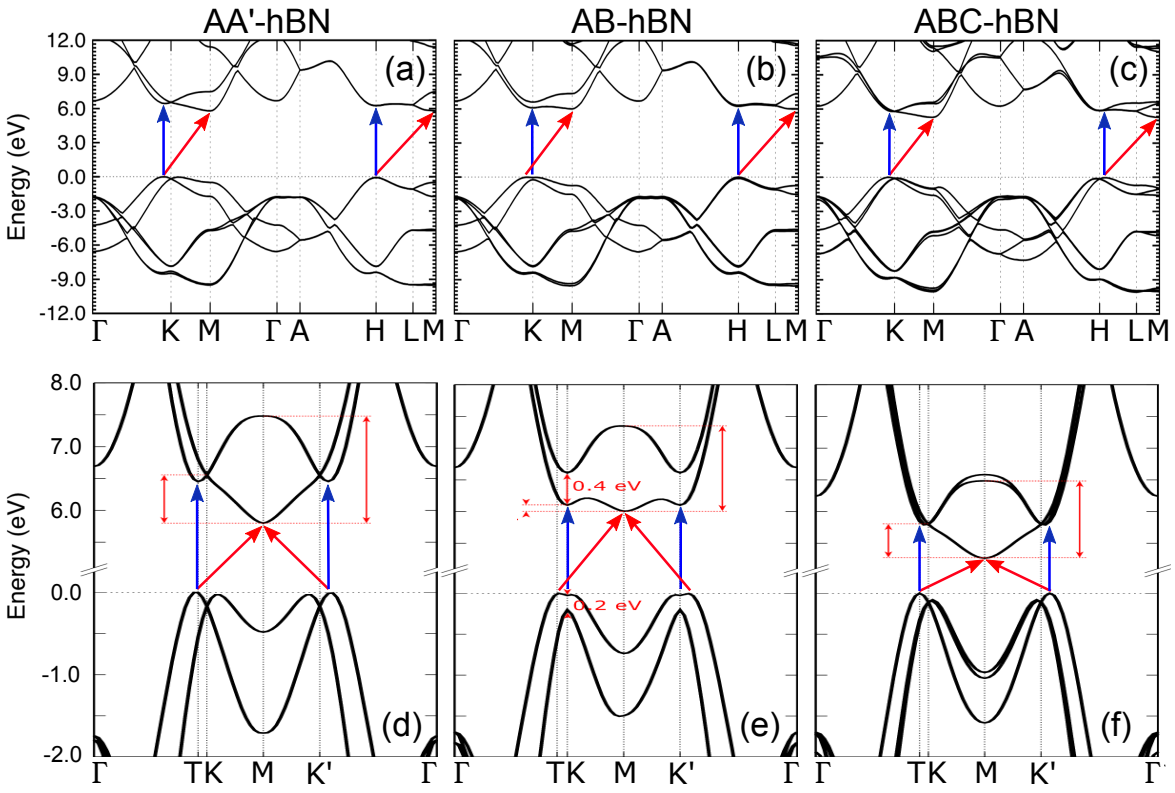

Figure 1.12: (a-c) Electronic band structures of AA'-hBN (a), AB-hBN (b) and ABC-hBN (c) along the path Γ-K-M-Γ in the BZ calculated by *Sponza et al.* via *ab-initio* calculations including the many particles interaction (GW-DFT). (d-e) Zoom of the above electronic band structures along the path $\Gamma - K - M - K' - \Gamma$ in the BZ [32]. The direct and indirect bandgaps are represented by the red and blue arrows, respectively

different polytypes. While the absolute value of E_g is always underestimated by *ab initio* calculations, the analysis of its variations with the stacking should give reliable predictions [32]. From the electronic dispersion of Fig.1.12(d,e,f), we observe variations of about $\sim$10 % of E_g with a $\sim$200 meV blue-shift ($\sim$500 meV red-shift) of E_g in AB-hBN (ABC-hBN) compared to AA'-hBN. Besides, the variations of the direct bandgap at K (K') with the stacking are completely different with a red shift of $\sim$150 meV and $\sim$450 meV in AB-hBN and ABC-hBN compared to AA'-hBN. Therefore, the energy splitting between the direct and indirect bandgap varies with polytypes. Interestingly, this splitting is predicted to be less than 0.1 eV in AB-hBN where the CBM at K (K') and M lie at almost the same energy [32]. This leads to an important effect on the optical properties of AB-hBN as we will see in Section 1.2.4.

As in monolayer hBN, electronic flat bands along K-M are also observed in hBN polytypes and they are due to the localization of electrons on B and N atoms due to their ionicity difference. Additionally, the weak interlayer coupling leads to a weak delocalization of their wavepackets along the c-axis inducing a rather flat electronic dispersion along K-H (K'-H'). Remarkably, this

leads to a degeneracy of the direct and indirect bandgaps along k_z as shown by the pairs of red and blue arrows on the right side of Fig.1.12(a,b,c) [54]. These flat bands are at the origin of the unique optical properties of hBN as we will see in Section 1.2.4.

1.2.4 Optical properties

The excitonic dispersions in AA'-hBN, AB-hBN and ABC-hBN calculated by *Sponza et al.* from *ab-initio* calculations using the Bethe-Salpeter equation (BSE) are shown in Fig.1.13 [32]. The red (empty) circles and dark (filled) circles in Fig.1.13 represent the free electron-hole pair states and the excitonic states along Γ-K, respectively. The fundamental direct (dX) and indirect (iX) excitons are represented by the large blue and red circles for each polytype in Fig.1.13. For any polytype, iX lies at nearly halfway of Γ-K path (k_T ~0.7-0.8 Å^{-1}), the so-called T point, corresponding to the momentum difference between the VBM at K and the CBM at M [see Fig.1.12]. In AA'-hBN and ABC-hBN, dX lies 100-200 meV above iX thus leading to an indirect optical bandgap. The situation is slightly different in AB-hBN where dX lies 20-40 meV below iX resulting in a marginally direct optical bandgap while the electronic bandgap was marginally indirect. This quasi-degeneracy of iX and dX will be of significant importance to understand the optical properties of AB-hBN as it will be shown in detail in Chapter 4.

As for monolayer hBN, excitons are strongly bound in hBN polytypes with a binding energy E_b of dX and iX ranging from 200 to 500 meV [8]. As discussed in Section 1.1.4, the smaller value of E_b compared to monolayer hBN (E_b~2 eV) is due to the dielectric screening of the excitons Coulomb interaction induced by the layers proximity in the lamellar structure of hBN polytypes [see Fig.1.6] [58].

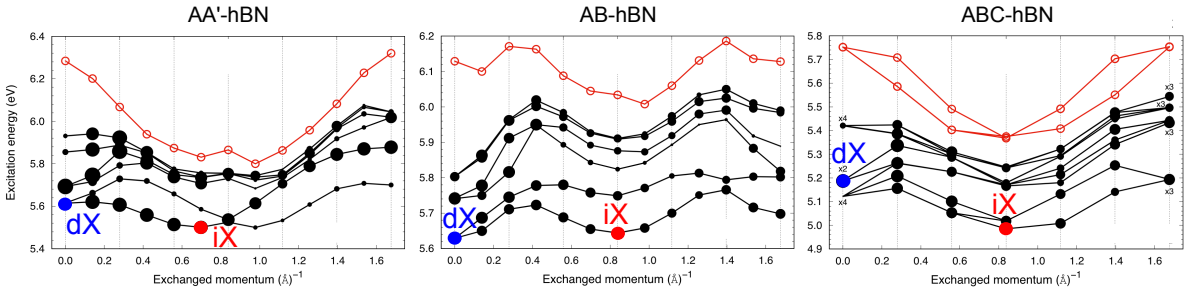

Figure 1.13: Excitonic dispersion of AA'-hBN, AB-hBN and ABC-hBN calculated by *Sponza et al.* where the direct and indirect excitons are represented in blue and red, respectively. [32]

Due to its indirect nature, iX does not directly couple to light through the dipolar interaction. Since iX is located at the T point outside the light cone, it requires the absorption (emission) of a phonon at T to interact with light inside the light cone, thus fulfilling the momentum conservation. Therefore, the creation and recombination of iX are made through phonon-assisted absorption and emission processes, respectively, involving phonons at T. Phonon-assisted processes are generally much less efficient compared to the direct dipolar processes so that indirect

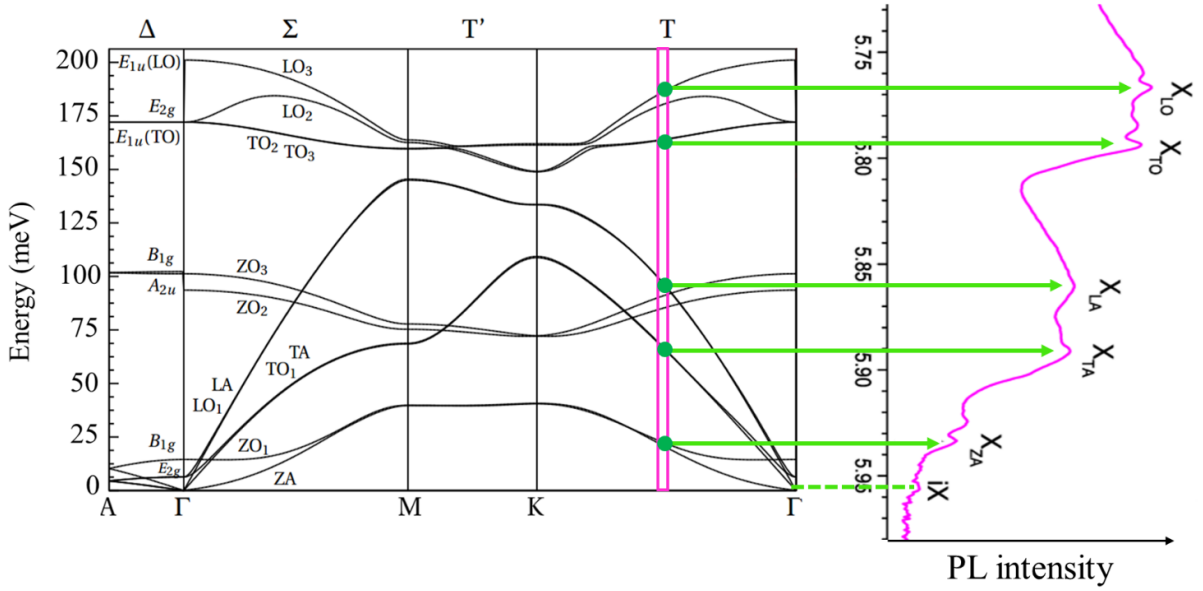

Figure 1.14: (right side) PL spectra of bulk h-BN at cryogenic temperature [7] [71] plotted at the same scale as the phonon dispersion [43] (left side); the energy of the indirect exciton (iX) coincides with the zero-phonon energy.

bandgap semiconductors are usually considered as bad light emitters. This scenario was shown to be drastically different in AA'-hBN which, despite its indirect bandgap, shows a strong intrinsic bandgap emission with an efficiency (∼50 %) [72] comparable to those of direct bandgap semiconductors misleading many researchers to claim the direct nature of the AA'-hBN bandgap [6]. In 2016, *Cassabois et al.* showed that the series of lines between 5.7-6 eV correspond to the phonon-assisted emission of iX where each phonon replica involves a different phonon in T, as depicted on Fig.1.14, thus demonstrating the indirect nature of the fundamental bandgap of AA'-hBN, with iX∼5.95 eV [7]. The line profile of the phonon replicas is characterized by a steep increase on the low-energy side, which results from the 3D joint density of states, and a long energy tail on the high-energy side corresponding to the thermal distribution of indirect excitons around iX following a Boltzmann law [7]. Additionally, the linewidth of phonon replicas increases with the phonon group velocity. Moreover, each phonon replica is escorted by a series of ∼6 meV separated peaks on the low-energy side arising from overtones of LO_1/TO_1 phonons at Γ [73].

Because of the selection rules associated with the symmetry of the lamellar structure of hBN, the phonons involved in the phonon-assisted processes depend on the polarization of the absorbed (or emitted) photons with respect to the basal plane of hBN. In that respect, different phonon replicas are observed depending on the in-plane and out-of-plane light polarization. In AA'-hBN, the phonon-assisted processes associated with in-plane polarized photons only involve phonons with E_{1u} or E_{2g} symmetries, all corresponding to in-plane phonons, while out-of-plane polarized photons only involve phonons with the B_{1g} symmetries, corresponding to ZO_2/ZO_3

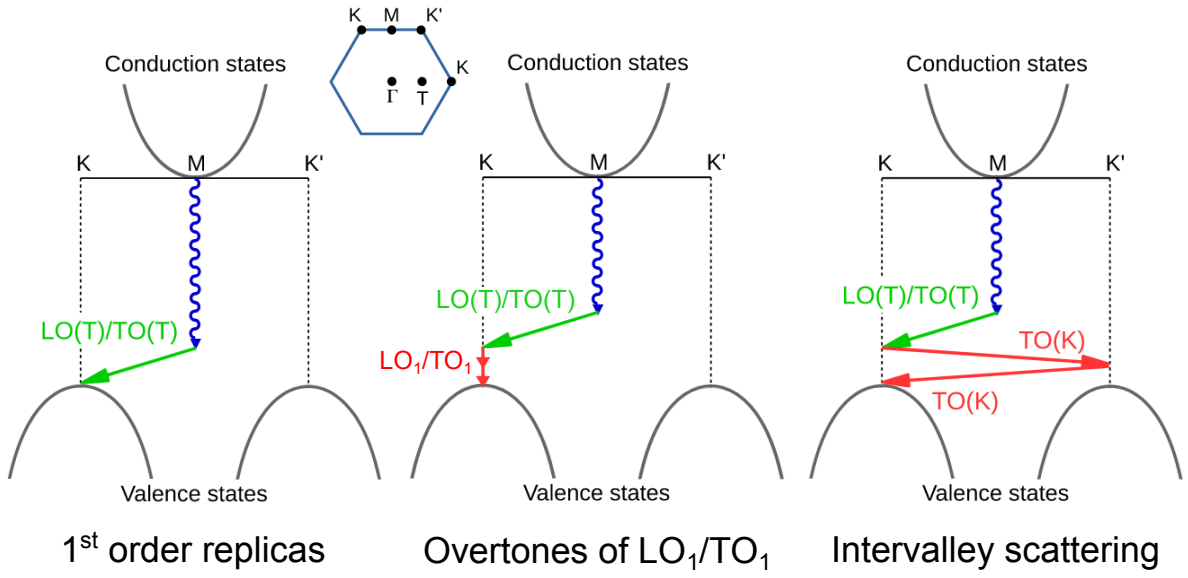

Figure 1.15: Schematic representation of the different phonon-assisted processes involved in the intrinsic indirect emission of AA'-hBN. The blue wavy arrows represent the emission of a photon, the green the emission of a phonon at T and the red arrows represent the emission of additional phonons at Γ and K(K') [73, 74]. A top view of the BZ is shown in the inset.

only, resulting in distinct phonon replicas [71].

Higher-order phonon-assisted processes can involve the emission of multiple TO_3 phonons at K(K') with an energy of 148 meV leading to an intervalley scattering between K and K' valleys, as illustrated in Fig.1.15 [74]. This results in a series of higher-order phonon replicas that consist of red-shifted copies of the first-order phonon replicas above 5.7 eV, that are increasingly broadened, as observed in spectrum A of Fig.1.16 [74]. Moreover, the amplitude of the phonon replicas decreases with the order of the phonon-assisted process. Nonetheless, the presence of shallow-level defects give rise to a density of final electronic states within the bandgap that could be resonant with the virtual states at K and K' of the intervalley scattering thus drastically increasing its efficiency. This results to the emergence of an intense band centered ∼5.45 eV which generally dominates the emission spectrum of standard hBN crystals, as observed in spectrum B of Fig.1.16. This defect-related band, which is modulated by the local defects density, appears generally stronger and are localized along domain boundaries and wrinkles in hBN crystals. It is then mainly attributed to extended defects like stacking faults that consist of local change of the stacking between two hBN layers, although other shallow defects are also considered like donor-acceptor pairs or BN divacancy [74, 75]. Following Section 1.2.3, stacking faults induces a local variation of the bandgap energy that may leads to the formation of shallow levels within the bandgap of the dominant stacking [75]. Therefore, the bands below 5.7 eV are commonly referred as the stacking faults emission bands.

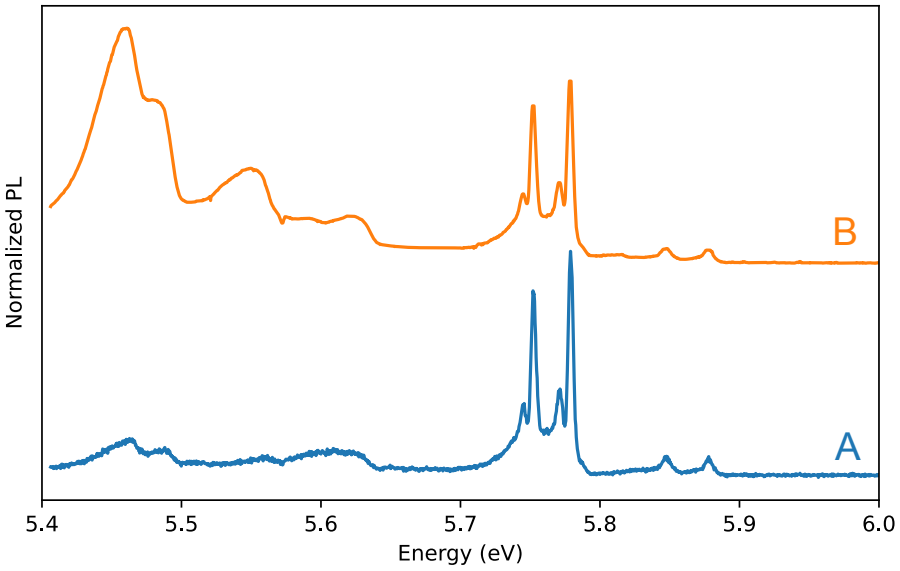

Figure 1.16: Impact of extended defects on the band-edge emission AA'-hBN in the deep-UV: (A) PL spectrum measured on a clean AA'-hBN region showing almost defect-related emission where the signal below 5.7 eV is mainly due to the intervalley scattering alone; (B) PL spectrum measured on a folded AA'-region displaying a strong defect-related emission bands below 5.7 eV that are stronger than the first-order phonon replicas above 5.7 eV.

The direct exciton dX strongly couples to light with an ultra-large oscillator strength due to the many parallel direct transitions between the electronic flat bands along both the K-M and the K-H lines. In the case of bulk material, the light-matter coupling leads to the emergence of a transverse-longitudinal splitting (Δ_{LT}) at the dX resonance, and this splitting is directly proportional to the oscillator strength of dX. In the region where the transverse-longitudinal splitting occurs, the real part of the dielectric function is negative giving rise to the so-called reststrahlen band within which the light is completely reflected. Fig.1.17(a) shows the reflectivity and transmission spectrum of AA'-hBN measured at cryogenic temperature (6 K) in the deep-UV [54]. We then observe a large reststrahlen band [purple region in Fig.1.17(a)] with Δ_{LT}~420 meV arising from the dX resonance at 6.125 eV. The value of Δ_{LT} in AA'-hBN, of the order of half an eV, is almost 20 times larger than what is typically measured in standard semiconductors, that is few or tens of meV, thus demonstrating the extremely large oscillator strength of dX in AA'-hBN [54]. Interestingly, the fine structure observed on the reststrahlen band of dX matches the energy of the phonon replicas in the mirrored image of the PL spectrum of Fig.1.14 [blue spectrum in Fig.1.17]. Therefore, these additional resonances arise from the phonon-assisted absorption of iX, which is depicted in the inset of Fig.1.17(b). While in standard semiconductors, indirect transitions appears as weak absorption bands that cannot be resolved in the reflectivity spectrum, the efficient phonon-assisted processes in hBN stem from the parallel indirect transitions between the electronic flat bands along K-H and M-L lines leading to an effective oscillator strength for the phonon-assisted processes of iX (Δ_{LT}~20 meV) similar to those of direct transitions in other materials [54].

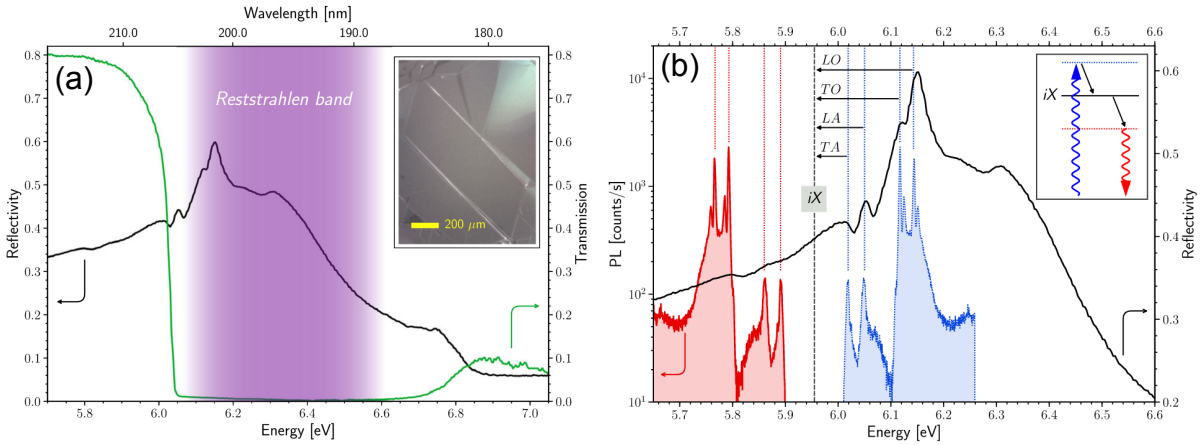

Figure 1.17: (a) Reflectivity and transmission spectrum of AA'-hBN measured at cryogenic temperature (6 K) in the deep-UV. (b) Comparison between reflectivity (black) and photoluminescence (red) of bulk hBN at 8 K. The vertical dashed line at 5.955 eV indicates the energy of the indirect exciton (iX). The dotted blue spectrum corresponds to the mirror image of the PL spectrum with respect to the iX energy.

1.3 Conclusion

In this chapter, I have reviewed the main physical properties of monolayer hBN (Part 1.1) and hBN polytypes (Part 1.2) that will be required to understand the results that will be presented in Chapter 3 and Chapter 4, respectively. Notably, while the physical properties of hBN mainly derive from hBN monolayers, I emphasized the importance of the interlayer interaction.

On the one hand, the strong ionic nature of the BN bonds, coupled with the reduced dimensionality of monolayer hBN, results in a wide optical bandgap, typically measured at ∼6.1 eV in the deep-UV [13]. Furthermore, the low dimensionality of monolayer hBN renders it sensitive to the surrounding dielectric environment, notably the dielectric screening of the Coulomb interaction induced by the substrate that influences both the electronic bandgap energy and the excitons binding energy. Consequently, the optical properties of monolayer hBN exhibit significant versatility, subject to variations depending on the choice of substrates and the fabrication process of the monolayers. However, the understanding of these optical properties remains limited, and the origin of the PL doublet observed at ∼6.1 eV in epitaxial hBN monolayers is still unresolved [13]. Chapter 3 is dedicated to the study of the optical properties of monolayer hBN in the deep-UV for both exfoliated and epitaxial hBN monolayers, with the purpose of elucidating the origin of the emission at ∼6.1 eV.

On the other hand, the modification of the interlayer interaction by the stackings induces a variation of the optical properties of hBN polytypes and, notably, of the energy and nature of the optical bandgap. Moreover, the stacking also influences the crystal symmetry that also impacts the optical properties of hBN polytypes. However, while AA'-hBN displays exceptional

optical properties which have been investigated in details this last decade, the optical properties of other hBN polytypes have not been studied yet due to lack of high-quality crystals. The effect of the stacking on the optical properties of hBN polytypes, through the modification of the interlayer interaction and the crystal symmetry, will be studied in Chapter 4 dedicated to the study of a bernal boron nitride (AB-hBN) crystal.

In the following chapters, I will mainly focus on the study of the optical properties of hBN monolayers (Chapter 3) and hBN polytypes (Chapter 4) using a unique deep-UV microscope which I have developed during my thesis and will be described in the next chapter (Chapter 2).

Chapter 2

Hyperspectral microscopy in the deep-UV

This chapter is dedicated to the description of the UVC microscope that I developed during my PhD. The first version of this microscope operating in the UVB was developed by the former PhD student *Thomas Pelini* to study the optical properties of deep-levels in hBN around ∼300 nm [33]. By upgrading this microscope to the UVC using an optical excitation up to ∼190 nm, the intrinsic optical properties of hBN could be studied at the microscopic scale. In chapter 3, I will demonstrate the use of this microscope in thin hBN layers down to a single atomic layer to study the optical properties of monolayer hBN for different types of samples. In chapter 4, I take advantage of the high spatial resolution of the UVC microscope to identify microscopic domains of hBN polytypes, which allows me to experimentally study for the first time the optical properties of hBN polytypes.

Contents

1.1 Monolayer hBN 8
1.1.1 Microscopic structure and symmetries 8
1.1.2 Vibrational properties 10
1.1.3 Electronic properties 11
1.1.4 Optical properties 12
1.2 hBN polytypes 15
1.2.1 Microscopic structures and symmetries 15
1.2.2 Vibrational properties 20
1.2.3 Electronic properties 23
1.2.4 Optical properties 25
1.3 Conclusion 29

2.1 Context

This part aims to give a general context to deep-UV microscopy. In Section 2.1.1 I make a state-of-the-art review of luminescence microscopy in the deep-UV focusing on the technical constraints and their main limitations. In Section 2.1.2 I present the main physical processes which can be detected via deep-UV microscopy.

2.1.1 Luminescence microscopy in the deep-UV

Luminescence spectroscopy consists of recording the emission of a material after excitation either optically (photoluminescence - PL) or electrically (electroluminescence - EL) or thermally

(thermoluminescence) or by an electron beam (cathodoluminescence - CL). When implemented in a microscope, the luminescence can be spatially resolved down to resolutions allowing to probe the local properties of materials and their spatial variations. Luminescence microscopy techniques are widely used in nanoscience to study the properties of nano-objects like atomic defects, quantum dots, carbon nanotubes, or 2D materials. Therefore, the spatial resolution plays an important role in luminescence microscopy. Moreover, the temperature has usually dramatic effects on the luminescence of materials such as a reduction of the intensity and a spectral broadening. The ability to cool the sample down to cryogenic temperatures then represents a significant advantage.

One of the most commonly used techniques is PL spectroscopy which consists of the optical excitation of the luminescence by any kind of light source (laser or incoherent). A standard way to study the PL of semiconductors is to excite the material with an excitation at an energy higher than its electronic bandgap. The optical excitation generally lies from the near-IR to the near-UV range for standard semiconductors. In these ranges, PL microscopy can be easily implemented due to the broad variety of light sources and optics with relatively low optical aberrations. On the other side, for wide bandgap semiconductors like hBN, the optical excitation should lie in the deep-UV which is technically more challenging. This is mainly due to the huge optical aberrations induced by the chromatic dispersion of dielectric media in this range together with the lack of efficient laser sources. Moreover, the propagation of UV light in air is limited by the oxygen absorption for wavelength below $\sim$190 nm thus constraining the optical spectroscopy at ambient conditions in the deep-UV. For all these reasons, PL microscopy in the deep-UV was nonexistent until 2019 and one should wait for 2020 with this thesis for the first confocal PL microscope in the deep-UV.

An alternative technique used for wide bandgap semiconductors is CL microscopy which can be performed inside a scanning electron microscope (SEM). The excitation is provided by an accelerated electron beam with energies on the order of few keV, well above the bandgap, and a typical spatial resolution on the order of $\sim$10 nm beyond the reach of any optical microscopy even in the UVC. The SEM chamber is kept under ultra-high vacuum (UHV) to avoid any atomic collision with the electron beam and the samples can be cooled down to cryogenic temperatures. Correspondingly, CL microscopy has been the only technique used to study the optical properties of hBN until 2014. Following the first synthesis of high-quality bulk hBN in 2004, *Watanabe et al.* observed for the first time the intrinsic emission of hBN by CL spectroscopy [6]. Later, *Bourrelier et al.* used CL microscopy in a TEM to reveal the effect of stacking faults on the intrinsic luminescence of hBN [75]. In 2019, *Schué et al.* studied by CL the optical properties of thin exfoliated flakes made of few atomic layers down to 6 atomic layers while they could not measure any signal for hBN thicknesses below [76]. This is probably due to the small interaction cross-section of the incident electrons with thin layers decreasing rapidly with the hBN thickness. Therefore, CL microscopy has proven to be inefficient for thin film materials with atomic

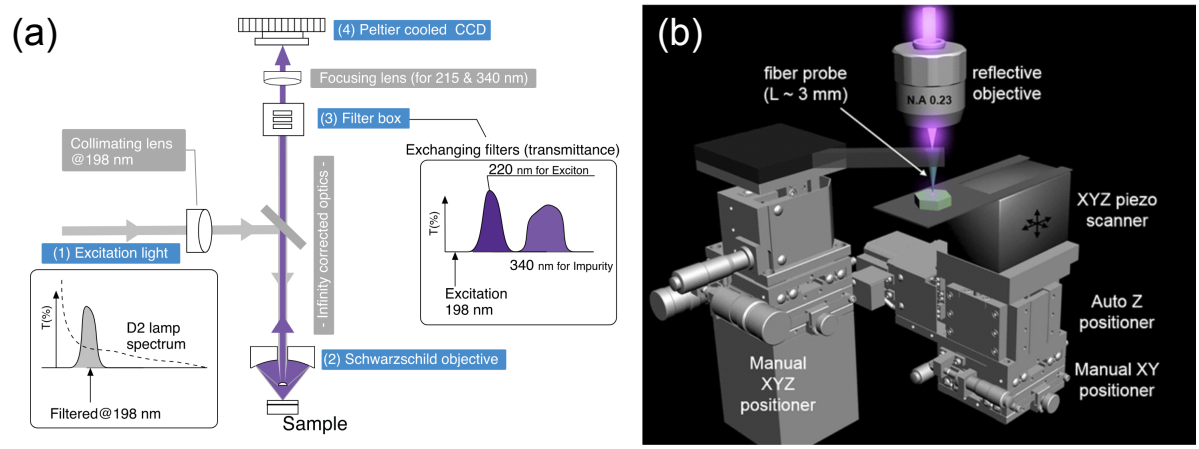

Figure 2.1: Luminescence microscopy techniques in the deep-UV : (a) Optical scheme of the wide field PL microscope in the deep UV developed by *Watanabe et al.* [77] ; (b) 3D modelization of the scanning near field optical microscope in the deep-UV developed by *Ishii et al.* [78].

thicknesses like few-layer and monolayer hBN thus requiring an alternative technique.

PL microscopy is widely used to study 2D semiconductors down to a monolayer with a bandgap in the visible like transition metal dichalcogenides (TMDs) or black phosphorus thus demonstrating its ability to probe atomically thin layers. However, as mentioned above, PL microscopy in the deep-UV turns out to be very challenging. By overcoming the technical difficulties associated with the deep-UV, *Watanabe et al.* developed in 2019 the first wide-field PL microscope operating in the deep-UV [77]. The optical excitation was provided by a deuterium lamp filtered at 198 nm which was focused by a reflective objective over a 100-400 µm-large area on the sample surface. The sample was studied at room temperature in an ambient environment. The PL signal emitted from the illuminated area was then collected back to a CCD camera recording the wide-field PL image. The image can be spectrally filtered to only measure the emission of the intrinsic or shallow defects. The spatial resolution of this wide-field microscope is ~10 µm, far from the light diffraction limit in this range (250 nm). Moreover, the use of an incoherent light source in the wide-field configuration leads to a small excitation density of 1-10 W/m^2. Therefore, they could only detect PL signals for hBN thicknesses of a few hundred of nanometers while the signal from thinner layers was too weak to be detected.

The same year, *Ishii et al.* developed the first deep-UV scanning near-field optical microscope (SNOM) operating at room temperature where the optical excitation is provided by the fourth-harmonic of a Ti:Sa laser up to 210 nm with a maximum output power of 20 mW [78]. The power and the alignment of the excitation are dynamically controlled through feedback loops. The incident light is focused with a reflective objective on the entrance of an optical fiber which guides the light to the other extremity of the fiber in proximity with the sample. The evanescent light at the apex of the probe then excites the PL of the sample which is collected back through

the fiber and the objective to a grating spectrometer which measures the PL spectrum. By recording the PL spectrum at each point of the sample they could acquire hyperspectral PL images in the deep-UV. They estimated the spatial resolution to be on the order of 150 nm. They used this deep-UV SNOM to study the optical properties of an $Al_{0.8}Ga_{0.2}N$/AlN quantum well (QW) with a typical emission up to ~250 nm. However, the excitation energy (~5.9 eV) being below the hBN bandgap, a higher excitation energy would be required to study the optical properties of hBN using this setup.

2.1.2 Physical processes

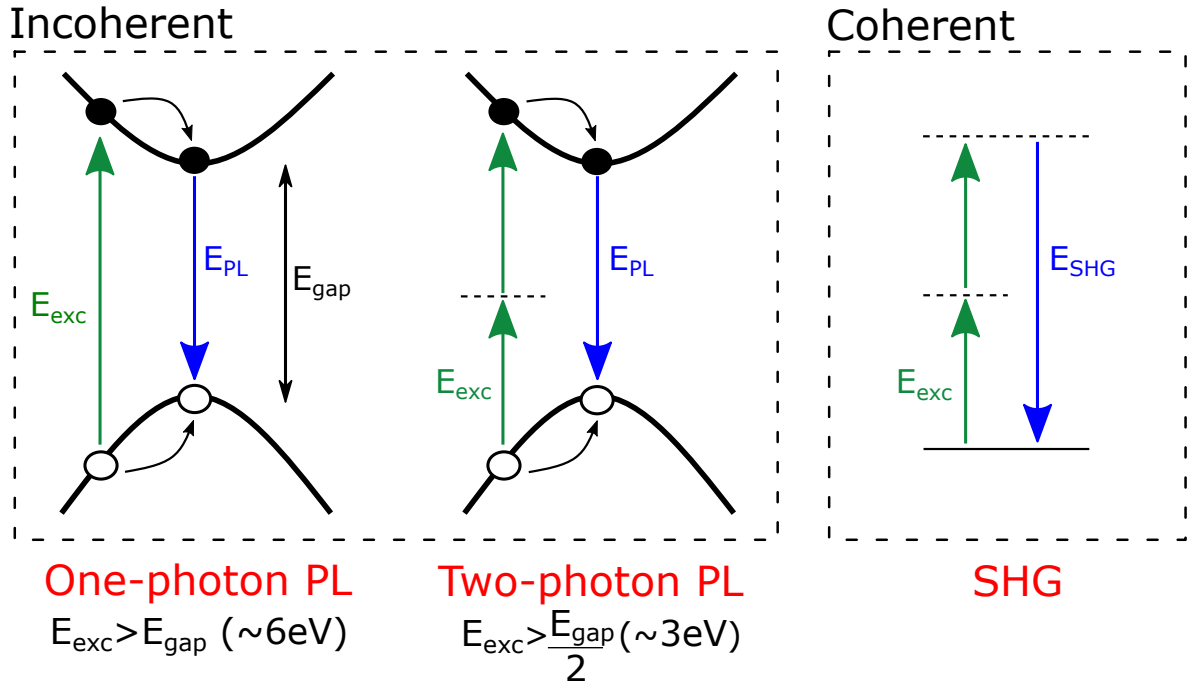

Figure 2.2: Schematic representation of the three main physical processes that can be studied in our deep-UV microscope.

The optical excitation of a material induces many different physical processes which can occur in parallel. In this thesis, we focus on three main physical processes which are represented in Fig.2.2. For all these processes the excitation and the signal are represented by the green (E_{exc}) and the blue ($E_{PL/SHG}$) arrows on Fig.2.2, respectively. The one-photon PL process consists of the absorption of a single photon with an energy greater than the material bandgap ($E_{exc} > E_{gap}$). In contrast, the two-photon PL process consists of the simultaneous absorption of two photons with the same energy through a non-linear optical process called two-photon absorption. As a consequence, the excitation energy must be at least half the material bandgap ($E_{exc} > \frac{E_{gap}}{2}$). The PL is an incoherent process that relies on the absorption of the excitation by the material. For both PL processes, the absorbed excitation creates electron-hole pairs which relax to lower energy states before recombining radiatively by spontaneous emission of photons

with an energy $E_{PL} \neq E_{exc}$. The PL spectrum is then constituted by all photons related to the different transitions inside the excited material. Besides, SHG is a non-linear optical process where two photons of the same energy are transformed into one photon with twice their energy. Whereas the one- and two-PL signals result from incoherent processes that require absorption by the material, SHG is a coherent process that can be observed in the transparency domain of the material since it only involves virtual levels. However, the efficiency of the SHG can be greatly improved near the resonances of the material bandgap ($E_{exc} > \frac{E_{gap}}{2}$).

In the second part of this chapter I will present the home-built deep-UV microscope that I developed during my PhD, represented schematically in Fig.2.3. This unique microscope worldwide can operate in the deep-UV at cryogenic temperatures (4 K) with a high spatial resolution of ∼200 nm [79]. It enables spatially-resolved PL microscopy in the deep-UV with a tunable excitation energy up to 6.5 eV(∼190 nm). Moreover, by using an optical excitation in the near-UV (∼400 nm), we could extend the use of our microscope for hBN to complementary optical techniques like SHG microscopy or two-photon PL. A general description of our deep-UV microscope is given in Part 2.2.

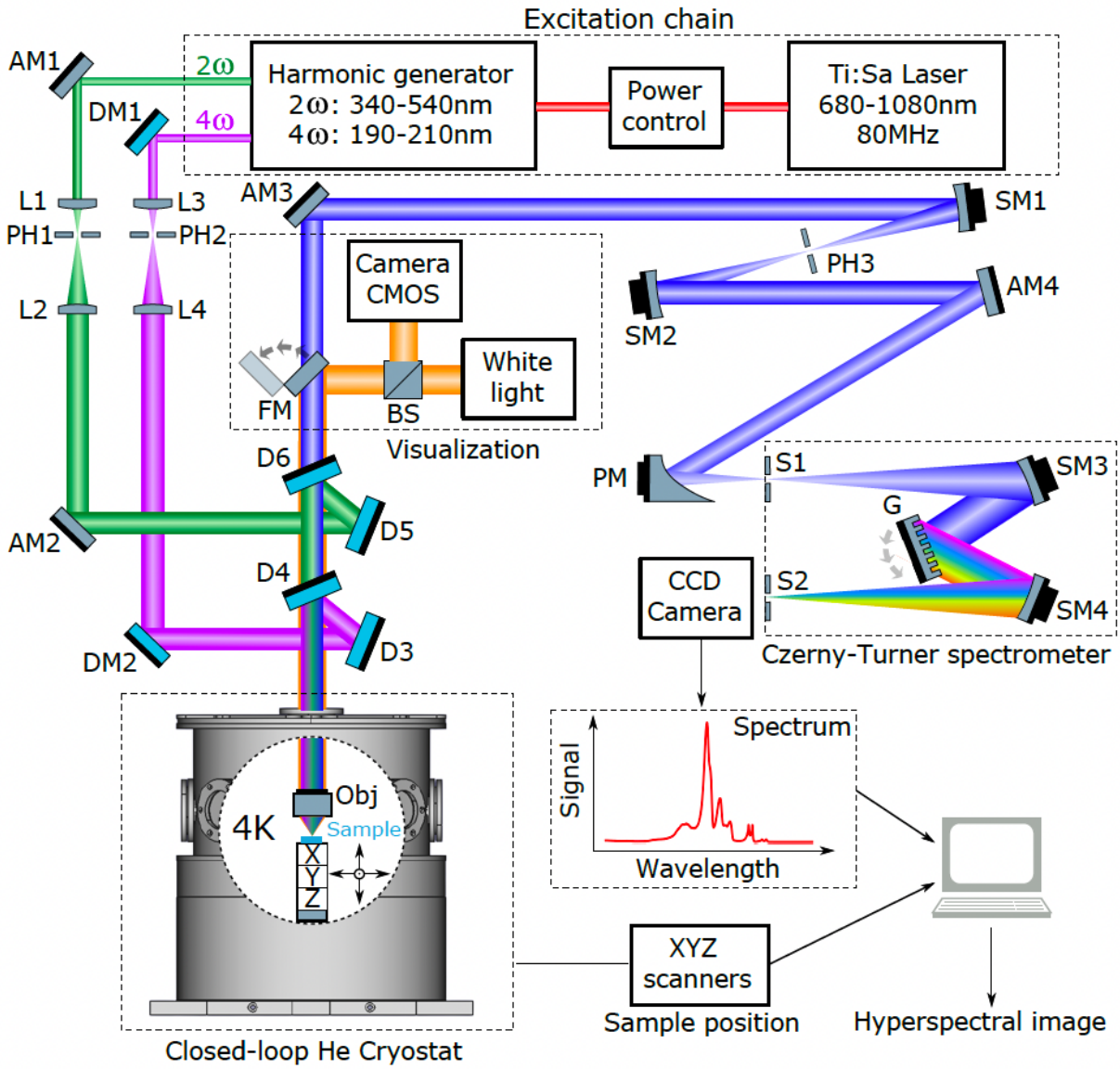

Figure 2.3: General scheme of the home-built confocal micro PL setup operating in the deep-UV at cryogenic temperatures. The legend of the optical components is the following: aluminium mirrors (AM1/2/3), dielectric mirrors (DM1/2), lenses (L1/2/3/4), pinholes (PH1/2/3), dichroïc mirrors (D3/4/5/6), flip mirror (FM), beam splitter (BS), spherical mirrors (SM1/2/3/4), parabolic mirrors (PM), slits (S1/2) and grating (G)

2.2 Deep-UV microscope

This part is dedicated to the description of our deep-UV microscope which will be decomposed into four parts. The generation and the injection of the excitation to the cryostat will be treated in Section 2.2.1. The control of the sample environment inside the cryostat and how the excitation is focused and scanned over the sample are treated in Section 2.2.2. The signal collection and detection through a grating spectrometer will be treated in 2.2.3. Finally, the overall acquisition process is controlled by a Python-written software allowing to record complex hyperspectral images which will be described in Section 2.2.4.

2.2.1 Deep-UV excitation

There are two possible optical excitations in our setup, either provided by the second (2ω) or by the fourth harmonic (4ω) of a continuous-wave (cw) mode-locked Ti:Sa laser (Chameleon Ultra II - Coherent©) as depicted in Fig.2.4. The Ti:Sa laser produces trains of 140 fs pulses at 80 MHz repetition rate, tunable from 680 nm to 1080 nm with ∼4 W output power. The harmonics of the fundamental frequency (ω) produced by the Ti:Sa laser are generated inside a commercial harmonics generator (HarmoniXX FHG - APE©) through the combination of second-order non-linear optical processes inside non-linear crystals (see Fig.2.4).

The generation of harmonics through non-linear processes outside a cavity is made possible by the use of the femtosecond pulses produced by the Ti:Sa laser reaching high peak power on the order of hundreds of kW. Efficient non-linear generation can only occur near the phase-matching conditions given by the second-order dielectric susceptibility tensor of the non-linear crystal. Therefore, the phase matching conditions depend both on the relative crystal orientation and the wavelength of the involved photons in the non-linear process. Correspondingly, the non-linear crystals, which consist of barium borate (BBO) crystals, are cut along specific crystalline orientations in regard to the phase matching of a non-linear process at a given spectral range. The phase-matching conditions are then fulfilled for different input wavelengths by tilting the non-linear crystals with respect to the optical axis. The grazing incidence thus defines the limit of the operational spectral range of the non-linear process.

The three harmonics (2ω, 3ω and 4ω) are generated from the combination of second-order non-linear processes inside three different BBO crystals. The two types of second-order non-linear processes involved in the harmonics generation are the second harmonic generation (SHG) and the sum frequency generation (SFG). While the first one consists of the conversion of two identical photons to a photon with twice the energy [SHG - Fig.2.4], the second one consists of the conversion of two photons with different energies into a photon with an energy equal to the sum of their energies [2+1/3+1 - Fig.2.4]. The generation of 4ω from frequency-doubling of 2ω ($2 + 2$) induces phase matching conditions which are limited to a wavelength of 210 nm below the hBN bandgap in the optimal cutting orientation of BBO crystals. Alternatively, 4ω can be

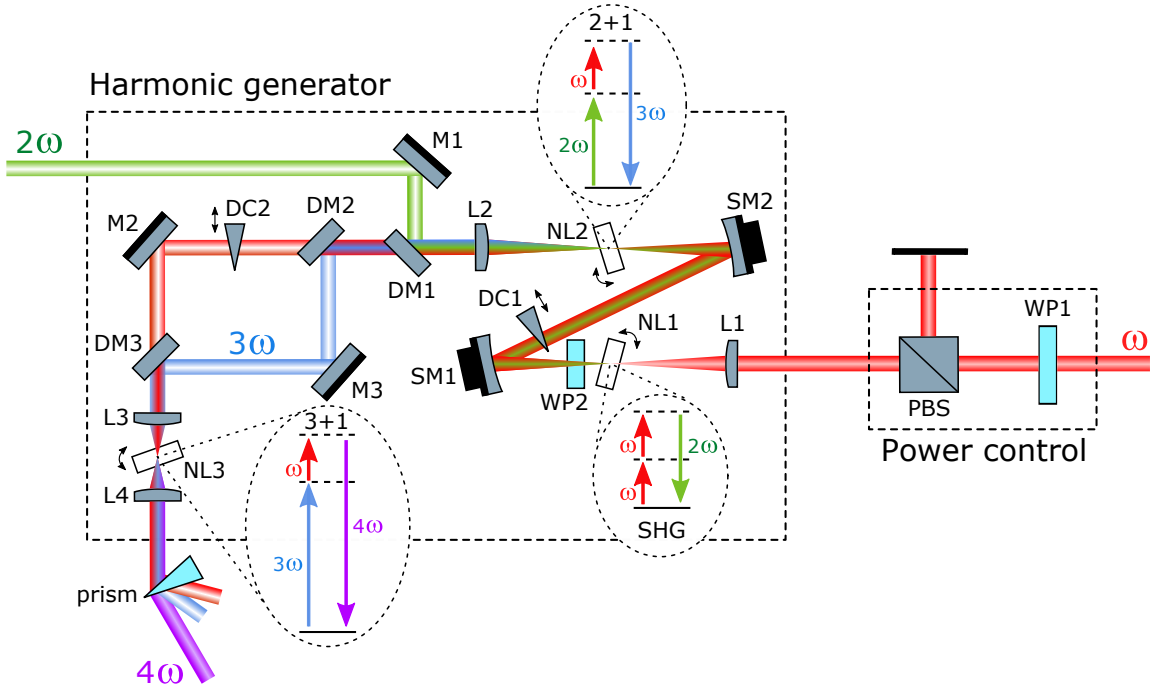

Figure 2.4: Scheme of the harmonic generator and the power control. The optical components are labeled as follows: wave plates (WP1/2), polarized beam splitter (PBS), lenses (L1/2/3/4), delay compensators (DC1/2), non-linear crystals (NL1/2/3), mirrors (M1/2/3), spherical mirrors (SM1/2) and dichroïc mirrors (DM1/2/3).

generated through sum-frequency of the third harmonic (3ω) and the fundamental ($3+1$) where the phase matching conditions are possible from 190 nm to 210 nm allowing an optical excitation above the hBN bandgap (λ <204 nm). We thus choose this last configuration for the harmonic generator (see Fig.2.4).

The 2ω beam is obtained through SHG in the first BBO crystal (NL1) by focusing the horizontally polarized Ti:Sa laser beam with a lens (L1) at the entrance of the harmonics generator. The 2ω beam and the remaining fundamental beam out of the BBO crystal are recollimated by a spherical mirror (SM1). The 3ω signal is obtained by SFG of the 2ω and the fundamental (2+1) beams in the second BBO crystal (NL2). A tunable half-wave plate (WP2) ensures the input pulses are horizontally polarized whereas a tunable delay compensator (DC1) makes the two pulses arrive at the same time on NL2 required for SFG. The three output beams, fundamental, 2ω and 3ω, are recollimated with a lens (L2). The 2ω beam can be separated from the others by using a dichroïc mirror (DM1) and then exiting the harmonics generator. The 4ω beam is obtained by SFG of the 3ω and the fundamental (3+1) beams in the third BBO crystal (NL3). The fundamental pulse is separated from the 3ω with a second dichroïc mirror (DM2) to be delayed with a tunable delay compensator (DC2) for temporal overlap on NL3. The two pulses

are recombined with a third dichroïc mirror (DM3) before being focused with a lens (L3) on NL3. The 4ω signal mixed with the two other beams is recollimated before spectral separation by a prism outside the harmonic generator.

The cut of the BBO crystals has been optimized for the corresponding non-linear processes to be efficient for fundamental wavelengths near ∼800 nm. A summary of the typical spectral range and maximum power of the different harmonics at the exit of the harmonics generator, in comparison with the fundamental, is presented on Tab.2.1. A motorized half waveplate (WP1) and a polarized beamsplitter (PBS) before the harmonics generator allow to vary the power of the fundamental beam before the harmonics generator and thus the power of the harmonics.

	Fundamental	2ω	3ω	4ω
Spectral range	680-1080 nm	340-540 nm	227-360 nm	190-210 nm
Max power	4 W	∼1 W	∼100 mW	∼1 mW

Table 2.1: Specifications of the operational spectral range and maximum optical power of the different harmonics.

To route the 2ω beam to the sample inside the cryostat we used an optical path made of UV-enhanced aluminium mirrors (AM1/2 in Fig.2.3). Because the reflectivity of UV-enhanced aluminium mirrors drops drastically below 210 nm we used dielectric mirrors (DM1/2) designed for Excimer lasers with the maximum reflectivity around 194 nm for routing the 4ω beam. Both excitation beams are collimated and enlarged using two telescopes (L1/2 and L3/4) such that the beam's dimension matches the objective pupil diameter in order to reach the diffraction limit on the sample. A spatial filter is added at the focus of the two telescopes to obtain gaussian beams of improved quality for the excitation spot on the sample.

Before the cryostat, we use dichoïc mirrors to inject the excitation beams and collect the signal from the sample. Due to the lack of commercial dichroïc mirrors matching our specifications, we use two different custom-made dielectric mirrors designed by *Layertec* for both excitations. The choice of the design has been made such that they reflect the excitation in the range 320-420 nm and 188-195 nm for the 2ω and the 4ω, respectively, and both transmit the signal in the range of 200-260 nm. Such a design was not achievable at 45° incidence so we chose a design at 22.5° incidence. We thus combine two dichroïc mirrors with 22.5° incidence for the two excitation paths, as represented in Fig.2.3 (D3/4 and D5/6). Depending on the experiment, the last dichroïc mirror (D4 or D6), placed on a magnetic mount, is easily removed.

2.2.2 Sample cryogenic environment

The excitation is injected inside the cryostat through a transparent CaF_2 window. To focus the excitation on a diffraction-limited spot at the sample surface, we use a reflective Schwarzschild objective made of UV-enhanced aluminium mirrors (LMM40x-UVV - Thorlabs©)

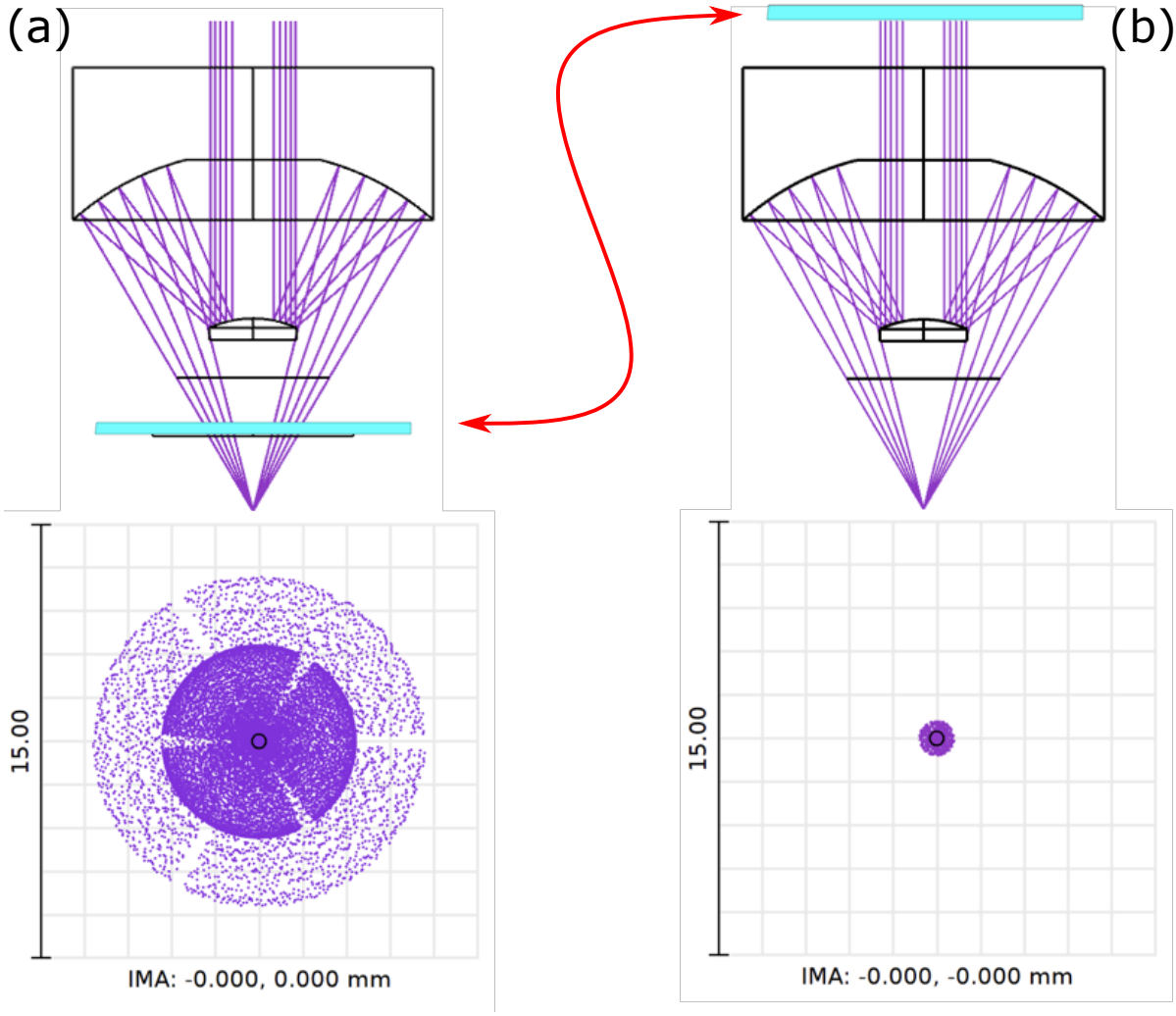

Figure 2.5: Zeemax simulations of the spot size at 200 nm for the objective before the cryostat window (a) and after the cryostat window (b).

with a numerical aperture (NA) of ∼0.5 and 7.8 mm working distance. A Schwarzschild objective consists of a primary concave mirror, with a hole in the middle for the pupil, and a smaller secondary convex mirror in front of the pupil held by three spider vanes as shown in Fig.2.5. Despite the obscuration losses caused by the design, this objective has the advantage of being completely achromatic on a broad spectral range from the deep-UV (∼200 nm) to the mid-infrared (∼20 µm) for UV-enhanced aluminium mirrors. Both the focal length and the numerical aperture are wavelength-independent. The diffraction limit (d_{min}) of an objective is defined by the expression :

$$d_{min} = 0.61\frac{\lambda}{NA} \tag{2.1}$$

with λ the optical wavelength. Correspondingly, the diffraction limit for 2ω and 4ω are 490 nm and ∼250 nm, respectively. In order to reach the diffraction limit, the input beam must be

a well-collimated gaussian beam matching the objective pupil diameter, which is the case for both excitation beams as seen in the previous section. Very importantly, the objective must be placed inside the cryostat in order to avoid any geometrical aberration induced by the cryostat window to reach a diffraction-limited spot at the surface of the sample. If the objective was placed before the cryostat window, the focused light would arrive with a large range of angles of incidence on the window inducing geometrical aberrations which would broaden the spot. This effect becomes particularly important in the UV due to the variations of the real part of the optical index at short wavelengths in dielectric materials following the standard chromatic dispersion of dielectric media: $n(\lambda) = A + \frac{B}{\lambda^2}$. Alternatively, if the objective is placed inside the cryostat, the light crosses the window in a collimated beam with no incidence angle, avoiding any geometrical aberration. By performing Zeemax simulations, we could compare quantitatively the spot broadening in the two situations. If the objective is placed before the window we obtain a spot size of 20 µm at a wavelength of 200 nm (see Fig.2.5(a)). If the objective is placed inside the cryostat, the resulting spot size is 300 nm at 200 nm (see Fig.2.5(b)) very close to the ideal diffraction limit. The depth of field (DOF) is defined as :

$$DOF = \frac{\lambda\sqrt{1 - NA^2}}{2NA^2} \tag{2.2}$$

is estimated to be ∼700 nm and ∼350 nm for 2ω and 4ω.

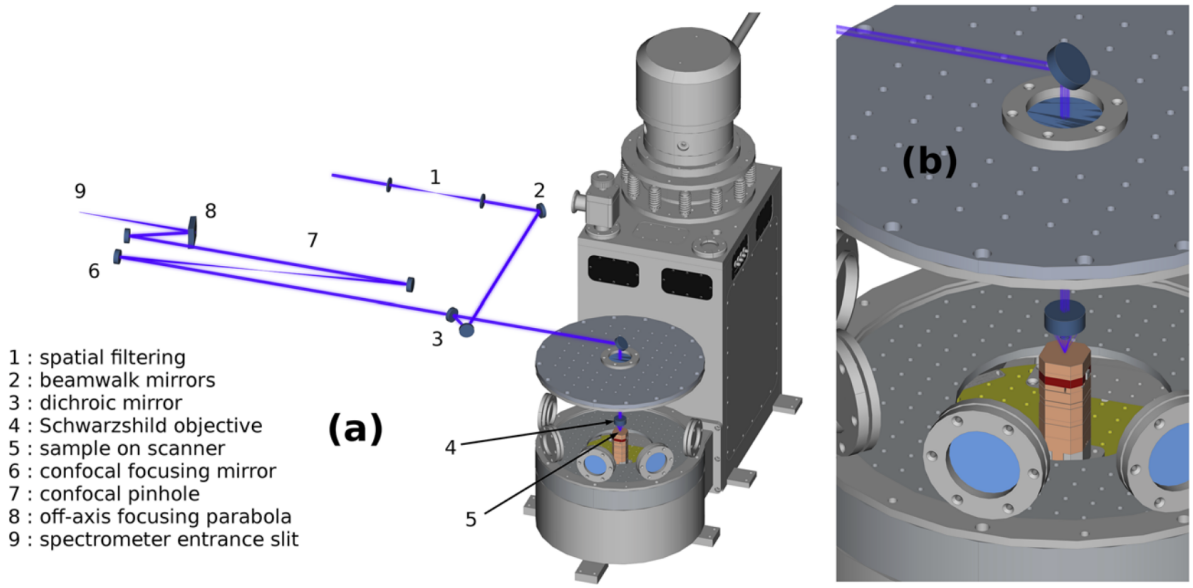

Figure 2.6: 3D view of the cryostat with the simulated beam path for the objective installed inside the cryostat, from Ref. [79].

In confocal PL microscopy, spatial mapping is commonly realized by moving the excitation spot over the fixed sample surface via a steering mirror placed before the cryostat inducing variations of the incidence angle of the excitation beam on the pupil of the objective. This mapping

technique is widely used in the visible and the near-IR because of the small aberrations in this range. However, because of the huge geometrical aberration in the deep-UV, this mapping technique must be precluded in our setup. Alternatively, the spatial mapping in our setup is realized by moving the sample relatively to the fixed excitation spot via a set of piezoelectric scanners installed under the sample holder. Therefore, the excitation beam always keeps a normal angle with the cryostat window and the objective along the mapping with the same spatial resolution.

The cryostat is a low-vibration closed-loop He cryostat (Optidry250) manufactured by MyCryoFirm© operating at low temperature (4 K), and designed with a large chamber in order to mount the objective inside and the tower of scanners, see Fig.2.6. The objective is fixed to an aluminium tube directly connected around the cryostat window just above the sample holder as represented in Fig.2.6. The cryostat is pumped at ultra-high vacuum ($\sim 10^{-11}$bar) to isolate thermally the cold plate with the sample from the rest of the cryostat. The cold plate at 4 K is protected from the thermal radiations of the chamber and the objective through two consecutive thermal shields typically at 50 K and 10 K. The thermal shield at 50 K has been extended around the sample holder to protect it against thermal radiations mainly arising from the objective kept at room temperature. The temperature of the sample is controlled from 4 K up to room temperature with a heating resistance under the sample and two thermal probes on the sample and the cold plate, respectively.

The mechanical vibrations of the cold head caused by the He rotary valve are damped by different stages of mechanical decoupling so that the root mean square of the vibrations on the sample and the scanners are less than 30 nm. The sample holder is fixed on the top of a stack of XYZ closed-loop piezoelectric scanners (ANSxyz100/LT/UHV - Attocube©), with a scan range of 30 µmx30 µmx15 µm at $T\sim$4 K, and XYZ piezoelectric steppers (ANPz101eXT12/LT/UHV). While the steppers are used for long-range displacements ($\sim$1 cm) to align the sample with the objective field, the scanners are used to scan the sample surface with sub-nanometric positioning for the hyperspectral acquisitions.

A visualization system made of a white light source, a beam splitter (BS), and a CMOS camera, shown in Fig.2.3, allows to image of the sample inside the cryostat. The incoherent white light emitted by the lamp is transmitted by the BS to a motorized flip mirror (FM) on the detection path after the dichroïc mirrors (D4/6). When the flip mirror is down, the white light is injected inside the cryostat through the dichroïc mirrors which are transparent in the visible, and then focused by the objective on the sample. The light reflected by the sample is then collected back by the objective through the same optical path before being reflected by the BS on the CMOS camera in order to image the sample. Then, by moving the sample with the steppers, the working area at the focus of the objective can be aligned with the area of interest in the sample. When the flip mirror of the visualization is up, the signal collected by the objective from the sample follows the detection path to the spectrometer to measure its spectrum.

2.2.3 Signal collection and detection

The detection path is represented in Fig.2.7. When the sample surface is placed at the focus of the objective, the excitation is focused in a diffraction-limited spot on the sample surface over an area $S_{exc} = \pi.(\frac{d_{min}}{2})^2$ [purple area on Fig.2.7]. The optical excitation then induces different physical processes which have been described in Section 2.1.2. The signal emerging from the sample is then achromatically collected by the objective and transmitted (T∼80 %) by the dichroïc mirrors (D4/6 on Fig.2.7). Because the signal (λ_{sig}) and the excitation (λ_{exc}) wavelengths are different the corresponding diffraction limits are also different. In the case of a point emitter, the effective spatial resolution is given by the smallest of the diffraction limits between the signal and the excitation. For the 2ω excitation, the spatial resolution is given by the diffraction limit of the signal. For the 4ω excitation, the diffraction limit between the signal (λ_{sig}∼210 nm) and the excitation (λ_{sig}∼190 nm) are similar. However, the signal emerges from an area [orange area on Fig.2.7] typically larger than S_{exc} due to light (signal or excitation) or carriers diffusion inside the sample. Consequently, the effective spatial resolution is limited to the photo-generated area which is larger than the excitation diffraction limit.

In order to reach the best spatial resolution near the diffraction limit, we only collect the signal emerging from the excitation spot using a confocal filter allowing us to reject the signal outside a collection area represented by the dashed circle in Fig.2.7. The image of the collected signal is formed on the conjugated plane of a 25 cm focal length spherical mirror (SM1). From the focal length ratio between the objective (5 mm) and SM1, the image is magnified 50 times and the image of the excitation spot correspond to a diameter of 24 µm (12 µm) for the 2ω (4ω) excitation, respectively. Then, by aligning a 20 µm pinhole (PH3 on Fig.2.7) in the focal plane of SM1, only the image of the signal inside the pinhole and at the vicinity of the excitation is transmitted whereas the rest of the signal is filtered out. The signal transmitted by the pinhole is thus conjugated to a collection area on the sample [dashed circle on Fig.2.7] with a diameter of 600 nm. The signal transmitted by the confocal filter is then recollimated by a second spherical mirror SM2 identical to SM1 inducing no magnification of the signal beam.

Finally, the emitted spectrum is measured by a 500 mm focal length Czerny-Turner spectrometer (Shamrock - Andor) with a back-illuminated UV-coated 2048x512 CCD camera (Newton - Andor). The spectrometer is equipped with three gratings (300 rpm, 1200 rpm and 1800 rpm) blazed at 300 nm. The signal is focused on the entrance slit (S1) of the spectrometer by a 22.5° off-axis parabola matching the f-number of the spectrometer. The signal inside the slit, which width can be tuned from 10 to 2500 µm, is transmitted inside the spectrometer and recollimated onto the grating by a 500 mm spherical mirror (SM3 on Fig.2.3). The signal is then dispersed by the grating along the x direction and refocused by another 500 mm spherical mirror (SM4 on Fig.2.3) on the pixels of the CCD camera. The light dispersion depends on the grating, and the spectral range of the dispersed light measured by the CCD camera is controlled through the grating tilt. Each column of the CCD camera is associated with a wavelength. Each wavelength

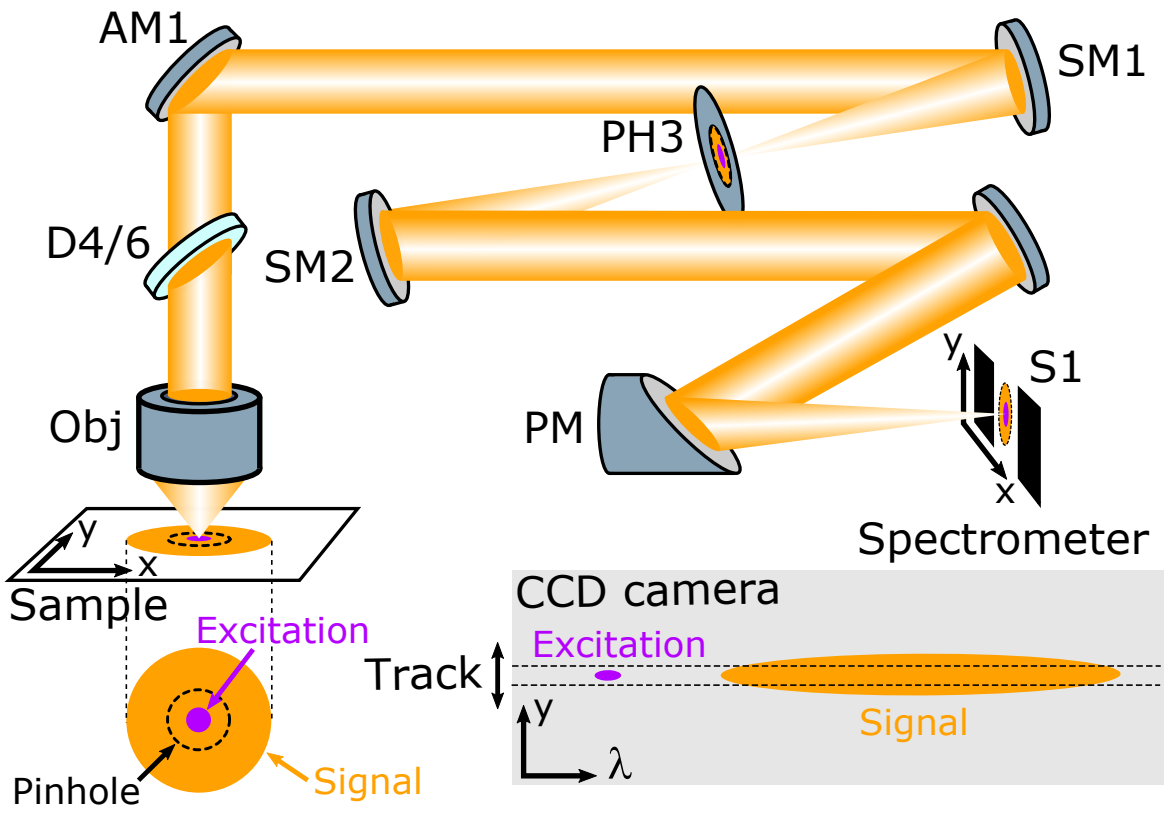

Figure 2.7: Scheme of the detection path where the optical components are labeled after the labeling of Fig.2.3.

on the CCD camera corresponds to an image of the signal through S1. Therefore, S1 is close to the minimum width to obtain the best spectral resolution as depicted in Fig.2.7. The dispersion along y on the CCD camera corresponds to the spatial distribution of the signal along this direction inside the detection area. The camera firmware allows the integration of the spectrum over a track delimited by two rows of the CCD to increase the signal-to-noise (SNR) ratio. By selecting a narrow track centered on the spot associated with the reflected excitation on the CCD, we can also reject the signal emitted outside the excitation area if not rejected by the pin-hole before.

2.2.4 Software control and hyperspectral acquisition

A significant improvement that I brought to this setup was to switch the experiment control software, previously in Labview, to a modular open-source Python framework named Qudi [80] which is more handy, flexible, and allows advanced tasks. The Qudi framework is based on a three-layer architecture where the tasks are separated into the *hardware*, *logic*, and *GUI modules* allowing better reliability and flexibility of the code. The *hardware modules* handle the communication with devices, and translate a set of generic instructions into device-specific commands. The *logic modules* supervise the *hardware modules* and perform acquisition control.

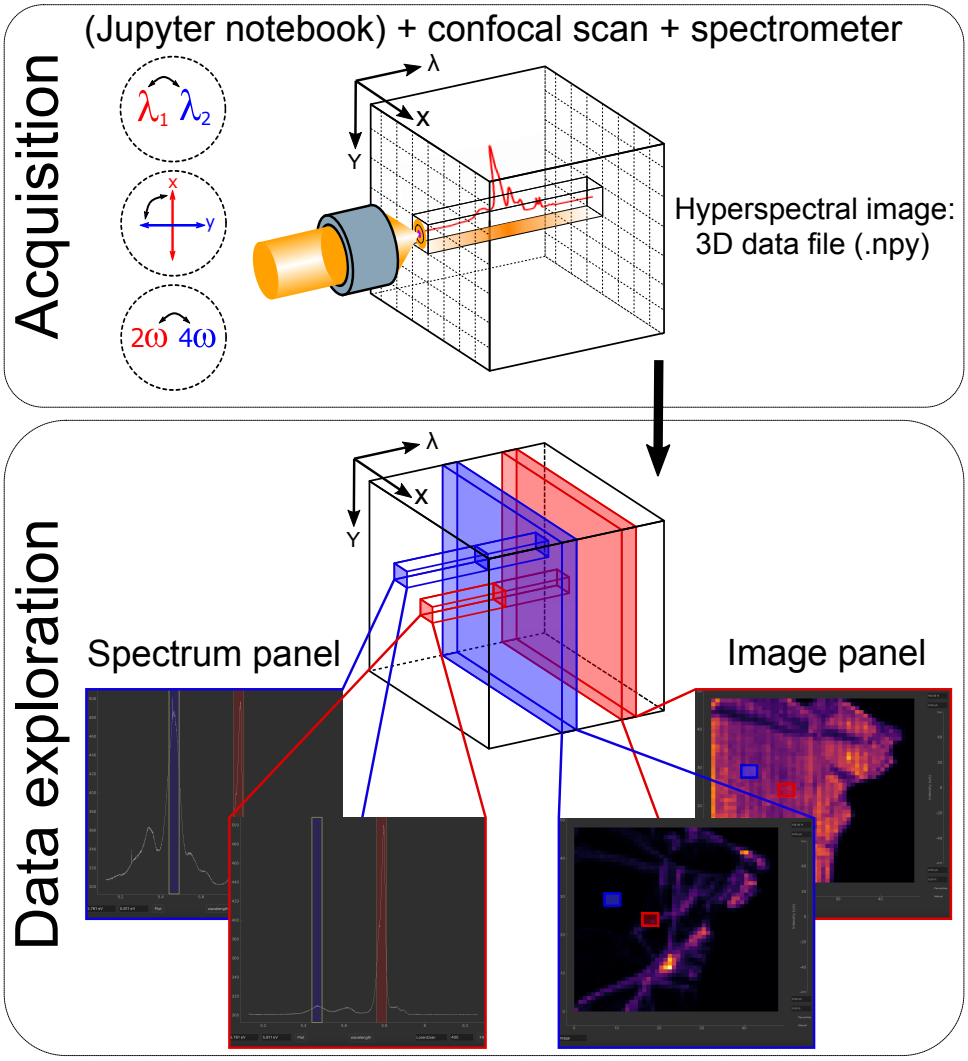

Figure 2.8: Diagram summarizing the hyperspectral data acquisition and exploration.

Finally, *GUI modules* handle the graphical user interface (GUI) like windows, buttons, or plots to interact with *logic modules* to manage the acquisition and visualize the acquired data. One interesting feature of Qudi is the ability to control the different instruments with Python scripts on *Jupyter Notebooks* allowing great flexibility in the control of the experiment. Because Qudi is an open-source Github project that has been developed and used by the community of spin defects commonly using confocal microscopy, we benefit from the modules already written for most of our instruments like for the scanners or the Thorlabs motorized rotations and flippers. On the other hand, spectrometer modules were missing which led me to develop a spectrometer tool chain for our spectrometer. This includes the interfacing of both the Czerny-Turner spectrometer and the CCD camera into *hardware modules*, a universal grating spectrometer *logic module* compatible with any type of grating spectrometer hardware, and a designed *GUI module* allowing advanced settings for different acquisition modes of the camera (image mode, counting

mode and spectrum mode). I also developed Qudi modules to control the Ti:Sa laser and the harmonics generator. This work took me more than 4 months of development resulting in more than 5000 lines of code and pull requests to the public Qudi project (https://github.com/Ulm-IQO/qudi/pull/648).

The second part of my work was to develop a Qudi module for the acquisition of hyperspectral images connecting the scanner with the spectrometer. To take advantage of the great flexibility offered by *Jupyter Notebooks* Qudi scripts, I developed a universal *lambda scan module* which enables modular and advanced acquisition at each point of a scan. The *lambda scan module* takes as input a custom function defined through a *Jupyter Notebooks* script which can perform all possible tasks from all the instruments of the setup and return a list of values at each position of the scan. For the hyperspectral acquisitions, we used custom functions that systematically measure the emitted spectrum on the spectrometer either for various grating orientations associated with different central wavelengths, various signal polarization, or various types of excitation (2ω and 4ω) as sketched on Fig.3.6. During the acquisition, the selected custom function is launched at each position of the scan and the returned values are stored as vectors for each position of the map forming a 3D tensor, namely a hyperspectral image.

Finally, because the analysis of such hyperspectral images can be complex, I developed a custom-made Python-written software, named *Hyperspex*, to explore our hyperspectral images, which allows us to see on one panel the image integrated over a given spectral range, and on another panel the spectrum integrated over a given selected area where both the spectral range and the selected area are dynamically controlled through the interface. The *GitHub* repository of the project can be found here: https://github.com/AdrienR09/hyperspex.

2.3 Conclusion

During this chapter, I gave a full description of the deep-UV microscope that I developed during my thesis. We then focused on the different technical challenges that the development of such a deep-UV microscope represents. This results in a deep-UV microscope with unique performances allowing a large flexibility in the experiments. In the following chapters, the performances of the microscope will be validated with practical cases leading to original results. In chapter 3, the deep-UV microscope will show its unique ability to probe atomically thin monolayer hBN allowing it to perform a deep investigation of the optical properties of monolayer hBN. In chapter 4, the high spatial resolution of the deep-UV microscope together with the ability to combine different optical techniques will allow me to identify microscopic domains of hBN polytypes and study for the first their optical properties.

Chapter 3

Monolayer hBN

This chapter is dedicated to the study of the optical properties of monolayer hBN. During my thesis, I used the deep-UV microscope described in Chapter 2 to perform systematic studies of the optical properties of exfoliated and epitaxial hBN monolayers. Our deep-UV microscope allowed me to study the intrinsic emission of monolayer hBN at the microscopic scale for the first time, unraveling the complex phenomenology of the coexistence of PL and Raman processes induced by the quasi-resonant excitation in monolayer hBN. Along this chapter, bulk hBN refer to the standard AA'-hBN polytype. The study of different hBN polytypes will be treated in the next chapter.

Contents

2.1 Context 31
2.1.1 Luminescence microscopy in the deep-UV 31
2.1.2 Physical processes 34
2.2 Deep-UV microscope 37
2.2.1 Deep-UV excitation 37
2.2.2 Sample cryogenic environment 39
2.2.3 Signal collection and detection 43
2.2.4 Software control and hyperspectral acquisition 44
2.3 Conclusion 46

3.1 Optical properties of monolayer hBN

Thinning a bulk lamellar material down to a single monolayer leads to dramatic effects associated to the reduction of dimensionality. One important phenomenon is the indirect-direct bandgap crossover where the indirect bandgap of a bulk semiconductor becomes direct at the monolayer limit. This effect has been observed in many 2D materials like transition metal dichalcogenides (TMDs) or black phosphorus (BP) [10]. Generally, the indirect-direct bandgap crossover induces a strong enhancement of the luminescence at the monolayer limit as depicted in Fig.3.1(a) where the intrinsic PL of MoS_2 increases by almost four (two) orders of magnitude when reduced to a monolayer compared to bulk (bilayer) [11]. In samples made of domains of different thicknesses, spatially-resolved luminescence microscopy enables a direct spatial identification of monolayers which appear much brighter than multi-layers as shown in Fig.3.1(b) where the widefield PL map of an exfoliated MoS_2 flake is dominated by the luminescence of the

monolayer [81]. Accordingly, spatially-resolved PL microscopy has become a standard approach to study the optical properties of 2D materials and, in particular, for exfoliated flakes with typical lateral size of 10-100 µm.

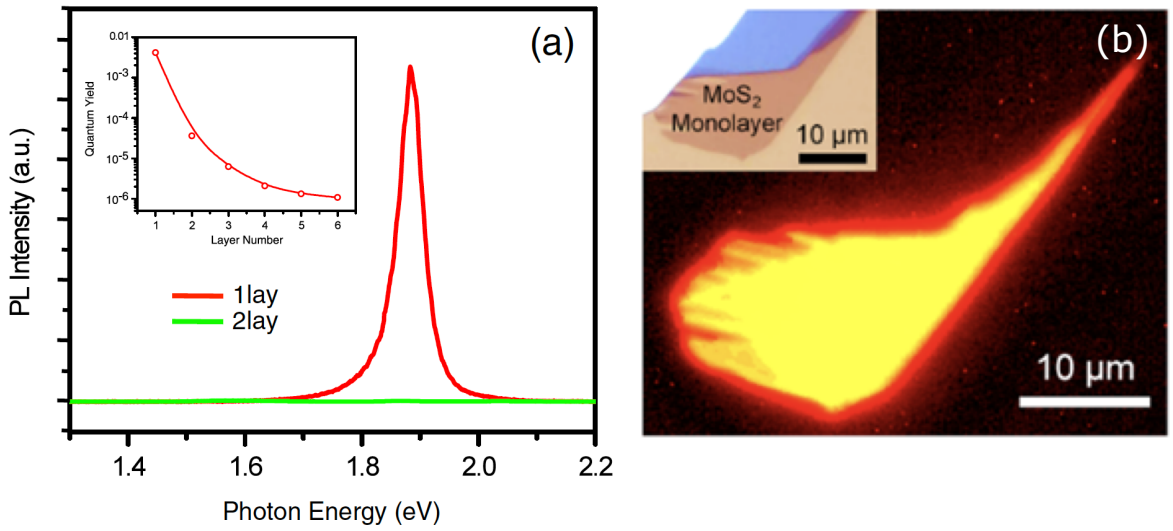

Figure 3.1: (a) PL spectrum of MoS_2 monolayer (in red) and bilayer (in green) [inset representing the PL intensity of MoS_2 versus the number of layers] [11]. (b) Widefield PL map of an exfoliated MoS_2 flake where the monolayer appears much brighter [picture of the flake in inset] [81].

Studying the optical properties of hBN using this standard approach requires spatially-resolved PL microscopy in the deep-UV due to the wide hBN bandgap. As already mentioned in Chapter 2, the development of an optical microscope in the deep-UV represents a real technical challenge so that such microscope was inexistent before 2019 thus precluding the use of the standard mirco-PL approach for hBN. Alternatively, spatially-resolved luminescence microscopy can be performed in a SEM by CL microscopy which is commonly used for wide bandgap materials. *Schué et al.* studied dimensionality effects on exfoliated hBN flakes down to 6 atomic layers. They were not able to detect any signal below 6 layers probably because of the low electron interaction cross-section as already discussed in Chapter 2 [76]. To study the indirect-direct bandgap crossover in hBN, *Elias et al.* used a different approach involving macroscopic measurements of both PL and reflectance spectra of monolayer hBN epitaxially grown by MBE on a highly ordered pyrolytic graphite (HOPG) substrate as shown on Fig.3.2 [13]. The typical PL spectrum of bulk hBN, represented in red on Fig.3.2(a), consists of a series of phonon replicas below 5.95 eV where the emission above ∼5.7 eV corresponds to the phonon-assisted emission of the indirect hBN bandgap while the lower energy emission bands correspond to the so-called stacking faults emission as discussed in Chapter 1. In contrast, the PL spectrum of monolayer hBN measured by *Elias et al.* shows two sharp peaks around ∼6.1 eV lying in the same range as the reflectance minimum, as shown in Fig.3.2(a). The absence of Stokes shift between the

reflectance minimum and the PL emission lines at ∼6.1 eV supports the demonstration of the direct bandgap of monolayer hBN. Similar results have been obtained by *Wang et al.* using the same approach on other MBE-grown monolayer hBN on HOPG [14]. More recently, *Shima et al.* succeeded in measuring the direct emission of epitaxial monolayer hBN by exciting the monolayer over a macroscopic area with an electron beam at a large incidence angle (∼60°) to increase the energy deposited onto the monolayer [57].

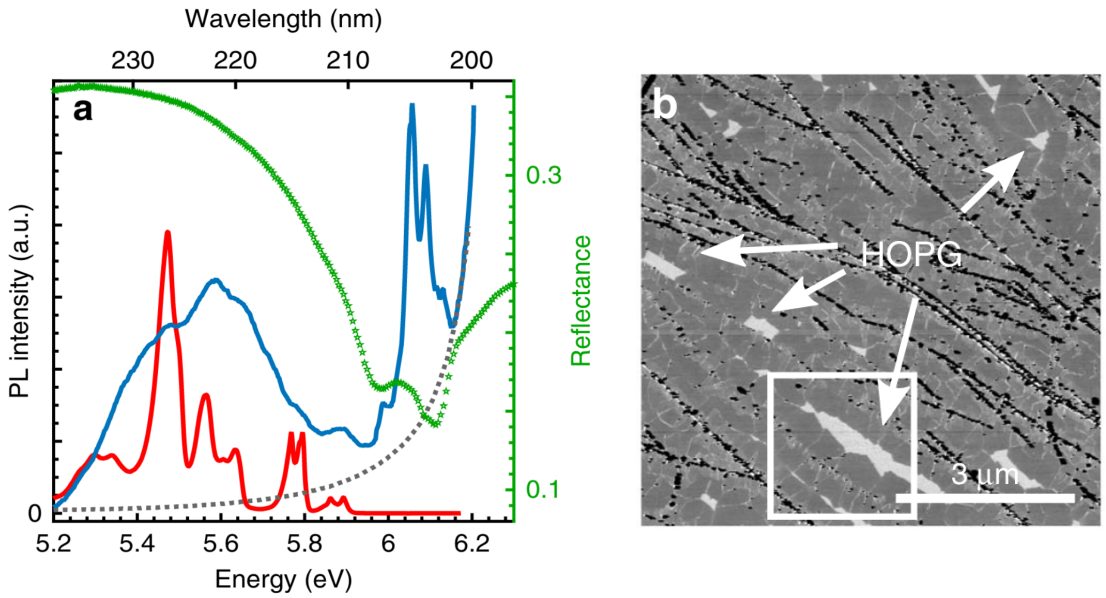

Figure 3.2: (a) Macro PL (in blue) and reflectance (in green) spectra of epitaxial monolayer hBN grown by MBE on HOPG. The typical PL spectrum of bulk hBN (in red) and the emission spectrum recorded on bare graphite without mBN (grey dotted line), showing stray light from the laser excitation, are plotted for comparison. (b) AFM topography of the epitaxial monolayer hBN [13].

As discussed in Section 1.1.4, the reduced screening of the Coulomb interaction in 2D materials leads to a huge exciton binding energy, of ∼2 eV in free-standing monolayer hBN [10,15,58]. Since the energy of the fundamental direct exciton (dX) of monolayer hBN has been estimated to ∼6.1 eV, the electronic bandgap is expected at ∼8 eV corresponding to a spectral window beyond the reach of any standard deep-UV laser [53]. To circumvent this critical issue, *Elias et al.* excited the PL of monolayer hBN using a quasi-resonant excitation via phonon-assisted processes where the excitation energy is detuned by one or few phonons [13]. Such quasi-resonant phonon-assisted excitation was demonstrated in other 2D materials like monolayer $MoSe_2$. Fig.3.3(a) shows the PL excitation (PLE) intensity map of monolayer $MoSe_2$ where the x-axis (y-axis) represents the emission (excitation) energy [82]. We observe three sharp diagonal lines shifting with the laser energy corresponding to the Raman scattering by the phonons A'(Γ), E'(Γ) and 2LA(M) of $MoSe_2$, respectively. The Raman scattering signal increases in the condition of resonant Raman scattering (RRS) at the vicinity of the X_0 resonance around ∼1.65 eV. Additionally, we observe a large signal around ∼1.65 eV corresponding to the PL emission of X_0

which increases when the Raman becomes resonant. This is due to the quasi-resonant excitation of the PL via the emission of the phonons also involved in the Raman scattering. Consequently, the quasi-resonant excitation leads to a coexistence of the PL and Raman optical emission making the analysis of the overall spectrum difficult. This PL/Raman coexistence was also present in the emission spectrum of monolayer hBN measured by *Elias et al.* due to the need for a quasi-resonant excitation because of its wide electronic bandgap precluding any excitation in the continuum of the free carriers states. *Elias et al.* used ∼150 fs laser pulses for the quasi-resonant excitation, inducing a spectral broadening of the Raman scattering making the analysis of the spectrum even more complex. The variation of the monolayer hBN signal around ∼6.1 eV for different excitation energies is shown in Fig.3.3(b). The spectral modulations observed for the different excitation energies indicate the coexistence of PL and Raman signals although the Raman signal cannot be as clearly identified as in Fig.3.3(a). Nonetheless, the signal reaches a maximum for a 6.4 eV excitation corresponding to a detuning of ∼312 meV which was attributed to the emission of the 2LA(M) overtone (LA(M)∼150 meV) [13].

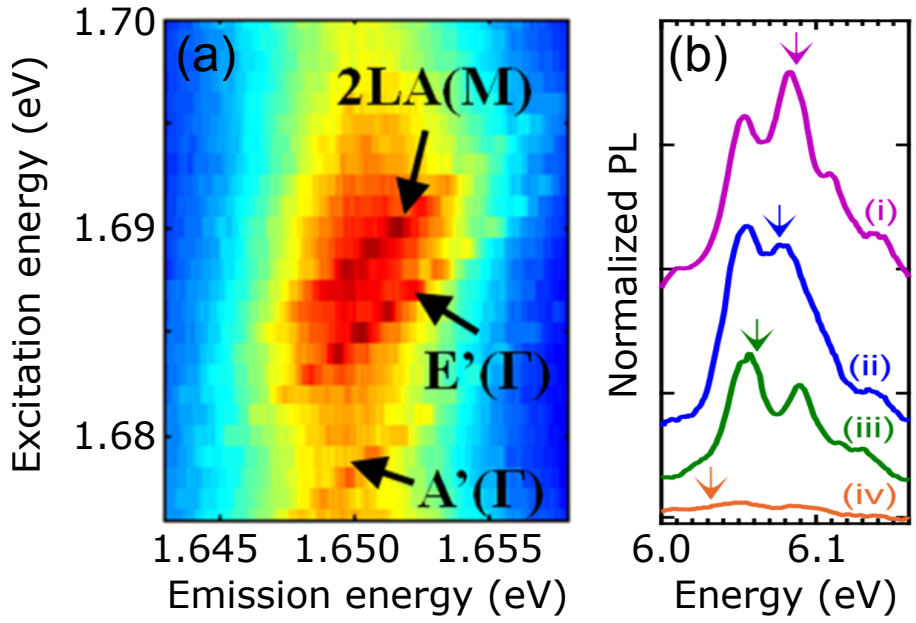

Figure 3.3: (a) PL excitation (PLE) intensity map of monolayer $MoSe_2$ [82]. (b) PL spectra of monolayer hBN for different excitation energies : (i) 6.4, (ii) 6.39, (iii) 6.375, and (iv) 6.345 eV [13].

For an excitation energy below 6.345 eV [spectrum (iv) on Fig.3.3(b)] the signal decreases drastically because of the detuning from the monolayer resonance which does not match anymore the 2LA(M) overtone detuning. In this non-resonant condition, we still observe a weak doublet at ∼6.04 eV and ∼6.08 eV independent of the Raman signal. This doublet has been tentatively attributed either to the emission of the two inequivalent direct excitons in K and K' valleys or to the phonon replicas from the phonon-assisted indirect emission of iX in monolayer

hBN [14, 56, 57]. This discussion comes together with the long-standing debate on the nature of the monolayer hBN bandgap where direct and indirect excitons are estimated at almost the same energies [52]. Recent *ab initio* simulations of the luminescence spectrum of monolayer hBN involving the contribution of phonons have suggested a very tiny contribution of iX to the luminescence spectrum [15].

A deeper understanding of the optical properties of monolayer hBN thus requires further investigation of the interplay between the PL and Raman processes under quasi-resonant excitation conditions. **To do so, it is meaningful to study how the relative contributions of these two processes vary both spatially and with the monolayer fabrication. This could help to answer the question about the physical origin of these processes and if they are intrinsic or extrinsic to monolayer hBN.**

In this chapter, I performed a systematic study on the optical properties of both exfoliated (Part 3.2) and epitaxial (Part 3.3) monolayer hBN. Thanks to the hyperspectral imaging in the deep-UV and the high spatial resolution of our deep-UV microscope (∼200 nm), I could study the correlations between the spatial and spectral variations of the signals for each sample. I could also investigate the complex interplay between PL and Raman processes around 6.1 eV induced by the quasi-resonant excitation of monolayer hBN. It led me to develop a phenomenological model that quantitatively describes these two processes as well as their relative intensity. Following a fitting procedure on each point of the maps, we could then retrieve the spatial variations of the different components of the optical signal. Then, by comparing the results obtained for the different types of samples, we gained insight into the origin of each process (Part 3.4) leading to a better understanding of the optical properties of monolayer hBN.

3.2 Exfoliated monolayer hBN

This part is dedicated to the study of the optical properties of an exfoliated hBN thin flake. In Section 3.2.1 we characterize the sample topography through a parallel analysis by wide-field microscopy in the visible, AFM topography, and PL imaging in the deep-UV. In Section 3.2.2, we perform a detailed analysis of the hyperspectral image measured on an area overlapping few-layer and monolayer hBN to resolve the spectral emission depending on the hBN thickness. In Section 3.2.3, we finally study the optical properties of few-layer hBN and their dependence on the thickness.

3.2.1 Sample topography

Our sample consists of an exfoliated hBN thin flake obtained by mechanical exfoliation with the standard scotch tape technique from a bulk hBN crystal grown by the high-pressure high temperature (HPHT) method, transferred onto a silicon wafer covered by 85 nm silicon oxide. Because hBN is transparent in the visible range, the optical contrast of thin hBN flakes is

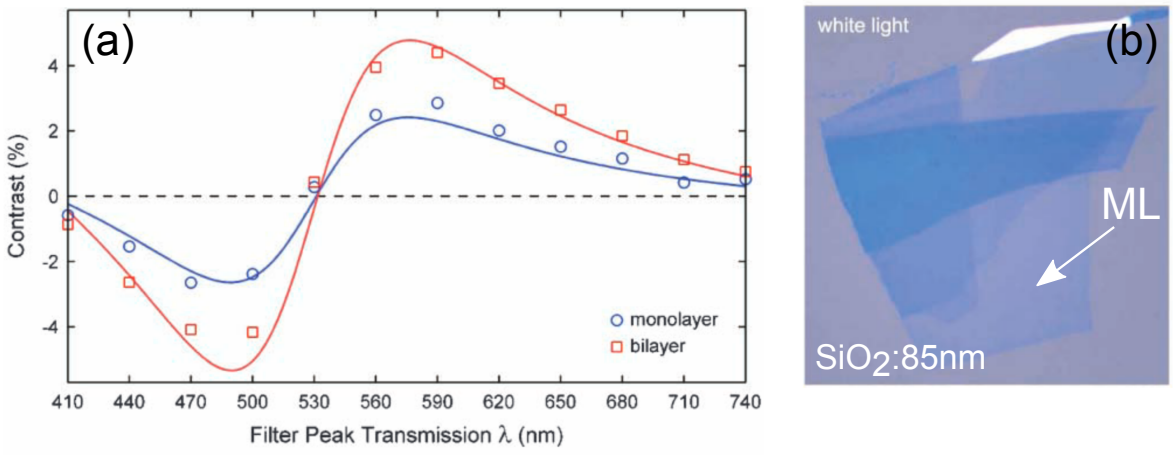

Figure 3.4: (a) Variation of the optical contrast with the optical wavelength calculated using the TMM method for monolayer (blue curve) and bilayer (red curve) hBN. The corresponding experimental values measured on thin exfoliated hBN flakes using different filters are represented by the blue circles (red squares) for the monolayer (bilayer). (b) Microscope picture under white light illumination of the thin exfoliated hBN flake used for the measurement of the optical contrast in (a) [44].

small making their identification very difficult. Nonetheless, the optical contrast can be further improved through Fabry-Perot interferences in the visible domain, induced by the thin oxide layer underneath, which vary with the thickness of the hBN flakes on top resulting in different light reflections. The optical contrast is defined as the reflectivity difference between the hBN flake and the substrate ($C = \frac{I_{hBN}-I_0}{I_{hBN}+I_0}$), it can then be optimized for monolayer hBN by tuning the oxide layer thickness. *Gorbachev et al.* used the transfer matrix method (TMM) to calculate the optical contrast resulting from the Fabry-Perot interferences of the multilayer structure (silicon wafer/oxide layer/hBN flake) varying both the oxide, the hBN thickness and the wavelength [44]. They found an optimal contrast, under white light illumination, of ∼2 % (∼5 %) for the monolayer (bilayer) with 85 nm silicon oxide [Fig.3.4(a)] which they confirmed experimentally as shown by the markers on Fig.3.4(a).

Fig.3.5(a) shows an optical image of our hBN sample under white light illumination obtained from a standard wide-field optical microscope. On the image, we can identify three main regions with distinct optical contrast corresponding to three different hBN layer thicknesses. The top region (green rectangle) shows the highest optical contrast of ∼30 % corresponding to a hBN thickness greater than ∼50 nm, from TMM calculations, equivalent to bulk hBN. The central region (red triangular shape) exhibits a weaker contrast of ∼7 % associated with hBN thicknesses of 4-∼10 nm corresponding to few-layer hBN (FL) except for the blue diagonal line [Fig.3.5(a)] crossing in the middle with a higher optical contrast (∼11 %) which can be attributed to layers folding or stacking faults. The last narrow area highlighted in white on Fig.3.5 presents an optical contrast of ∼2 % in accordance with what is expected for monolayer hBN (ML) onto

85 nm silicon oxyde [44].

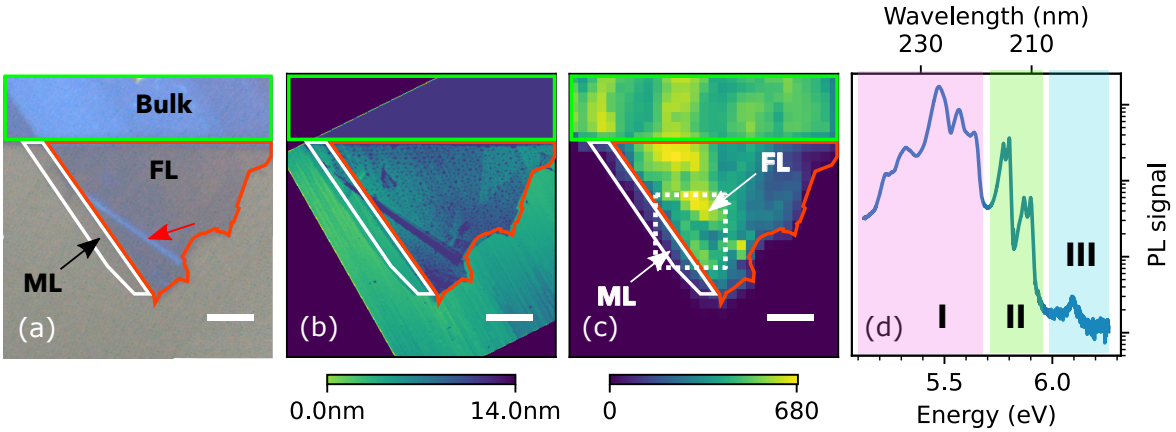

Figure 3.5: (a) Widefield microscope image under white light illumination of the exfoliated hBN flake showing three distinct regions, the monolayer (ML - white), few-layer (FL - red), and bulk (green) region, with optical contrasts of ∼30, ∼7 and ∼2 %, respectively. The red arrow indicates the folded area. (b) AFM topography image of the hBN flake with the colorbar representing the sample height relative to the substrate. (c) PL intensity image integrated over 5.71-5.95 eV corresponding to the green shaded area II on panel (d). (d) deep-UV PL spectrum spatially integrated over the area represented by the white dashed square on panel (c), the different pink (I), green (II), and blue (III) shaded areas represent the detection windows associated to defects, few-layer, and monolayer emission. Scale bars = 4 µm.

Fig.3.5(b) displays the sample topography image measured using atomic force microscopy (AFM). The height with respect to the substrate is plotted in color with the code indicated below Fig.3.5(b), going from 0 to 14 nm in order to preferentially observe the thickness variations in the ML and FL regions. We then observe a good correspondence between the AFM heights and the optical contrast in the visible domain [Fig. 3.5(a)] of the hBN flake. The height of the bulk region is larger than 14 nm while the height of the FL region varies from 2 to 5 nm except for the folded region where the height is greater than 14 nm. The topography image also shows small bubbles over the FL region, commonly observed in exfoliated flakes, and coming from air bubbles trapped during the transfer process. The height measured on the ML region around ∼2 nm is six times larger than the interlayer distance of bulk hBN (c_0 ∼0.33 nm), presumably because of a contaminant layer trapped beneath the flake [44]. The AFM topography of a folded monolayer gives the expected height difference of 0.33 nm between the monolayer and the folded area whereas the height of the monolayer from the substrate was again ∼2 nm. Accordingly, the estimated number of atomic layers in the FL region, except for the folded region, ranges between 7 to 15 atomic layers.

We then recorded the PL in the deep-UV at ∼5 K using our deep-UV microscope with an excitation energy of 6.39 eV (194 nm) in the same area of the hBN flake as Fig.3.5(a,b). Fig.3.5(d) shows the PL spectrum in the deep-UV averaged over the area represented by the

white dashed square on Fig.3.5(c) overlapping both the FL region with the folded region and the ML region. The PL spectrum of the hBN flake can be separated into three parts represented by the three shaded regions in Fig.3.5(d). The PL signal below 5.7 eV (pink region - I) arises from the recombination of excitons localized on extended defects such as stacking faults (see Section 1.2.4) [75]. The PL signal in the range 5.71-5.95 eV (green region - II) corresponds to the phonon replicas from the indirect bandgap emission of bulk hBN (see Section 1.2.4). Finally, above 5.97 eV (blue region - III) we observe a dim signal centered around ∼6.1 eV matching the energy of the PL emission attributed to monolayer hBN by *Elias et al.*. Fig.3.5(c) shows the PL intensity map integrated over the detection window represented by the green region on Fig.3.5(d) corresponding to the indirect bandgap emission of hBN. In both the bulk and the FL region, the average intensity is around ∼500 counts with 15 % spatial variations except along the folded region or at the top right of the FL region where the signal decreases by more than 50 % (∼200 counts). The similar PL intensity despite the different hBN thickness in these two regions originates from the strong absorption of hBN at 194 nm resulting in a penetration depth of 2-3 nm for the excitation. The spatial variations of the PL intensity are attributed to the excitons trapped by shallow defects, like stacking faults, thus reducing the number of free excitons initially generated. In the ML region, the PL intensity decreases rapidly to ∼5 counts.

3.2.2 Hyperspectral imaging in the deep-UV

We used hyperspectral imaging in the deep-UV to study the spatial distribution of each spectral component in the PL spectrum of Fig.3.5(d). We performed a PL map over an area delimitated by the white square of Fig.3.5(c), with a spatial resolution of ∼300 nm, under the same conditions as Fig.3.5(c). Fig.3.6 represents the recorded hyperspectral image in the deep-UV where the three first panels show the PL intensity integrated below 5.76 eV, over 5.76-5.93 eV and above 5.93 eV, respectively, represented by the shaded areas of different colors on Fig.3.5(d). Panel (d) shows the PL spectra taken on the three distinct points marked on panels (a-c).

In panel (a) showing the PL below 5.76 eV, the PL intensity is localized in a ∼1 µm strip delimitated by white dotted lines, along the image diagonal. This region matches the folded part of the FL region observed on the sample topography. The PL spectrum (I) measured inside the strip [Fig.3.6(d)] is dominated by the SF emission below 5.7 eV thus showing the impact of folding, leading to the formation of stacking faults, on the recombination processes.

In panel (b) showing the energy window 5.76-5.93 eV, the PL intensity is roughly constant over the FL area except for the strip discussed above where the PL signal is lower in this spectral range. The PL spectrum (II) is dominated by the intrinsic phonon-assisted emission [Fig.3.6(d)]. The drop of the intrinsic emission in the folded area is explained by the trapping of free excitons by the extended defects. The resulting spatial anti-correlation between intrinsic and defect-assisted PL is similar to previous reports by CL [75]. In a defect-free area, the PL intensity is rather uniform over a typical length of ∼10 µm which is a good indication of the intrinsic nature of the emission where the free excitons can recombine everywhere equivalently without being

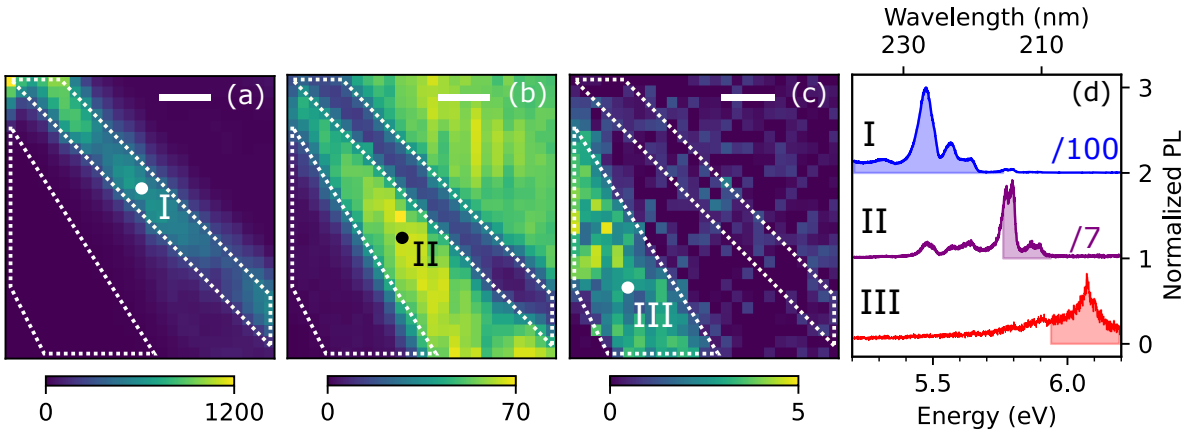

Figure 3.6: (a, b, c) PL intensity images integrated below 5.76 eV, over 5.76-5.93 eV and above 5.93 eV, respectively, represented by the shaded areas of different colors on Fig.3.5(d). (d) Deep-UV PL spectra taken on the three different points I, II and III represented on panels (a, b, c), respectively. Scale bars = 1.6 µm.

trapped. Moreover, the PL intensity at stacking faults is almost ∼15 times stronger than the intrinsic emission [Fig.3.6(d)] in agreement with what is typically observed in bulk hBN [74]. This can be explained by the presence of a density of final electronic states from extended defects below the hBN bandgap inducing an increase of the inter-K valley scattering efficiency through a strong enhancement of the phonon-assisted relaxation rate. As a matter of fact, at the spatial position of the stacking faults, inter-K valley scattering corresponds to an efficient nonradiative relaxation channel for the intrinsic phonon-assisted emission, which quenches the PL signal at 5.76-5.93 eV and seeds the one below 5.76 eV, finally leading to a spatial anti-correlation between the two maps of panels (a) and (b).

In panel (c) showing the PL above 5.93 eV, the PL intensity is localized inside a ∼3 µm width area represented by white dotted lines delimitating the region identified as a monolayer by optical reflectivity [Fig.3.5(a)] and AFM [Fig.3.5(b)]. In this area, the PL intensity varies from 2 to 5 counts with the position. However, we did not observe any spectral modulation of the PL with the position. Because the recorded signal lies near our detection threshold, we could not conclude on the origin of these spatial variations. The PL spectrum (III) measured inside this zone presents only emission around 6.1 eV which corresponds to the intrinsic emission of monolayer hBN as measured by *Elias et al.* [13]. The PL intensity of the monolayer is thus ∼100 (∼7) times weaker than for the stacking faults (intrinsic) emission. The reasons for that are, first, the atomic thickness of monolayer hBN inducing a very small excitation volume and, second, the quasi-resonant excitation characterized by the absence of a density of states (DOS) at the excitation energy where the monolayer is only excited through phonon-assisted processes which are much less efficient than the direct absorption. Consequently, the phenomenology of the indirect-direct bandgap crossover typically observed in other 2D materials is drastically different in hBN where the indirect bandgap emission of few-layer or bulk hBN is one order of

magnitude stronger than the emission of the monolayer direct exciton. Indeed, this is partly due to the need for a quasi-resonant excitation imposed by the very large bandgap of monolayer hBN.

We observe a clear anti-correlation between the three intensity maps of panels (a-c) while the three spectral features (I-III) on Fig.3.5(d) are spectrally distinct from each other thus indicating their different origin. Therefore, despite the weaker emission of monolayer hBN compared to the few-layer and bulk hBN making a direct spatial identification of the monolayer as in TMDs, the hyperspectral imaging allows to isolate both spatially and spectrally the optical signature of monolayer hBN. We thus recorded for the first time the intrinsic emission of an exfoliated hBN monolayer which will be analyzed in detail and compared with epitaxial monolayers in Section 3.4.

3.2.3 Indirect bandgap emission in few-layer hBN

Here we want to study the indirect bandgap emission of few-layer hBN. Fig.3.7(b) shows three PL spectra recorded at different positions on the FL area. They differ from the typical PL spectrum of bulk hBN shown in Fig.1.14. As for bulk hBN, we observe an intense doublet at ∼5.76 eV and a weaker doublet at ∼5.86 eV which correspond to the phonon-assisted emission of the indirect bandgap involving LO_3/TO_3 and LA/TA phonons at the T point, respectively, as explained in Section 1.1.4. However, the 6 meV overtones on the low energy side of the phonon replicas typically observed in bulk hBN are not resolved and the shape of the phonon replicas is different from bulk hBN [73]. This could be attributed to the inhomogeneous broadening of the phonon replicas and overtones induced by spatial disorder inside the layer. One origin of this disorder could be strain fluctuations which are more likely in very thin films like few-layer hBN, as suggested by the presence of bubbles in the FL area observed by AFM [Fig.3.5(b)].

Alternatively, this broadening could originate from the reduced thickness of the FL area (2-4 nm) which is on the same order as $|\vec{c}|$ (∼6.6 Å) thus inducing dimensionality effects. As a result of the *Born-von Karman* conditions, the reciprocal space along k_z is discretized with respect to the crystal thickness L_z as $\Delta k_z = \frac{2\pi}{L_z}$. In the FL area, Δk_z correspond to ∼1.5-3 nm^{-1}) that is of the same order than $|\vec{c}^*|$ (∼5 nm^{-1}) resulting in the alteration of the selection rules along k_z. Thus, any phonons along k_z can be involved in the phonon-assisted processes thus leading to a spectral broadening of the transitions with respect to the out-of-plane dispersion at T. However, the phonon dispersion along k_z around T calculated by our collaborator *Giorgia Fugallo* is of the order of ∼1 meV for in-plane phonons, one order of magnitude smaller than the broadening of the phonon replicas [Fig.3.7(b)] of about 10-20 meV. This effect of dimensionality has been also suggested by *Schué et al.* when studying exfoliated few-layer hBN using CL spectroscopy [76]. At this stage, we could not give any clear explanation about the origin of this line broadening that is commonly observed in few-layer hBN.

We further observe a modification of the doublet intensity ratio with the thickness as shown

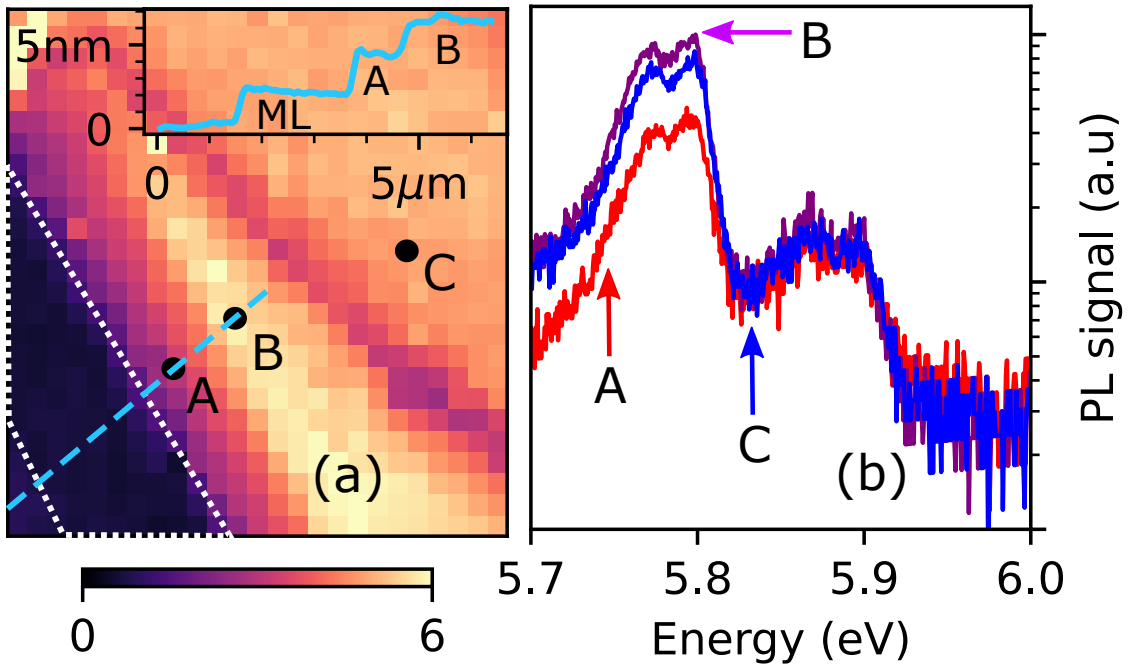

Figure 3.7: (a) Map of the intensity ratio between the PL signal integrated over 5.73-5.83 eV and 5.83-5.93 eV, with the ML area represented by the white dashed lines [inset representing the AFM linecut along the blue dashed line represented on the map]. (b) PL spectra taken on three different points A, B and C represented on panel (a).

in Fig.3.7(a) which represents the map of the intensity ratio (I_r) between the two doublets following the equation :

$$I_r = \frac{I_{LO_3/TO_3} + c}{I_{LA/TA} + c} - 1 \tag{3.1}$$

where I_{LO_3/TO_3} corresponds to the intensity of the LO_3/TO_3 doublet integrated over 5.73-5.83 eV while $I_{LA/TA}$ corresponds to the intensity of the LA/TA doublet integrated over 5.83-5.93 eV. Offsets c have been added to I_{LO_3/TO_3} and $I_{LA/TA}$, respectively, so that I_r cancels out when both I_{LO_3/TO_3} and $I_{LA/TA}$ much smaller than c. I used the value c =1 counts s^{-1}, corresponding to the noise limit in our measurements. The variations of I_r, going from 0 to 6, are plotted in color following the code indicated below Fig.3.7(a). The ML area is delimitated by the white dashed lines and it appears dark on the bottom left of Fig.3.7(a) where both I_{LO_3/TO_3} and $I_{LA/TA}$ fall below c resulting to $I_r \sim 0$. On the FL area, I_r varies from 1 to 6 with a terrace-like spatial distribution. An AFM topography line-cut along a path going from the substrate through the ML region to the FL region stopping before the folded area (blue dashed line on Fig.3.7(a)) is represented in the inset of Fig.3.7(a). The line-cut shows three terraces, labeled (ML), (A) and (B), all with a step height of ∼2 nm. The first terrace (ML) corresponds to the monolayer characterized by a ∼2 nm offset, as explained in Section 3.2.1, while terraces A and B correspond to few-layer hBN with different thicknesses in the FL region. By applying the ∼2 nm offset correction, we find an upper bound of ∼7 and ∼15 atomic layers for the terraces A and B, respectively. The height of

terrace C at the top right of Fig.3.7(a) across the folded area is equivalent to the one of terrace B.

We find a good correspondence between I_r and the AFM topography where I_r is uniform over the different terraces, and equal to ~ 3, ~ 6 and ~ 5.5 on terraces A, B and C, respectively. The 5.5 intensity ratio on terrace C is comparable to what has been measured on the bulk region and what is typically observed in the literature for bulk hBN [6–8]. The small change (~ 0.5) of I_r between terraces B and C may come from the different number of atomic layers. Interestingly, the two-fold decrease from B to A is consistent with the two-fold decrease of the thickness, thus suggesting a linear relation between I_r and the hBN thickness in the few-layer regime. Finally, I_r decreases to ~ 4 along the diagonal corresponding to the folded layers. This could be attributed to the effect of strain induced by the folding then modifying the selection rules of the phonon-assisted processes.

Our results on the indirect bandgap emission of few-layer hBN are radically different from those of *Schué et al.* which observed dramatic changes of the intrinsic emission with the thickness from 27 to 6 atomic layers where the LA/TA doublet is replaced by a singlet at ∼5.9 eV as shown on Fig.3.8 [76]. The indirect bandgap emission that we measured on few-layer hBN, with atomic thickness going from 7 to 15 atomic layers, retains the main characteristics of bulk hBN. However, the phonon replicas in few-layer hBN are broader than in bulk hBN and the intensity of the LA/TA doublet varies with the hBN thickness. The spectral shift or the emergence of a singlet reported by *Schué et al.* could be imputed to the effect of strain present in their studied hBN layers. This argument is strengthened by the observation of similar deformations on bent hBN layers by *Schué et al.* [83]. This also suggests that the indirect bandgap emission of few-layer hBN is sensitive to local strain which can be induced by the underlying topography. Up-to-date, the influence of strain on the opto-electronic properties of hBN in the deep-UV remains unexplored, and an in-depth investigation is required to understand the properties of thin hBN layers.

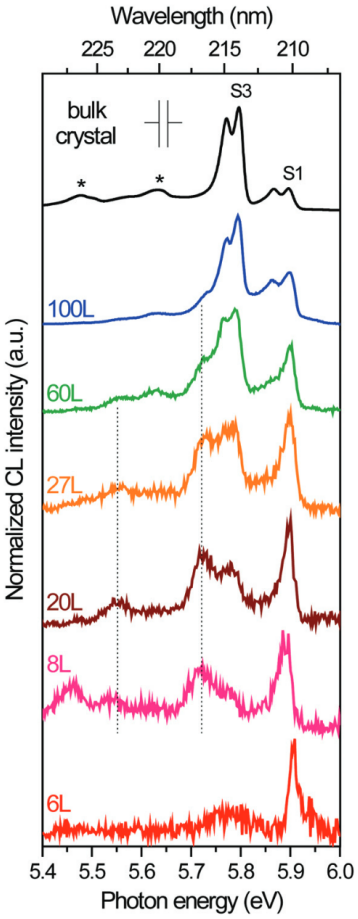

Figure 3.8: CL spectra of bulk hBN and flakes of 100, 60, 27, 20, 8 and 6 layers measured by *Schué et al.* [76].

3.3 Epitaxial monolayer hBN

In the previous part, we studied the optical properties of exfoliated monolayer hBN. In order to investigate the optical properties of monolayer hBN for different fabrication techniques, this part is dedicated to the study of epitaxial monolayer hBN. In particular, I focus on two epitaxial samples differing by their monolayer hBN coverage. In Section 3.3.1 I identify the different components of the AFM topography of the two samples. In Section 3.3.2, I use the deep-UV microscope to record hyperspectral images on the two samples using two different excitation energies to explore the variations of the different spectral components in space and with the excitation energy.

3.3.1 Samples topography

The samples consist of hBN monolayers epitaxially grown by MBE on HOPG substrates in the group of *Pr. Sergeï Novikov* from Nottingham University, similar to the one studied by *Elias et al.* [13]. HOPG has been shown to be an ideal substrate for the epitaxial growth of high-quality monolayer hBN via MBE due to the small lattice mismatch between hBN and graphene layers and their similar thermal expansion [84, 85]. The hBN layers grown on HOPG do not show any crack or wrinkle induced by the strain as generally observed in other substrates like sapphire (Sa). The HOPG substrate is however usually a polycrystal made of many microscopic graphite single-crystal domains with various orientations forming atomic steps on the HOPG surface. The lateral size of the graphite domains varies from 1 to 100 µm.

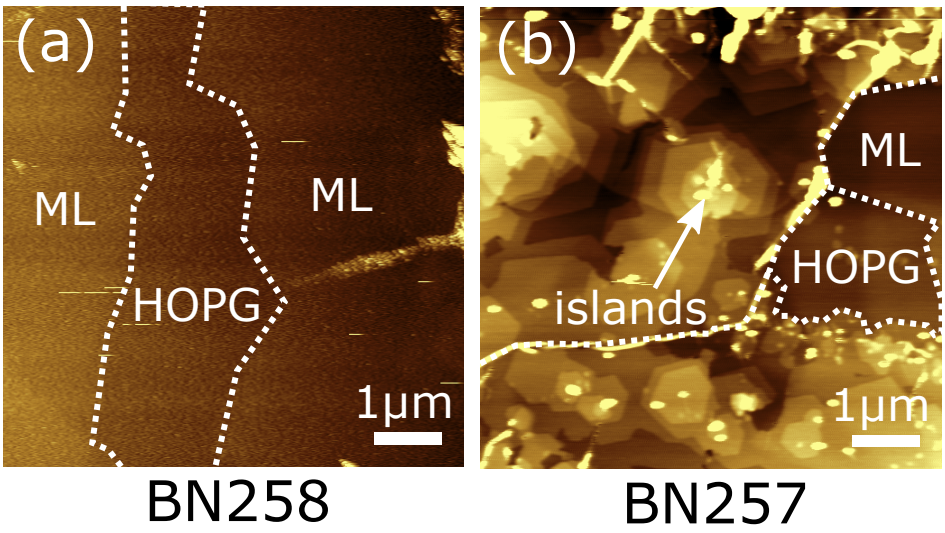

Figure 3.9: AFM topography images of BN258 (a) and BN257 (b) where the HOPG regions are delimitated by the white dashed lines and the arrows indicate the bulklike islands on BN257.

During the growth, the HOPG substrate is placed inside the MBE reactor and heated up to ∼1800 °C. An active flux of N atoms is produced by a radio-frequency (RF) plasma source

(Veeco) operating at 550 W with a N flow rate of 2 sccm. Besides, the B flux is produced by a high-temperature solid-source effusion cell. The two samples labeled BN257 and BN258 have been grown under similar conditions for different boron cell temperatures (T_B) of 1950 °C and 1925 °C, respectively. Fig.3.9 shows the AFM topography image of BN257 and BN258 where the color scale represents the height of the epitaxial layer relative to the substrate going from 0 (dark) to 2 nm (yellow). The AFM topography is drastically different in the two samples. In particular, the two samples differ by their hBN coverage. A quantitative description of our samples can be made through the statistical analysis of their AFM topography. The average hBN thickness ($< e >$) is defined as :

$$< e >= \int\int e(\vec{r}) d^2\vec{r} \tag{3.2}$$

where $e(\vec{r})$ represents the local hBN thickness at a position $\vec{r}$. Since the hBN thickness is proportional to the number of hBN layers, the average hBN thickness can be expressed as a sum of the number of hBN layers :

$$< e >= \sum_{i=0}^{\infty} e_i \alpha_i \tag{3.3}$$

where $e_i = ic_0$ is the thickness of i hBN layers and α_i is the surface proportion covered by i hBN layers such that $\sum_{i=0}^{\infty} \alpha_i = 1$. Then, α_0 represents the fraction of uncovered HOPG areas ($\alpha_{HOPG} = \alpha_0$) and α_1 the fraction of monolayer hBN coverage ($\alpha_{ML} = \alpha_1$). Finally, the overall hBN coverage (α_{hBN}) is given by:

$$\alpha_{hBN} = \sum_{i=1}^{\infty} \alpha_i = 1 - \alpha_0 \tag{3.4}$$

The values of α_{ML} and α_{hBN} have been extracted from a statistical analysis of the AFM topography for the two samples, summarized in Tab.3.1. BN258 is characterized by α_{hBN} ∼α_{ML} ∼75 % meaning that BN258 mainly consists of monolayer hBN. The average thickness measured via X-ray photoelectron spectroscopy (XPS) by the group of *Pr. Sergeï Novikov* is ∼0.4 nm very close to the monolayer hBN thickness (0.33 nm). The AFM topography of BN258 [Fig.3.9(a)] is rather homogeneous and consists of ∼25 % of uncovered HOPG area, delimited by the white broken lines on Fig.3.9(a), and ∼75 % of monolayer hBN (ML). Both HOPG and ML areas have a typical lateral size of 2-10 µm and appear aligned with the vertical direction in the AFM image. Recently, *Summerfield et al.* demonstrated that monolayer hBN grows laterally from HOPG edges, later confirmed by *Wang et al.* [14,85]. Because of the atomic flatness of graphene layers, the kinetic energy of the incident B and N atoms makes the atoms diffuse over the surface of graphite domains. When the atoms reach the domain edges, generally associated to atomic steps, the B and N atoms are trapped by the domain walls and interact to form hBN. The other B and N atoms will then be locked by the monolayer hBN edges thus contributing to the lateral growth of monolayer hBN from HOPG edges.

BN257 presents a hBN coverage α_{hBN} ∼90 % and, therefore, only α_0 ∼10 % of uncovered areas [HOPG area Fig.3.9(b)]. Monolayer hBN covers only α_{ML} ∼∼30 % of the hBN film [ML

	T_B	α_{ML}	α_{hBN}	α_{ML}/α_{hBN}	$< e >$
BN257	1950 °C	∼30 %	90 %	∼30 %	∼1.7 nm
BN258	1925 °C	75 %	75 %	100 %	∼0.43 nm

Table 3.1: Summary of the main topography characteristics of BN257 and BN258.

area on Fig.3.9(b)] and the average thickness measured by XPS is ∼1.7 nm. This indicates the formation of thicker layers. The AFM topography of BN257 [Fig.3.9(b)] is strongly inhomogeneous. Both HOPG and ML areas present a typical lateral size in the micrometer range. In the topography image, we can observe many bright spots [white arrow on Fig.3.9(b)] on top of nested hexagons with increasing heights. Interestingly, they are found in higher density near the HOPG domain edges represented by the white broken lines in Fig.3.9(b). Because the two samples only differ by T_B which controls the B flow, we attribute the different topography of BN257 and BN258 to the higher B flow in BN257 which modifies the growth process of monolayer hBN as described earlier. The higher B flow presumably leads to a higher concentration of B atoms on the surface of the HOPG which are more likely to collide and interact around small nucleation centers in the middle of domains. The growth process should be drastically different from HOPG edges. The growth around nucleation centers has been already studied for other materials like GaS and GaSe grown via MBE and it generally consists of spiral growth, in the form of screw dislocations. In the case of the hBN pyramids, one can assume that the first hBN layer grows laterally around the nucleation center until a second hBN layer starts to grow from the center when the bottom layer becomes large enough, and so on. Moreover, bulklike hBN islands could be easily formed in the vicinity of the nucleation centers. This results in the formation of hBN pyramids with bulklike hBN islands on top. Consequently, a small variation of ∼1 %(25 °C) of T_B leads to dramatic changes in the topography of hBN epilayers which stems from a variation of the B flow. Because of their very different hBN topography, a systematic study of the optical properties of these two samples using our deep-UV microscope could provide a better understanding of the physical processes involved in the PL of monolayer hBN around 6.1 eV.

3.3.2 Hyperspectral imaging in the deep-UV

With our deep-UV microscope, we recorded two hyperspectral images on BN257 and BN258 using an excitation energy of 6.38 eV(194.2 nm) and 6.32 eV(196 nm), respectively. Fig.3.10 and Fig.3.12 represent the hyperspectral images obtained for BN258 and BN257. On both figures, panels (a) and (b) show the intensity maps integrated over 5.3-5.7 eV and 6-6.1 eV, respectively, represented by the orange and red shaded regions on panel (c) and also schematically shown below panels (a) and (b). Panels (c) show the PL spectrum spatially integrated on three different regions of the scans represented by the white rectangles labeled (I), (II) and (III) on panels (a) and (b). Finally, panels (d) show a zoom of the normalized spectra (I) and (II) in the range 5.9-6.2 eV. In the following, the signal intensity associated to extended defects (5.3-5.7 eV) and the intrinsic signal (6-6.1 eV) are represented by I_{def} and I_{ML}, respectively. Furthermore, the

spatial correlation (C) of I_{def} and I_{ML} is measured using :

$$C(X,Y) = \frac{\sigma_{XY}}{\sigma_X \sigma_Y} \tag{3.5}$$

with σ_{XY} and $\sigma_{X,Y}$ the spatial covariance and the standard deviations of X and Y where $X = I_{ML}$ and $Y = I_{def}$ in this case.

BN258

Starting with Fig.3.10 for BN258, I_{def} [panel (a)] varies from 0 to 150 counts/s at the surface of the sample where the signal is spatially distributed along diagonal lines which may correspond to HOPG edges. The areas showing the lowest signal intensity (I_{def} <4 counts/s) are represented by the black pixels on panel (a). The absence of emission from extended defects in these areas could either originate from defect-free hBN layers or from uncovered HOPG areas. Moreover, we also observe bright spots [yellow pixels on panel (a)] where the emission from extended defects shows the highest intensity (I_{def} >120 counts/s). These bright spots could be attributed to a high concentration of extended defects. I_{ML} [panel (b)] varies from 0 to 10 counts/s at the surface of the sample and the signal presents a similar spatial distribution as on panel (a). Remarkably, the one order of magnitude decrease between I_{ML} and I_{def} is similar to the intensity ratio between the stacking faults emission and the indirect bandgap emission typically observed in both few-layer [Fig.3.5] and bulk hBN [7]. The areas with the lowest signal intensity (I_{ML} <2 counts/s), represented by the black pixels on panel (b), nearly overlap with the black areas on panel (a). Therefore, these areas present a negligible signal over the full deep-UV range ($I_{def} + I_{ML}$ <6 counts/s) which indicates the absence of hBN. Moreover, these areas where $I_{def} + I_{ML}$ <6 counts/s represent a portion of 33 % of the overall map in agreement with α_0∼30 % measured on the AFM topography of BN258 [Fig.3.9(b)]. Moreover, the largest black area in panels (a) and (b) present a lateral size of the order of ∼2 µm in line with the HOPG area of the AFM topography in Fig.3.9(b). We then conclude that these areas correspond to uncovered HOPG areas. Interestingly, I_{def} and I_{ML} present a spatial correlation of C ∼21 %. This could be explained by the fact that $\alpha_{ML} \sim \alpha_{hBN}$ in BN258 meaning that most extended defects are surrounded by hBN monolayers which may jointly contribute to the signal measured over the spot area.

We now focus on the three selected areas represented by the white rectangles (I), (II) and (III) on panels (a,b). The raw intensity spectrum integrated over (I) is plotted on panels (c) and (d) [spectrum I in Fig.3.10(c,d)]. It shows a sharp lorentzian peak centered around ∼6.04 eV with a linewidth of ∼13 meV and a smaller peak at ∼6 eV. The spectrum below 5.9 eV is almost flat thus indicating the absence of defect-related emission. The raw intensity spectrum integrated over (II) is plotted on panels (c) and (d) [spectrum II in Fig.3.10(c,d)]. It shows a multiplet above 5.9 eV which consists of 7 peaks at 5.94 eV, 5.97 eV, 6 eV, 6.04 eV, 6.08 eV, 6.14 eV and 6.16 eV. Moreover, below 5.9 eV we observe 3 broad emission bands around 5.46 eV, 5.6 eV and 5.79 eV with a linewidth ranging from ∼50 meV to ∼300 meV which we attribute to

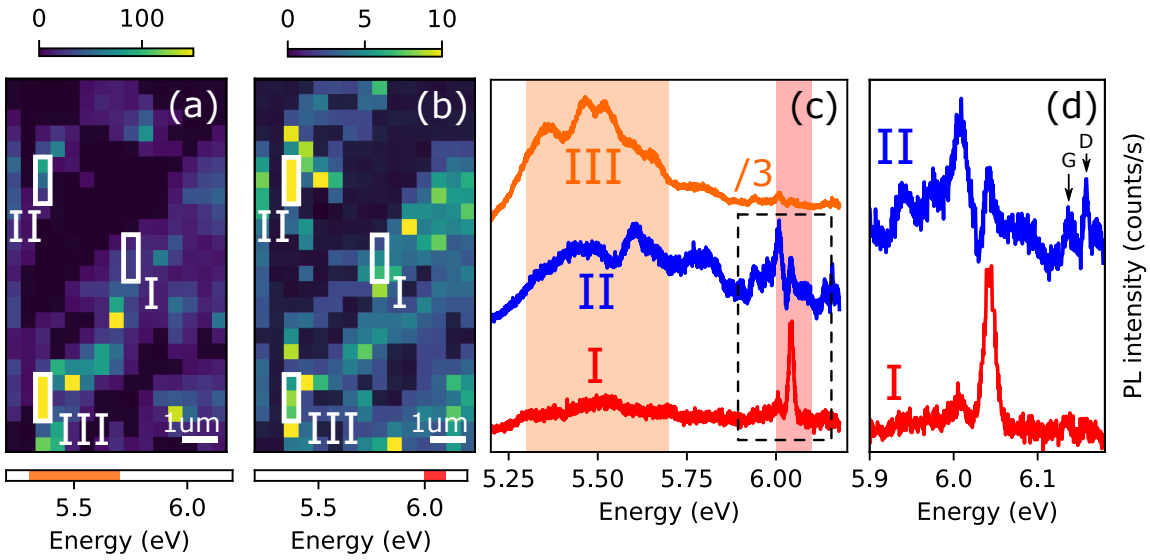

Figure 3.10: Hyperspectral image of BN258 recorded at 6 K using an excitation energy of 6.32 eV(196 nm) : (a, b) PL intensity map integrated in the range 5.3-5.7 eV (a) and 6-6.1 eV (b) represented by the orange and red shaded regions on panel (c). (c) PL spectra taken on three different points I, II and III represented on panels (a) and (b), respectively. (d) zoom of spectra I and II of panel (c) around ∼6.1 eV.

the emission of extended defects. The raw intensity spectrum integrated over (III) is plotted on panel (c) [spectrum III in Fig.3.10(c)]. The spectrum intensity is three times larger than in spectra (I) and (II) and is dominated by the emission band below 5.9 eV with 6 components around 5.36 eV, 5.46 eV, 5.52 eV, 5.6 eV, 5.65 eV and 5.79 eV. Above 5.9 eV, we observe again the multiplet structure of spectrum (II) with a similar intensity. In the low energy range of spectrum (III), the defect-related emission consists of many bands centered on different energies. However, we observe recurrent bands centered around 5.46 eV, 5.6 eV and 5.79 eV. While the first two bands barely match the energy of the so-called stacking faults emission in bulk hBN, the highest energy band matches the LO/TO phonon replica of the indirect emission in bulk hBN. We then attribute these bands to the stacking faults and phonon-assisted emission of few-layer hBN, respectively.

In all spectra, we either observe a multiplet or a singlet above 5.9 eV which we link to the Raman and PL processes under quasi-resonant excitation, following the discussion of Part 3.1, and further detailed below.

On Fig.3.11(a), we observe a good agreement between the multiplet plotted as a function of the detuning with the excitation energy at 6.33 eV(196 nm) and the second-order Raman scattering signal between 200 and 300 meV measured by *Reich et al.* on bulk hBN [86]. The second-order Raman signal, arising from the simultaneous emission of two phonons with op-

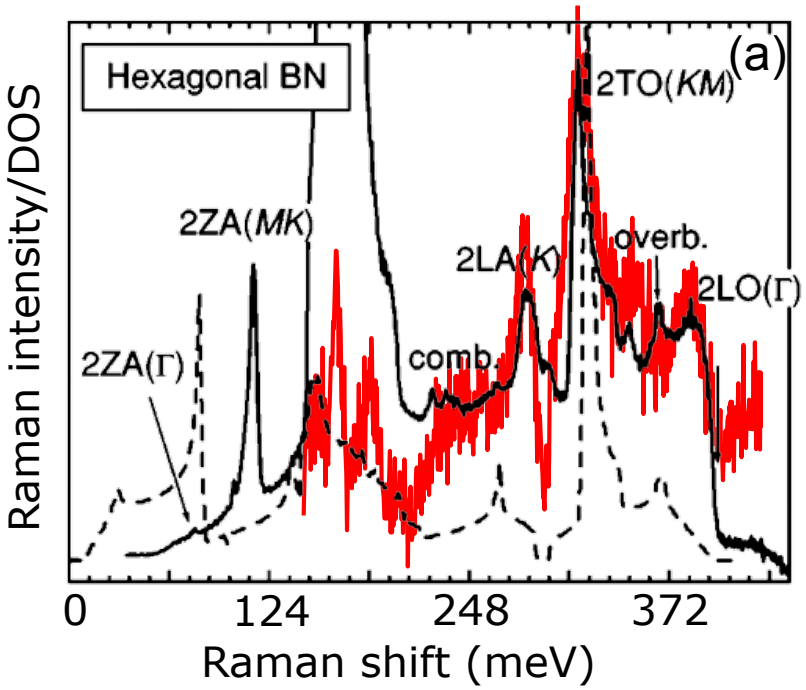

Figure 3.11: Comparison between the multiplet and the second-order Raman scattering of bulk hBN measured by *Reich et al.* [86] : (a) Second-order Raman spectrum of bulk hBN (black solid line), phonon density of states (DOS) calculated by *Kern et al.* [87] (black dashed line) and the multiplet measured above 5.9 eV of spectrum (II) as a function of the detuning with the excitation energy 6.33 eV (red line).

posite momenta everywhere in the BZ, is expected to be almost unchanged between bulk and monolayer hBN due to their very similar phonon dispersion (see Section 1.2.2). Moreover, the peaks at Raman shifts of ∼170 meV and ∼190 meV in Fig.3.11(a) match the first-order Raman scattering due to the high-energy E_{2g} mode in hBN and graphite expected around 170 meV and 196 meV, respectively. Besides these two peaks, the multiplet between 200 and 300 meV corresponds to a signal at ∼6 eV, at the vicinity of the direct bandgap resonance of monolayer hBN measured by *Elias et al.* [13]. Consequently, we interpret this multiplet as arising from the resonant second-order Raman scattering of monolayer hBN.

In contrast, the singlet at 6.04 eV is very different than the resonant second-order Raman scattering and we interpret it as the PL signal coming from the direct bandgap of monolayer hBN. In agreement with the observation of *Elias et al.* [13], this suggests that the PL is excited quasi-resonantly through the emission of pairs of phonons with opposite momentum matching the energy detuning between the direct exciton resonance and the excitation. A quantitative analysis of the PL and Raman coexistence induced by the quasi-resonant excitation will be presented in Part 3.4.

BN257

We now move to Fig.3.12 for BN257. Similarly to BN258, I_{def} [panel (a)] and I_{ML} [panel (b)] vary from 0 to 150 counts/s and 0 to 10 counts/s at the surface of the sample, respectively, and are distributed along diagonals. We then observe again a one order of magnitude decrease between I_{def} and I_{ML} as for BN258. The black pixels on panels (a) and (b) represent the areas with the lowest signal intensity (I_{def}, I_{ML} <2 counts/s) which only coincide spatially on a small rectangular region [black rectangle on the top right of the map in both panels (a) and (b)] where the signal is negligible over the whole spectrum ($I_{def} + I_{ML}$ <4 counts/s). This region is attributed to uncovered HOPG. The fraction of uncovered HOPG represents ∼6 % of the overall map, close to the value α_0∼10 % estimated from the AFM topography of BN257. The remaining black pixels on panel (b) show a strong defect-related emission below 5.9 eV on panel (a). Besides, the spatial distributions of I_{def} and I_{ML} are different and present a weak spatial anti-correlation of C∼−40 %. This indicates the detrimental effect of extended defects on the intrinsic emission of monolayer hBN. While the impact of extended defects on the intrinsic emission of few-layer (Section 3.2.3) and bulk hBN [75] has been already demonstrated, this is the first evidence of this effect in monolayer hBN.

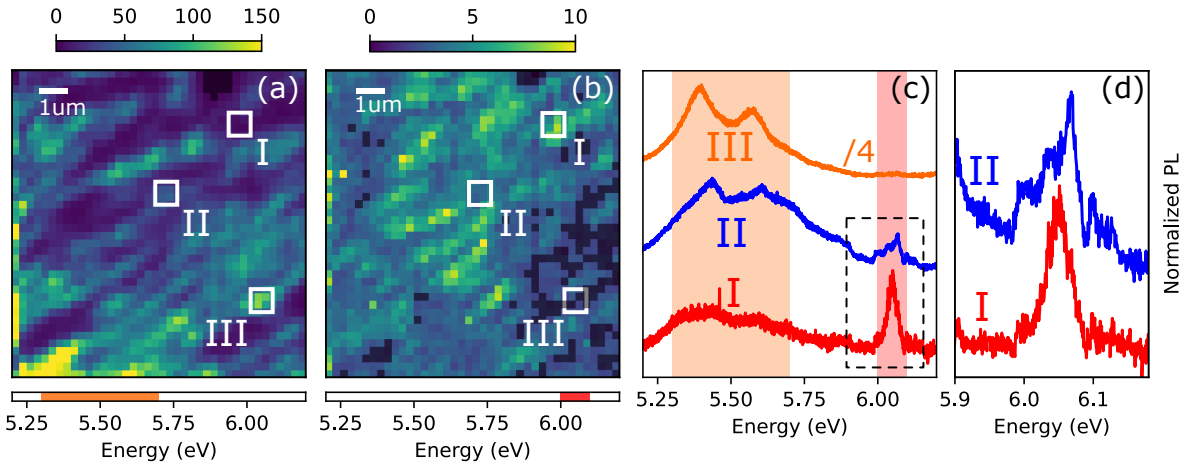

Figure 3.12: Hyperspectral image of BN257 recorded at 6 K using an excitation energy of 6.38 eV(194.2 nm) : (a, b) PL intensity image integrated in the range 5.3-5.7 eV (a) and 6-6.1 eV (b), represented by the orange and red shaded regions on panel (c). (c) PL spectra taken on three different points I, II and III represented on panels (a) and (b), respectively. (d) zoom of spectra I and II of panel (c) around ∼6.1 eV.

We now focus on the three selected areas represented by the white rectangles (I), (II) and (III) on panels (a,b) of Fig.3.12. The raw intensity spectra integrated over these areas are displayed correspondingly on spectra (I), (II) and (III) in panels (c) and (d) [Fig.3.12]. As for BN258, spectrum (I) only consists of a lorentzian peak at ∼6.05 eV, but here with a ∼40 meV linewidth, while the signal below 5.9 eV is negligible. Following our previous assignment of

Section 3.3.2, the singlet at ∼6.05 eV is attributed to the PL at the direct bandgap of monolayer hBN under quasi-resonant excitation conditions. Similarly, the multiplet above 5.9 eV displayed in spectrum (II) presents an energy detuning with the excitation energy similar to the one in BN258 [Fig.3.11(a)]. Here the excitation is 60 meV higher, thus explaining the 60 meV blue-shift in line with our interpretation as due to the resonant second-order Raman scattering under quasi-resonant excitation conditions. Besides, the defect-related emission below 5.9 eV in spectrum (II) consists of 3 bands at 5.46 eV, 5.6 eV and 5.79 eV as for BN258. Moreover, spectrum (III) is globally 4 times more intense than spectra (I) and (II) and it is dominated by the emission band below 5.9 eV which consists of 2 components at 5.36 eV and 5.55 eV. The recurrent bands observed at 5.46 eV, 5.6 eV and 5.79 eV in spectra (II) and (III) of BN258 are also observed here in spectrum (II) of BN257, and they correspond to the optical signature of few-layer hBN. Furthermore, spectrum (III) in BN257 and BN258 also displays two bands at ∼5.36 eV and ∼5.55 eV already reported on similar epitaxial few-layer hBN grown by MBE on both sapphire and HOPG substrates by *Vuong et al.* which they attributed to point defects [84].

3.4 Direct bandgap emission in monolayer hBN

In Section 3.3, my spatially-resolved PL measurements in hBN epilayers, above 6 eV, were qualitatively interpreted in terms of PL and Raman under quasi-resonant excitation conditions. In this section, I perform a quantitative analysis of the PL and Raman coexistence through the linear combination of two functions representing each process. I then use this model to fit the intrinsic signal of monolayer hBN between 5.9 eV and 6.2 eV for each point of the samples in order to extract separately the PL and Raman contributions. Through statistical analysis of the fitting parameters we then obtain a deeper insight about the complex interplay between Raman and PL processes at the origin of the optical properties of monolayer hBN.

3.4.1 Model

As demonstrated in Section 3.3, the quasi-resonant excitation of monolayer hBN induces a coexistence between second-order Raman scattering, characterized by a multiplet, and PL, characterized by a singlet. In that respect, by extracting and interpolating the experimental data of *Reich et al.*[Fig.3.11], I define a function $\mathcal{H}(x)$ representing the Raman signal. Besides, while only a singlet at ∼6.05 eV is observed for the PL of **epitaxial** monolayers, a doublet at ∼6.05 eV and ∼6.08 eV is actually required to fit the PL of the **exfoliated** monolayer, as it will be shown in Section 3.4.3, in agreement with the previous results of *Elias et al.* [13]. Therefore, our model is generalized by modeling the PL as a linear combination of two lorentzian functions with different amplitudes. Consequently, the coexistence of PL and Raman signals is accounted for by the linear combination :

$$\mathbf{F}(E) = A_0\mathcal{H}(E_{exc} - E) + A_1\mathcal{L}(E, E_{dX}, w_1) + A_2\mathcal{L}(E, E_{dX'}, w_2) \tag{3.6}$$

with $\mathcal{L}$ a lorentzian function, E the energy of the detected photon, E_{exc} the excitation energy, A_0 the amplitude of the Raman signals and $E_{dX}/E_{dX'}$, w_1/w_1 and A_1/A_2 the energy, the linewidth

and the amplitude of the two PL lines, respectively. Both $\mathcal{H}$ and $\mathcal{L}$ are normalized functions so that A_0, A_1 and A_2 represent the effective amplitude of each process. Therefore, the PL (η_{PL}) and Raman (η_R) contributions to the the overall signal between 5.9 eV and 6.2 eV are defined as:

$$\eta_R = \frac{A_0}{A_0 + A_1 + A_2 + \delta} \tag{3.7}$$

$$\eta_{PL} = \frac{A_1 + A_2}{A_0 + A_1 + A_2 + \delta} \tag{3.8}$$

where δ accounts for the fit error at each point so that $A_0 + A_1 + A_2 + \delta$ corresponds to the signal integrated from 5.9 eV and 6.2 eV over the experimental data. Fig.3.13(c) gives a schematic representation of our model.

3.4.2 Epitaxial monolayer hBN

We use this model to analyze the intrinsic emission of monolayer hBN in the region 5.9-6.2 eV for BN258 and BN257. We first fit spectra (I) and (II) of Fig.3.12(d) (BN257) and Fig.3.10(d) (BN258). Fig.3.13 shows the results of our modeling for BN258 [panel (a)] and BN257 [panel (b)]. In panels (a) and (b), the fits are represented by the black curves while the PL component is represented by the red shaded area delimitated by the black dashed line and the Raman component is represented by the blue shaded area, respectively. The Raman component lies in energy above and below the PL line at ∼6.05 eV in BN257 and BN258, respectively, with respect to the excitation energy used for each sample. In all spectra, A_2 is at least ∼20 times smaller than A_0 and A_1, in agreement with the previous assignment of the PL to a singlet at ∼6.04 eV in epitaxial samples. This leads us to neglect the contribution of the PL line at ∼6.08 eV in the fit of the data recorded in epitaxial monolayer hBN ($A_2 \sim 0$) so that $\eta_{PL} \sim \frac{A_1}{A_0+A_1+\delta}$ and $\eta_R \sim \frac{A_0}{A_0+A_1+\delta}$.

For BN258, we used an excitation energy of 6.32 eV leading to a second-order Raman signal centered around ∼6 eV. In the top spectrum, the PL signal consists of a narrow peak of ∼13 meV linewidth which contributes to η_{PL}∼41 % to the overall signal. The Raman signal contributes to the low energy component of the recorded spectrum at ∼6 eV. The bottom spectrum is on the contrary completely dominated by the Raman signal with a negligible PL contribution of η_{PL}∼3 %.

For BN257, we used an excitation energy of 6.38 eV leading to a second-order Raman signal centered around ∼6.05 eV. As we can see in panel (b), the PL signal centered at 6.048 eV in both spectra fully overlaps with the Raman signal. In the top spectrum, the signal is dominated by the PL signal with η_{PL}∼65 %, and a PL linewidth of ∼38 meV. In the bottom spectrum, the signal is dominated by the Raman signal with η_{PL}∼30 %, and the PL linewidth is ∼48 meV. Our fits reproduce nicely the different experimental spectra taken on the two samples with a fit error lower than 10 % showing the relevance of our model to analyze our data.

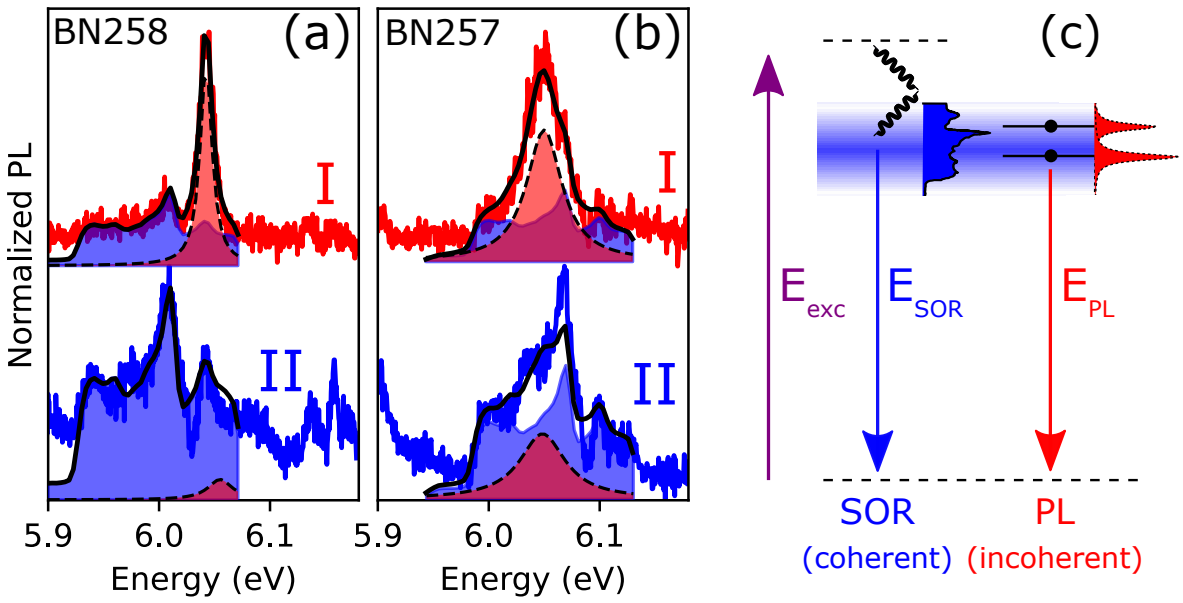

Figure 3.13: (a,b) Results of the fit of spectra (I) and (II) of Fig.3.10(c,d) and Fig.3.12(c,d) in the region 5.9-6.2 eV for BN257 [panel (a)] and BN258 [panel (b)]. The fits are shown by the black curves while the PL component is represented by the red shaded area delimitated by the black dashed line and the Raman component is represented by the blue shaded area. (c) Schematic representation of our model on the coexistence of the PL/Raman signals for the quasi-resonant excitation of monolayer hBN.

We applied the above procedure to fit the signal between 5.9-6.2 eV for any position on the hyperspectral images of BN257 [Fig.3.15] and BN258 [Fig.3.14]. Fig.3.14 shows the results for BN258 where panel (a) shows the overall intensity map integrated in the range 5.9-6.2 eV [identical to Fig.3.10(b)] while panels (b-e) represent the maps of the Raman and PL amplitudes (A_0 - b, A_1 - c) and contributions (η_R - d, η_{PL} - e), respectively.

As seen in Section 3.3.2, the overall intensity of the intrinsic signal [panel (a)] dominates along both diagonal and vertical lines corresponding to the border of the uncovered HOPG areas identified in Section 3.3.2 [black pixels on Fig.3.10(b)]. In panel (b), A_0 varies from 1 to 15 counts/s with a mean value of ∼2.4 counts/s and a standard deviation of 1.51 counts/s, and is found to be spatially correlated (C∼97 %) with the overall intensity map of panel (a). Because $\alpha_{ML} \sim \alpha_{hBN}$ in BN258, this suggests than the Raman signal is enhanced along the edges of the uncovered HOPG areas. In panel (c), A_1 varies from 0 to 3 counts/s with a mean value of ∼0.38 counts/s and a standard deviation of ∼0.36 counts/s and presents a different spatial distribution from panels (a) and (b) with C∼27 % and ∼13 %, respectively. From the map of A_1, the PL seems to be confined inside some areas between the HOPG edges, with a typical lateral size of ∼3 µm, matching the one of monolayer hBN observed on the AFM topography of BN258 (see Section 3.3.1). Remarkably, the Raman signal is in average 6 times stronger than the PL ($< \frac{A_0}{A_1} > \sim 6$) and it dominates the overall intensity map as evidenced by the strong

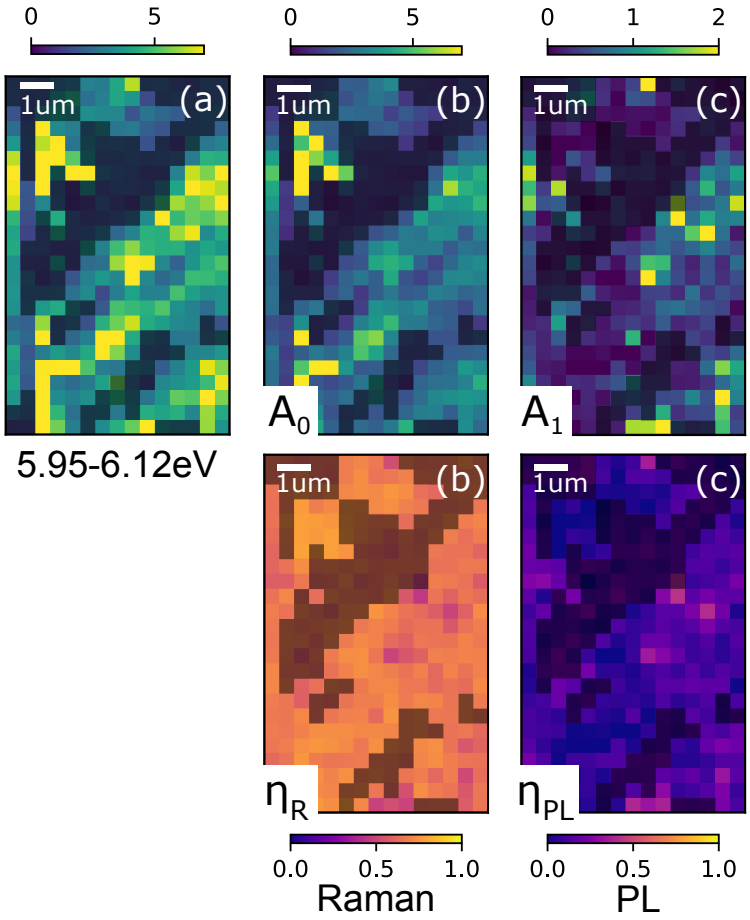

Figure 3.14: Fitting parameters of the hyperspectral image on BN258. (a) Map of the overall signal intensity integrated over 5.9-6.2 eV [identical to Fig.3.10(b)] given by the color code on top. (b-e) Maps of the Raman and PL amplitudes (A_0 - b, A_1 - c) and contributions (η_R - d, η_{PL} - e) extracted from the fits where the color maps are given by the colorbar on the top and bottom of each map, respectively. The color maps have been saturated in order to resolve the intensity variations. The black pixels represent the areas where $A_0 + A_1$ <2 counts/s which we attribute to HOPG.

similarities between panels (a) and (b).

In panel (d), η_R varies from 45 to 78 % with a mean value of ∼66 % and standard deviation of 5 % while, in panel (e), η_{PL} varies from 0 to 42 % with a mean value of ∼11 % and standard deviation of 8 %. Again, we find a sixfold increase between the mean values of η_R and η_{PL} indicating the predominance of the Raman signal. Importantly, η_R and η_{PL} are spatially anti-correlated from each other (C∼−85 %) and both match the spatial distribution of A_1 [panel (c)]. Accordingly, the spatial variations of η_R and η_{PL} appear to be induced by the variations of A_1 with opposite dependence.

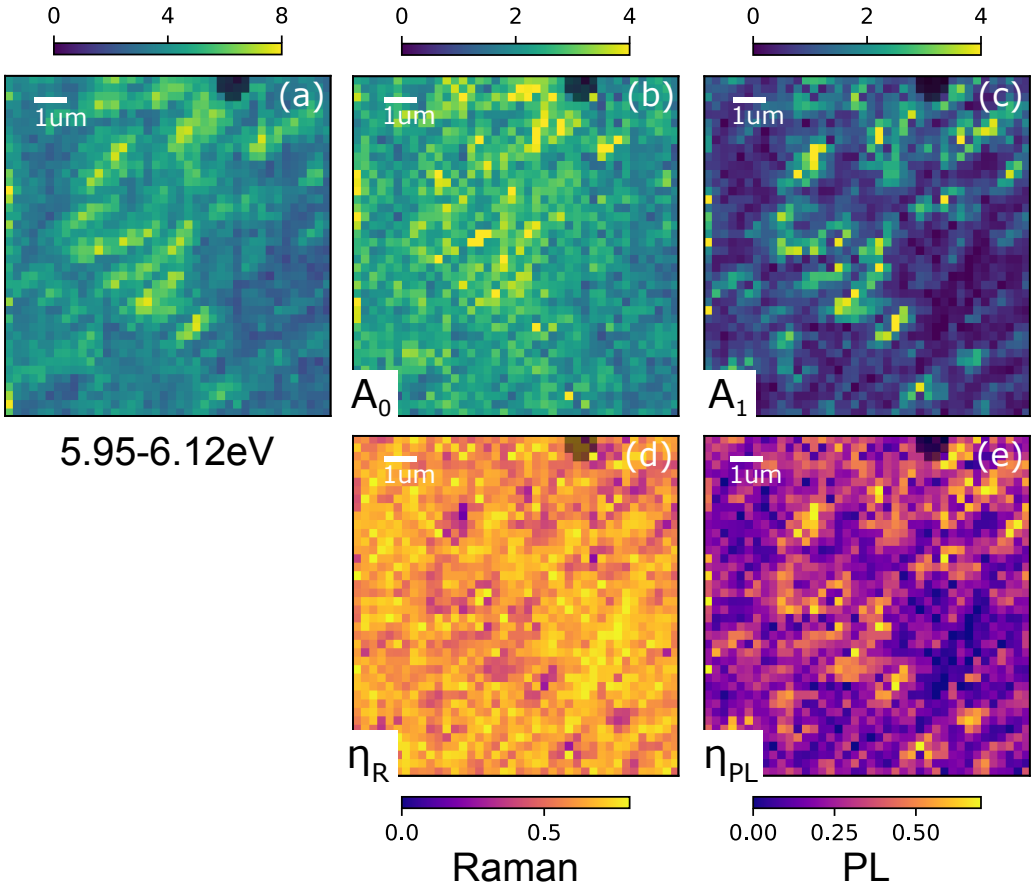

Figure 3.15: Fitting parameters of the hyperspectral image on BN257. (a) Map of the overall signal intensity integrated over 5.9-6.2 eV [identical to Fig.3.10(b)] given by the color code on top. (b-e) Maps of the Raman and PL amplitudes (A_0 - b, A_1 - c) and contributions (η_R - d, η_{PL} - e) extracted from the fits where the color map are given by the colorbar on the top and bottom of each map, respectively. The black pixels represent the areas where $A_0 + A_1$ <2 counts/s which we attribute to HOPG.

Let us now switch to Fig.3.15 presenting the results for BN257 where panel (a) shows the overall intensity map integrated in the range 5.9-6.2 eV [identical to Fig.3.12(b)] while panels (b-e) represent the maps of the Raman and PL amplitudes (A_0 - b, A_1 - c) and contributions (η_R - d, η_{PL} - e), respectively.

Again, the overall intensity of the intrinsic signal [panel (a)] is distributed along diagonal lines almost parallel to each other which we assigned to HOPG edges (see Section 3.3.2). In panel (b), A_0 varies from 0 to 6 counts/s with a mean value of ∼2.3 counts/s and a standard deviation of 0.57 counts/s, and is spatially correlated (C∼74 %) with the overall intensity map of panel (a). However, in contrast to BN258, A_0 is more uniform and shows less pronounced localization along the diagonal lines visible in panel (a). In panel (c), A_1 varies from 0 to 6 counts/s with a mean value of ∼1.1 counts/s and a standard deviation of ∼0.86 counts/s, and

appears localized along the bright areas observed in panel (a). A_1 is also spatially correlated ($C{\sim}72\,\%$) with the overall intensity map of panel (a), but is weakly correlated ($C{\sim}14\,\%$) with A_0. The typical lateral size of the brightest areas in panel (c) is on the order of a micrometer in agreement with the typical monolayer domains observed on the AFM topography of BN257 [ML region on Fig.3.9(a)]. Moreover, the Raman signal is on average only twice stronger than the PL ($< \frac{A_0}{A_1} > \sim 2$) while the overall intensity map in panel (a) seems to arise from the balanced contribution of the Raman [panel (b)] and PL [panel (c)] signals. This discrepancy with BN258 could be explained by a reduced Raman enhancement on the HOPG edges due to the small fraction of uncovered HOPG areas ($\alpha_0{\sim}6\,\%$) in BN257 leading to a more uniform Raman signal.

In panel (d), η_R varies from 17 to 81 % with a mean value of ∼60 % and a standard deviation of 10 % while, in panel (e), η_{PL} varies from 0 to 92 % with a mean value of ∼25 and standard deviation of 14 %. We thus find a 2.5 ratio between the mean values of η_R and η_{PL} close to the one discussed above for A_0 and A_1. As in BN258, η_R and η_{PL} are spatially anti-correlated ($C{\sim}-86\,\%$) and they match the spatial distribution of A_1 [panel (c)], thus supporting our attribution of the origin of the spatial variations of η_R and η_{PL} as induced by the variations of A_1.

Our statistical analysis of A_0 and A_1 for BN257 and BN258 is summarized in Tab.3.2. Remarkably, the values are fairly similar between the two samples despite their different topography and the spatial distribution of the PL signal. This suggests that the same physical processes occur at different scales in the two samples. Surprisingly, $< A_1 >$ is ∼2.5 times lower in BN258 than in BN257 which is opposite with α_{ML} that is twice higher in BN258. This could be due to an effect of the quasi-resonant excitation as it will be discussed in Section 3.4.4.

	$< A_0 >$	$< A_1 >$	$< \eta_R >$	$< \eta_{PL} >$	$C(A_0, A_1)$	$C(\eta_R, \eta_{PL})$
BN257	2.3±0.57	1.1±0.86	60±10 %	15±14 %	14 %	−86 %
BN258	2.4±1.51	0.38±0.36	66±5 %	11±8 %	13 %	−85 %

Table 3.2: Summary of the statistical analysis of A_0 and A_1 for BN257 and BN258.

Finally, in Fig.3.16 we show the spatial variations of E_{dX} extracted from the fits of the hyperspectral images of BN257 (panel (a)) and BN258 (panel (b)). In panel (a), E_{dX} varies from 6.03 to 6.06 eV with a mean value of 6.048 eV and a standard deviation ∼4 meV. The distribution is uniform over the whole map except for the two bright areas on top with a typical lateral size of ∼1 µm where $E_{dX}{\sim}6.06$ eV. Interestingly, these areas lie at the border of the uncovered HOPG region of BN257 identified in Section 3.3.2 [black pixels on Fig.3.12(b)]. Consequently, the ∼20 meV blue-shift observed in these areas may be due to local strain induced by the HOPG edges onto hBN monolayers. In panel (b), E_{dX} varies from 6.03 to 6.07 eV with a mean value of 6.046 eV and a standard deviation of ∼7 meV. It is less uniform than in BN257, displaying similarities with the spatial distribution of A_1 in Fig.3.15(c). Panel (c) shows the histograms of E_{dX} for BN257 [blue bars] and BN258 [orange bars] using a bin width of 1.5 meV. In both

samples, the distribution of E_{dX} follows a normal law [orange and blue curves in Fig.3.16(c)] that can be modeled using gaussians at positions 6.0475 eV and 6.0445 eV) with a full-width half-maximum (FWHM) of ∼8 meV and ∼10 meV) for BN257 and BN258, respectively. It is worth noting that the ∼3 meV shift between the two gaussians is more than twice smaller compared to the 8-10 meV linewidth precluding any physical interpretation.

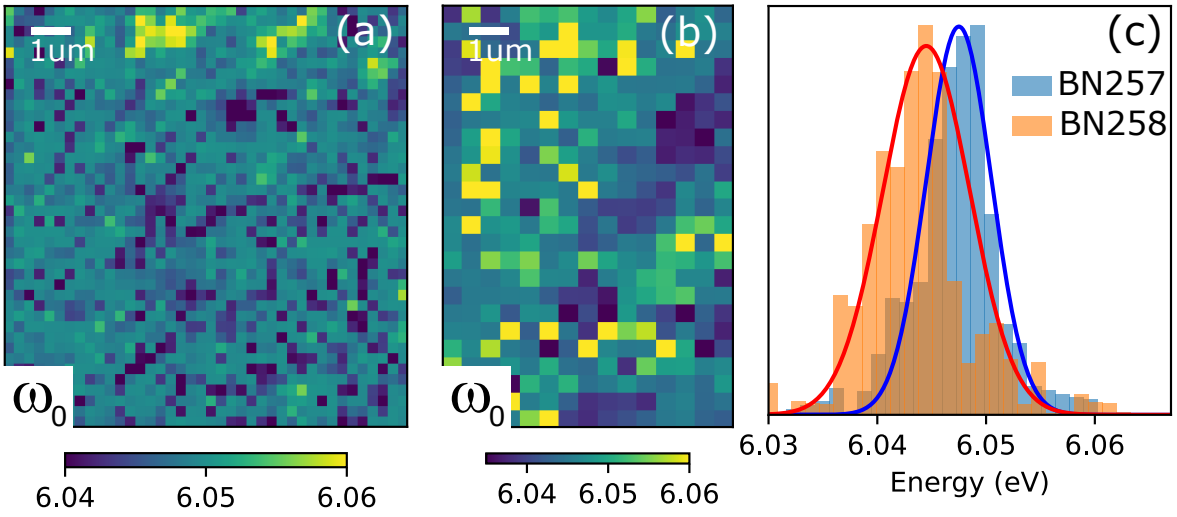

Figure 3.16: (a, b) Spatial variations of E_{dX} extracted from the fits of the hyperspectral images of BN257 (a) and BN258 (b). (c) Histograms of E_{dX} weighted by A_1 for BN257 [blue bars] and BN258 [orange bars] using a bin width of 1.5 meV which the distribution follows a normal law represented by the blue and orange gaussian curve, respectively.

The linewidth (w_1) of the lorentzian function accounting for PL in the fits of BN257 and BN258 is estimated at 47±6 meV and 26±12 meV, respectively. Interestingly, these values are close to the 20-30 meV radiative broadening of the direct optical bandgap of monolayer hBN assessed from deep-UV reflectivity measurements on epitaxial monolayers by *Cassabois et al.* [45]. This indicates that w_1 is locally dominated by, or of the order of the homogeneous broadening. The inhomogeneous broadening of the order of ∼10 meV extracted from the distribution of E_{dX} [Fig.3.16(c)], is indeed smaller than w_1. Our results are consistent with the PL linewidth of 32 meV on epitaxial monolayer hBN measured by *Elias et al.* [13], where the PL signal is collected from macroscopic areas of ∼50 µm equivalent in size to our maps. This confirms the small inhomogeneous broadening of the direct bandgap emission in epitaxial monolayer hBN and our spatially-resolved measurements reveal that it originates from inhomogeneities partly below the size of our laser spot, and partly above it following the morphology of the HOPG substrate.

3.4.3 Exfoliated monolayer hBN

We now apply our model to the case of the exfoliated monolayer hBN studied in Part 3.2. Because the signal on the exfoliated monolayer is uniform [Fig.3.6], we integrate the PL spectrum over the whole monolayer in order to improve the signal-to-noise ratio. Fig.3.17 shows the results of the fit in the case of a model accounting for only the Raman component [panel (a)], the Raman and the high-energy PL component [panel (b)] and the Raman and the two PL components [panel (c)]. We obtain a very good agreement between our experimental data and our fit for the model including both the Raman and the two PL components [panel (c)].

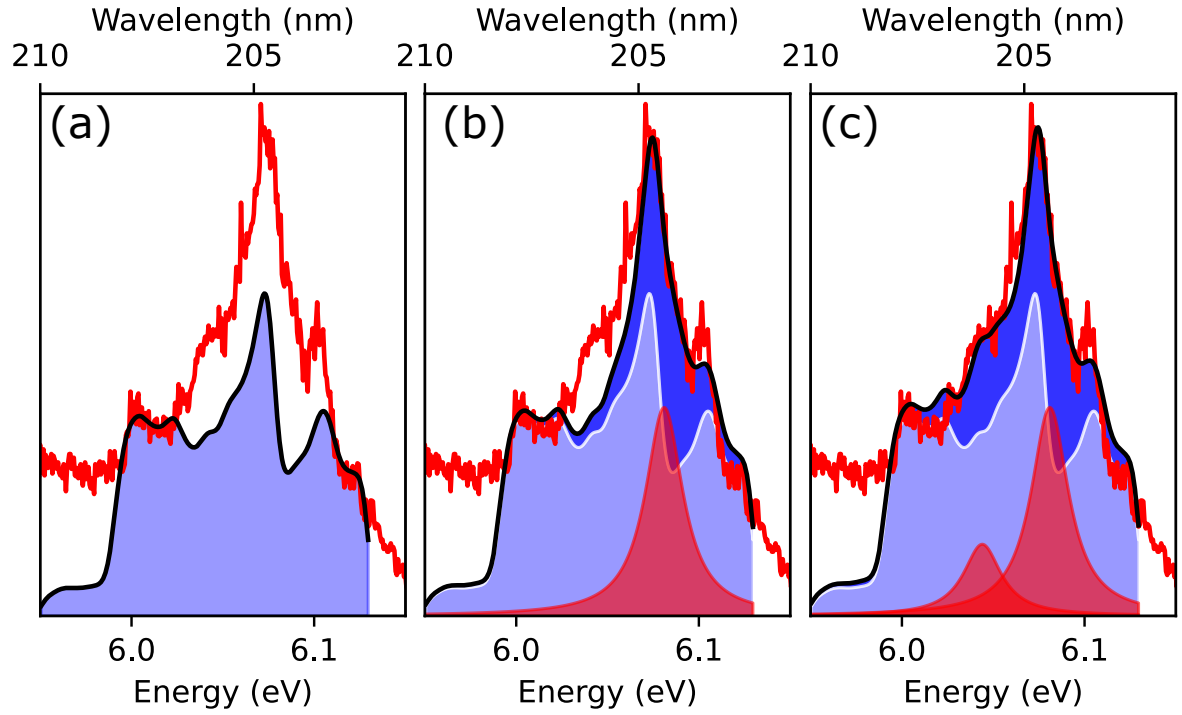

Figure 3.17: Results of the fit [black line] of the exfoliated monolayer hBN spectrum [red lines] in the case of a model accounting for (a) only the Raman component [$\mathbf{F}(E) = A_0\mathcal{H}(E_{exc} - E)$], (b) the Raman and the high-energy PL component [$\mathbf{F}(E) = A_0\mathcal{H}(E_{exc} - E) + A_1\mathcal{L}(E, E_{dX}, w_1)$], (c) the Raman and the two PL components [$\mathbf{F}(E) = A_0\mathcal{H}(E_{exc} - E) + A_1\mathcal{L}(E, E_{dX}, w_1) + A_2\mathcal{L}(E, E_{dX'}, w_2)$]. The Raman and PL components are represented by the blue and red-filled curves, respectively. The darker blue areas between the fit results and the Raman represent the integrated PL signal.

In panel (a), the excitation energy of 6.389 eV places the Raman component [blue filled curve in Fig.3.17] between 6 and 6.1 eV. Remarkably, the Raman multiplet coincides with the lines of the experimental spectrum at ∼6 eV, ∼6.07 eV and ∼6.1 eV. In panel (b), the high-energy PL component, centered at 6.081 eV with a linewidth of 25 meV, reduces drastically the fit error by filling most of the gap between the Raman component and the experimental spectrum around ∼6.08 eV. Finally, in panel (c), the low-energy PL component, centered at 6.044 eV with

a linewidth of 25 meV, leads to a fit error below 10 %. Besides, from the amplitude of each component extracted from the fit, the PL and Raman contribution to the overall signal between 5.9 and 6.12 eV are η_{PL}~25.5 % and η_R~65 %, respectively, where the contribution of the low- and high-energy PL components represent correspondingly 5.5 % and 20 %. Interestingly, these values are similar to the ones obtained on epitaxial monolayers in Section 3.4.2.

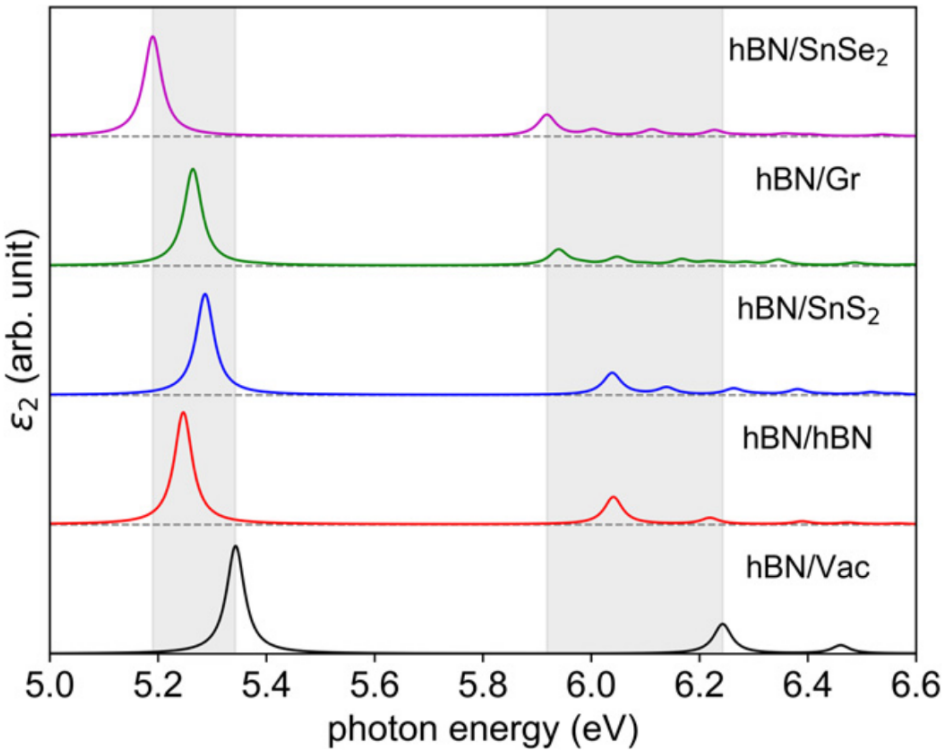

Figure 3.18: Absorption spectra obtained from DFT calculations including the BSE (with e–h interaction) for monolayer hBN interfacing with various substrates. The curves from the bottom to the top are for (hBN/Vac) free-standing monolayer hBN, (hBN/hBN) monolayer hBN/hBN, (hBN/SnS_2) monolayer hBN/SnS_2, (hBN/Gr) monolayer hBN/Graphene, (hBN/$SnSe_2$) monolayer hBN/$SnSe_2$ heterostructures [55].

The energies of the two PL lines at 6.044 eV and 6.081 eV match the energy of the PL doublet at ~6.05 and 6.08 eV reported by *Elias et al.* on epitaxial monolayer hBN [13]. As seen in Section 1.1.4, the negligible shift between the PL doublet of the two samples, in spite of their different substrates, is explained by the compensating effect of the dielectric screening of the Coulomb interaction on the electronic bandgap energy and the binding energy of dX (or dX'). This results in similar values for the energy of dX and dX' regardless of the dielectric screening induced by the substrate [13]. Fig.3.18 shows the simulated the absorption spectra for monolayer hBN interfacing with various substrates obtained recently from *ab initio* calculations using the BSE [55]. Accordingly, the shift of the resonance corresponding to dX at ~5.4 eV induced by the substrates dielectric screening is estimated to be lower than ~150 meV while the shift of the binding energy is of the order of 2 eV. However, this do not explains the observation of a singlet

in epitaxial monolayers. In the next section, I demonstrate that this may originate from the selective excitation of dX in our quasi-resonant excitation conditions.

3.4.4 The origin of the PL doublet

Our results on the two epitaxial samples only show a single PL line at ∼6.05 eV, in discrepancy with the PL doublet observed in both exfoliated [88] and epitaxial [13] monolayer hBN. While the PL doublet was observed on similar samples by *Elias et al.* [13], we attribute the observation of a single PL line to the selective excitation in our quasi-resonant excitation conditions. Indeed, the quasi-resonant excitation also leads to a dependence on the relative amplitude of the PL lines with respect to the excitation energy detuning. The PL is excited by a pair of phonons of opposite momenta matching the energy detuning between dX (or dX') and the excitation. Therefore, the efficiency of the quasi-resonant excitation depends on the two-phonon joint density of states at the energy of dX (or dX').

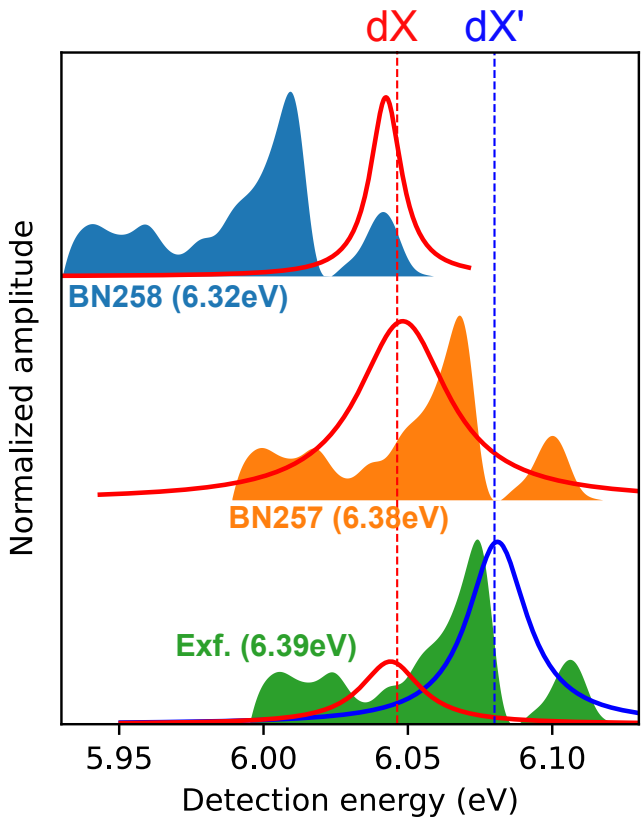

Figure 3.19: Plots of the Raman and PL components extracted from the fits of BN258 [spectrum (I) of Fig.3.13 - on top], BN257 [spectrum (I) of Fig.3.15 - in the middle] and the exfoliated monolayer [Fig.3.16 - on the bottom]. The normalized Raman components are represented by the orange, blue and green-filled curves, respectively. The position of dX and dX' estimated at ∼6.048 eV and ∼6.08 eV are represented by the blue and red vertical lines, and the corresponding PL lines are represented by the blue and red curves, respectively. For the exfoliated monolayer, the PL lines are normalized by the amplitude of the highest one.

Fig.3.19 displays the PL [blue and red solid curves in Fig.3.19] and Raman [filled curves in Fig.3.19] components extracted from the fit in the three samples. The positions of dX and dX' estimated at 6.048 eV and 6.08 eV, are represented by the blue and red vertical lines, respectively. For BN258, the excitation energy of 6.32 eV places the second-order Raman signal in the range 5.93-6.06 eV, thus leading to an overlap of the high energy component of the Raman signal only with dX. This leads to the observation of a PL line at 6.042 eV. On the contrary, the excitation range does not overlap with dX' resulting in the absence of PL at ∼6.08 eV. For BN257, the excitation energy of 6.38 eV places the second-order Raman signal in the range 5.99-6.12 eV. The low energy component of the Raman signal overlaps again with dX thus leading to the observation of the PL line at 6.048 eV. Reciprocally, dX' falls in the gap between the high and low energy components of the two-phonon density of states resulting in a negligible excitation of dX'. Correspondingly, no PL is observed at ∼6.08 eV. Finally, for the exfoliated monolayer, the excitation energy of 6.39 eV places the second-order Raman signal in the range 6-6.13 eV. In these conditions, the low energy components of the Raman signal overlap with dX and dX'. Accordingly, two PL lines at 6.044 and 6.081 eV are observed rather than a single PL line ∼6.04 eV like for epitaxial monolayers. The relative amplitudes of the two PL lines coincide with the ones of the two-phonon density of states at dX and dX', respectively, thus supporting our argument on the dependence of the quasi-resonant excitation with the overlap.

Our results demonstrate that each PL line within the doublet corresponds to an excitonic state, denoted as dX and dX', at approximately ∼6.04 eV and ∼6.08 eV, respectively. This further indicates that the PL doublet does not arise from phonon-assisted processes but more probably from two distinct direct excitons dX and dX' built from carriers in K and K' valleys, respectively. Further experiments are required to fully elucidate the origin of the PL doublet.

I thus demonstrated the ability of our model to reproduce the direct bandgap emission in both exfoliated and epitaxial hBN monolayers, thus providing a complete and unified description of the emission profile of the direct bandgap emission for all types of hBN monolayer. Moreover, I also evidenced the impact of the quasi-resonant excitation on the relative amplitude of the PL lines with respect to the excitation energy detuning resulting, notably, to the selective excitation of a single PL line at ∼6.04 eV in epitaxial monolayers.

3.5 Conclusion

In this chapter, I performed a systematic study of the optical properties of monolayer hBN for both exfoliated and epitaxial hBN monolayers for different conditions of excitation using our deep-UV microscope. Thanks to the high spatial resolution and the hyperspectral imaging enabled by our deep-UV microscope, I could isolate and identify the PL signal of hBN monolayers in our samples. On the exfoliated sample, I observed a dramatic change of the PL signal when moving away from few-layer hBN, showing a series of PL lines similar to the ones of the indirect emission in bulk hBN, to monolayer hBN, showing only an emission centered at 6.08 eV closed to

the energy of the PL doublet measured by *Elias et al.* on epitaxial monolayers [13]. By studying the dependence of the indirect emission with the thickness of hBN in the few-layer regime, I then demonstrated a substantial modification of the intensity ratio of the phonon replicas, where LA/TA phonon replicas decrease with the thickness. However, the origin of the line broadening of the phonon replicas commonly observed in few-layer hBN is still undetermined. Next, I studied two epitaxial samples differing by the hBN coverage and displaying completely different topography in AFM. In these two samples, either a multiplet or a singlet are distinctly observed above 6 eV which I attributed to the coexisting Raman and PL signal, respectively, induced by the quasi-resonant excitation. I then developed a quantitative model based on the linear combination of functions representing the Raman and PL signals in order to perform a quantitative analysis of my results. By fitting at each point of the different maps, I then extracted the PL and Raman contributions as well as the energy and the broadening of the PL lines at each point of the maps. From the spatial analysis of the PL and Raman contributions in the two epitaxial samples I concluded on the enhancement of the Raman signal at the HOPG edges while both signals are systematically observed in hBN monolayers. By applying the same model to the PL spectrum recorded in an exfoliated monolayer, I evidenced the presence of a PL doublet at similar energies to the one observed by *Elias et al.* [13]. Finally, the conversion of the PL emission from a singlet in epitaxial monolayers to a doublet in exfoliated monolayer hBN is attributed to the selective excitation induced by the quasi-resonant excitation. This leads me to conclude that the origin of the PL doublet arises from the two direct excitons dX and dX' built from carriers in K and K' valleys, respectively.

Chapter 4

Bernal boron nitride

This chapter is dedicated to the study of the optical properties of hBN polytypes with a particular focus on AB-hBN. I used deep-UV microscopy to isolate a AB-hBN crystal from the combination of photoluminescence (PL) and second-harmonic generation (SHG) microscopy. This enabled me to study the optical properties of AB-hBN from the deep-UV (band edge emission) to the UVB (deep levels emission) providing a direct insight into the impact of stacking on the optical properties of hBN.

Contents

3.1 Optical properties of monolayer hBN 47
3.2 Exfoliated monolayer hBN 51
3.2.1 Sample topography 51
3.2.2 Hyperspectral imaging in the deep-UV 54
3.2.3 Indirect bandgap emission in few-layer hBN 56
3.3 Epitaxial monolayer hBN 59
3.3.1 Samples topography 59
3.3.2 Hyperspectral imaging in the deep-UV 61
3.4 Direct bandgap emission in monolayer hBN 66
3.4.1 Model 66
3.4.2 Epitaxial monolayer hBN 67
3.4.3 Exfoliated monolayer hBN 73
3.4.4 The origin of the PL doublet 75
3.5 Conclusion 76

4.1 hBN polytypes in the literature

While hBN is standardly observed in the AA' stacking sequence (AA'-hBN), other stacking sequences of hBN are thermodynamically stable corresponding to the so-called hBN polytypes as seen in Chapter 4 Section 1.2. Among them, bernal (AB-hBN) and rhombohedral (ABC-hBN) boron nitrides are predicted as the most stable hBN polytypes along with AA'-hBN. However, because of their similar cohesive energy, these polytypes are prone to coexist making the fabrication of single-crystal hBN difficult. The use of microscopy techniques is thus essential to study the physical properties of a given hBN polytype. Moreover, because hBN polytypes only differ by their stacking, their identification is challenging as it requires several complementary techniques. Therefore, there have been very few reports on the identification of high-quality hBN

polytypes single crystals to date. Consequently, while the optoelectronic properties of AA'-hBN have been studied extensively this last decade in high-quality AA'-hBN crystals, little is known about the physical properties of other hBN polytypes.

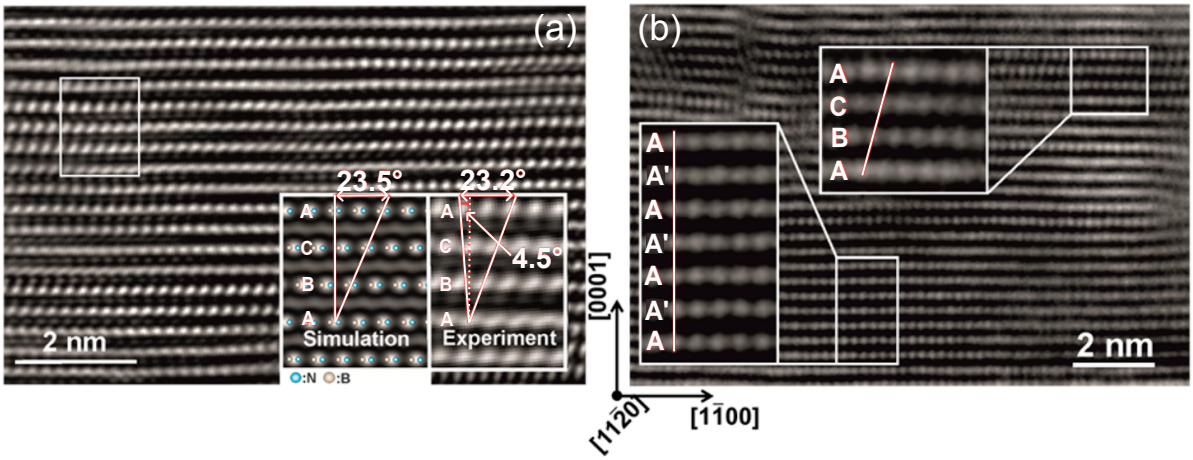

Figure 4.1: Cross-section HRTEM images of hBN layers grown via CVD on (a) 6H-SiC and (b) α-Al_2O_3 substrates, respectively [38]. The insets of panels (a) and (b) show a zoom of selected areas represented by the white rectangles. The red lines in the inset show the layers alignment which are vertical for AA'-hBN and diagonal for ABC-hBN.

In 1951, *Pease et al.* used X-ray diffraction (XRD) on high-quality hBN powders to demonstrate the dominant AA' stacking sequence in hBN [89]. Later in 1990, *Solozhenko et al.* [90] prepared for the first time a ∼98 % containing ABC-hBN powder verified a few years later by *Kurdyumov et al.* using XRD [36]. The same year, *Liu et al.* showed the cBN to ABC-hBN transformation via laser heating of a cBN grain powder above 1795 K by measuring simultaneously the Raman spectra for different powers of the laser. The presence of ABC-hBN in the cBN grains after laser heating was evidenced from its Raman peak at 800 cm^{-1} [39]. In 2015, *Chubarov et al.* grew a polytype-pure ABC-hBN film via CVD on a 6H-SiC substrate [38]. In their study, they showed the effect of the underlying substrate on the preferential growth of a given hBN polytype using high-resolution TEM (HRTEM) as depicted in Fig.4.1. In Fig.4.1, panels (a) and (b) show the cross-section HRTEM images of hBN layers grown via CVD on 6H-SiC and α-Al_2O_3 substrates by *Chubarov et al.*, respectively [38]. The hBN stacking extracted from the two HRTEM images is shown in the inset of panels (a) and (b) correspondingly. On 6H-SiC [panel (a)] they found a predominance of ABC-hBN everywhere in the hBN layer, characterized by a lateral shift angle of ∼23.5° every four layers. Besides, on α-Al_2O_3 the first ∼13 layers correspond to AA'-hBN [Fig.4.1(a)] while the remaining layers correspond to ABC-hBN. They attribute this transition to the surface temperature decrease of the sample with the thickness of deposited hBN thus inducing a transition to ABC-hBN after 13 layers. This suggests that ABC-hBN is formed at a lower temperature than AA'-hBN.

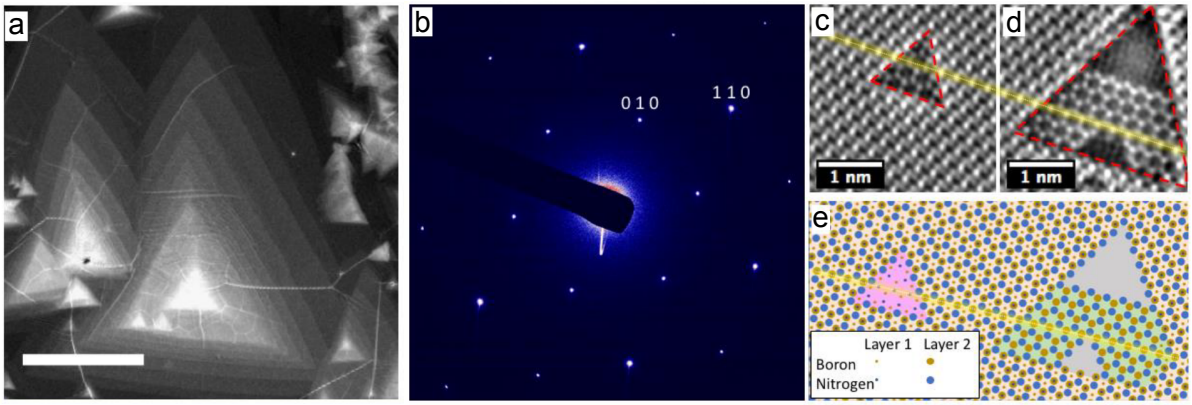

Figure 4.2: (a) SEM image of CVD-grown AB-hBN flakes on Cu [40]. Scale bar = 10 µm. (b) SAED spectrum of the AB-hBN flake where the first-order <010> diffraction peaks are three times weaker than the second-order <110> diffraction peaks [40]. (c, d) HRTEM image of two different areas on the AB-hBN flakes near mixed bilayer/monolayer hBN regions thus showing typical AB boundaries (red dashed triangles) [40]. (e) Schematic position of each atom in (c,d) [40].

Although AB-hBN has been predicted by many theoretical works as the most stable of the hBN polytypes including AA'-hBN, one should wait until 2019 for its first observation in multilayer hBN [40]. *Gilbert at al.* grew virtually pure AB-hBN flakes via CVD on both Fe and Cu metallic substrates as shown in Fig.4.2. Panel (a) [Fig.4.2] shows the SEM image of the CVD-grown AB-hBN flakes with thicknesses going from 1 up to 10 layers. The concentric triangular shape is an indication of a parallel stacking of hBN layers while an anti-parallel stacking would rather induce a star-like shape. Moreover, the selected-area electron diffraction (SAED) spectrum of the flake [panel (b) of Fig.4.2] shows a three-fold increase of the second-order diffraction peaks, corresponding to the 110 planes family, relative to the first-order diffraction peaks, corresponding to the 100 planes family. This result is consistent with the AB, AB' and A'B stackings, where the two lasts correspond to anti-parallel stackings. Finally, the AB-stacking is directly evidenced by HRTEM [panels (c, d and e) of Fig.4.2] where the hBN hexagons are laterally shifted by $\delta = \frac{a}{\sqrt{3}}$ as confirmed by the simulations on the atomic positions for the AB stacking.

In spite of these few reports on AB-hBN and ABC-hBN in the literature, their optical properties are still unknown due to the absence of large, high-quality crystals. Alternatively, *Bourrellier et al.* used CL microscopy inside a TEM to evidence the impact of the different stackings on the optical properties of hBN then contributing to the so-called stacking faults emission [75]. Fig.4.3(a) shows the imaginary part of the dielectric functions in the deep-UV of the different stackings of hBN bilayers calculated via *ab intio* calculations in *Bourrellier et al.* [75]. The lorentzian peaks in the spectra of Fig.4.3(a) correspond to the different exciton resonances for each stacking, thus giving a general estimation of their absorption/emission spectra. We observe a distribution of the resonance depending on the stacking going from 5.2 to 6 eV where most of

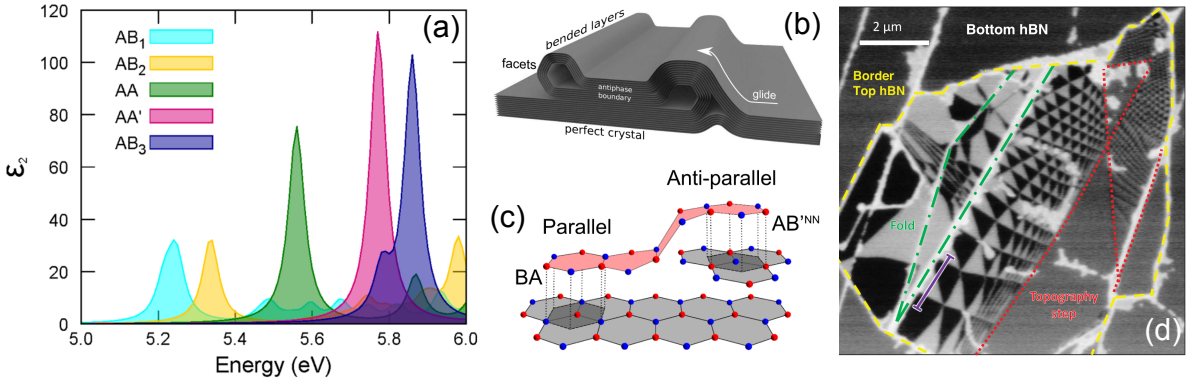

Figure 4.3: (a) Imaginary part of the dielectric function (optical absorption spectrum) for different hBN stacking obtained in the framework of GW + BSE calculations [75]. (b) Model of a faceted double fold in a hBN crystal leading to layers sliding and antiphase boundaries [75]. (c) Illustration of hBN bilayers for parallel (BA) and anti-parallel (AB'^{NN}) stackings at the origin of an out-of-plane charge polarization [91]. (d) Kelvin probe map showing oppositely polarized domains of AB/BA stacking (black and white) separated by sharp domain walls [92].

the optical bandgaps lie below the one of AA' with the exception of AB_3 (AB stacking in our notation). Therefore, they suggest that layer glidings [Fig.4.3(b)] engender a broad range of hBN stackings contributing to the low energy band below 5.7 eV, attributed to the stacking faults emission in hBN which they found to be spatially localized along crystal lines. In 2018, *Sponza et al.* calculated the excitonic dispersion of the different hBN polytypes in order to study the effect of the stacking on the optical bandgap of polytypes as already discussed in Section 1.2.4 [32].

More recently, in 2021, ferroelectricity was observed in twisted hBN layers using electric force (or Kelvin probe) microscopy by three different groups [91–93]. They showed that the ferroelectricity, forbidden by symmetry in the AA' stacking, arises from the AB domains inducing a strong out-of-plane electric dipole due to interfacial charge polarization [Fig.4.3(c,d)]. Furthermore, *Stern et al.* [92] demonstrated that this interfacial polarization in AB stacked hBN layers enables superlubricity where the two layers move relatively to each other under the application of an electric field in the out-of-plane direction so that electric dipoles align to the electric field. This unravels the significant impact of stacking through the modification of the symmetries on the optical properties of hBN.

Surprisingly, while hBN exhibits unique optical properties extensively studied in AA'-hBN, the optical properties of other hBN polytypes have remained unexplored to date. This is primarily due to the lack of large, high-quality crystals, and the technical difficulty associated with optical spectroscopy in the deep-UV. Interestingly, these two experimental limitations could be circumvented by investigating microscopic inclusions of hBN polytypes commonly found in polytypic crystals, using spatially-resolved PL microscopy in the deep-UV. **Importantly, this would allow us to uncover the optical properties of other hBN polytypes, such as**

AB-hBN or ABC-hBN polytypes, and determine how the stacking may influence their optical properties.

In this chapter, I investigate the optical properties of the bernal boron nitride polytype (AB-hBN) by means of our deep-UV microscope. In Part 4.2, I demonstrate the first isolation of a AB-hBN crystal optically identified through the combination of second-harmonic generation (SHG) and photoluminescence (PL) microscopy. In Part 4.3, I perform an in-depth study of the optical properties of AB-hBN in both the deep-UV and UVB ranges. Remarkably, I unravel the quasi-degeneracy of the optical bandgap resulting in simultaneous direct and indirect band-edge emissions in AB-hBN. This leads to different thermal broadening for the direct and indirect transitions which is explained by the dramatic effect of light-matter coupling for the direct exciton. Moreover, the deep-level emission in the UVB associated to the so-called 4.1 eV defects in hBN is modified in AB-hBN thus demonstrating the dependence with the stacking order.

4.2 Optical identification of a AB-hBN crystal

This part is dedicated to the optical isolation and identification of a AB-hBN crystal obtained from a polytypic crystal using deep-UV microscopy. In Section 4.2.1 I present X-ray diffraction and PL measurements at the macroscopic scale in our polytypic sample and in a high-quality AA'-hBN crystal. In Section 4.2.2, I then use our deep-UV microscope on a flake detached from the polytypic crystal to identify and isolate a few micrometer-size AB-hBN crystal through the combination of PL and SHG microscopies.

4.2.1 Macroscopic characterization

The sample was grown by the group of *Pr. James H. Edgar* in the Kansas State University (KSU) using a modified version of the Ni-Cr flux method where 2 g of graphite powder has been added to a Ni-Cr mixture (20 g Ni + 20 g Cr) and 1 g of hot-pressed BN powder. The mixture was heated to 1345 °C to produce a molten solution, then slowly cooled at a rate of 0.5 °C/h so that B and N atoms precipitate to the surface to form hBN crystals [94, 95]. A gas mixture of CO and N_2 was flowing through the furnace during the whole process to react with and remove any oxygen in the system. The hBN crystals are then carefully removed from the solidified Ni-Cr ingot when completely cooled. A picture of our sample [labeled C33] is shown in Fig.4.4(a). A high-quality bulk AA'-hBN crystal [labeled Fe72] obtained from the standard Fe-Cr flux method previously reported by *Pr. Edgar's group* is shown on Fig.4.4(b) for comparison [96]. The Fe72 sample consists of millimeter-sized triangular transparent domains displaying interference colors at the edges, typical of high-quality hBN crystals. Drastically different is our C33 sample which consists of a granitic-like crystal made of micrometer-size (<10 µm) hBN crystals [white crystals on Fig.4.4(a)] embedded inside a dark material probably resulting from the graphite powder agglomeration [darker regions on Fig.4.4(a)].

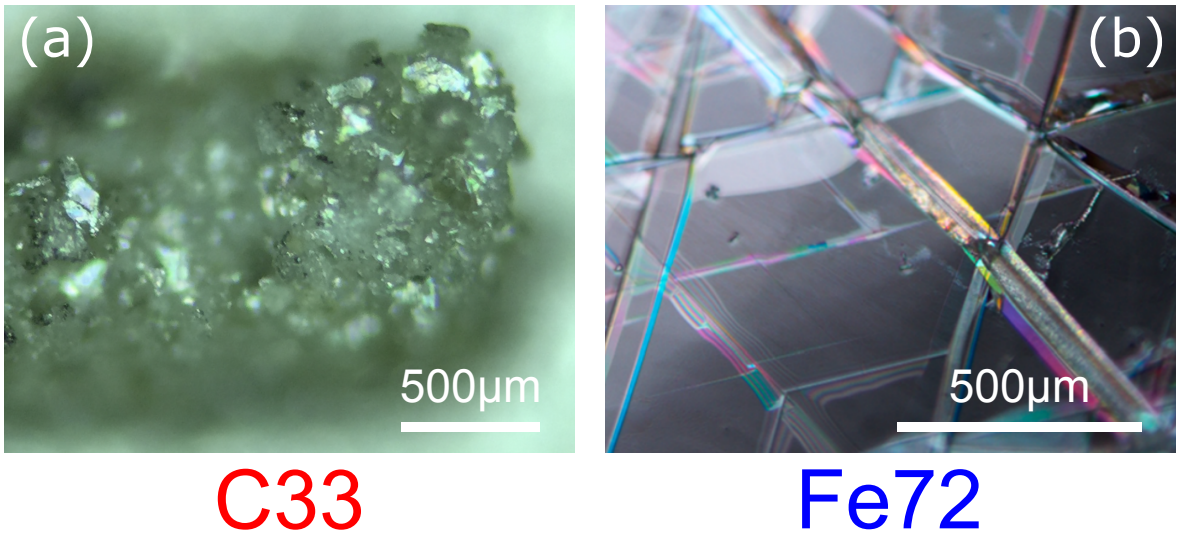

Figure 4.4: Pictures of the C33 (a) and Fe72 (b) samples.

The $\theta - 2\theta$ XRD spectra of the C33 (in red) and the Fe72 (in blue) samples are shown in Fig.4.5(a). The XRD spectra have been recorded at room temperature by our collaborator *Dr. Matthieu Moret* using a Bruker D8DISCOVER diffractometer with a VÅntec linear detector in the Bragg-Brentano configuration. To increase the detectivity, a simple Göbel mirror has been used resulting in a non-monochromatic primary beam [Cu(Kα1 + Kα2)] with some traces of Cu(Kβ) and W(LA1) highlighted by the asterisks on Fig.4.5(a). The calculated 2θ x-ray diffraction angles of the different hBN polytypes with the corresponding crystal orientation are presented on Tab.4.1.

Both XRD spectra show three main peaks at ∼27°, ∼55° and 87.8°. These peaks arise from the out-of-plane periodicity of hBN and they are labeled (0,0,n), (0,0,2n) and (0,0,3n), respectively, where n(=1, 2 or 3) corresponds to the number of layers in the stacking period of hBN polytypes. In that respect, the position of these (0,0,qn) peaks is given by the Bragg law :

$$sin(\theta) = \frac{qn\lambda}{2c_0} \tag{4.1}$$

with θ the Bragg angle, c_0 the interlayer distance, λ the wavelength of the primary beam (λ =1.5406 Å for the Cu(Kα_1) transition) and q(=1, 2 or 3) the diffraction order. From the XRD data we thus extracted c_0 ∼3.42 Å in agreement with what was previously measured by *Kurdyumov et al.* at room temperature on high-quality hBN powders [36]. The full-width half-maximum (FWHM) of the (0,0,n) peak is ∼0.16° and ∼0.25° in Fe72 and C33, respectively, very close to the canonical value of ∼0.14° reported on high-quality hBN crystals [97]. Accordingly, both samples consist of high-quality hBN crystals with long-range stacking orders along the c-axis. As seen in Section 1.2.1, c_0 may vary with the stacking, so that a shift of the (0,0,qn) diffraction peak may occur depending on the hBN polytypes. Such characteristic shift on the order of ∼0.01° cannot be resolved here because of the ∼0.1° FWHM of the response function

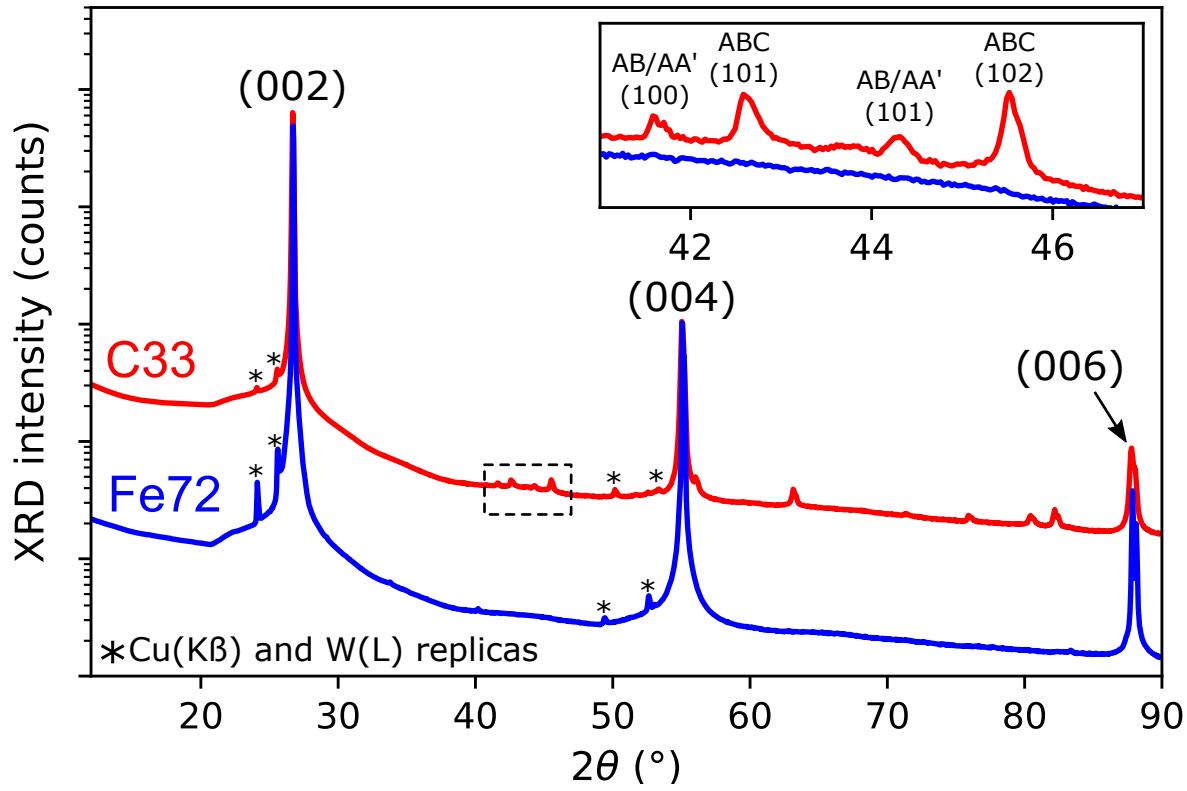

Figure 4.5: $\theta - 2\theta$ XRD spectra of C33 (red line) and Fe72 (blue line) at room temperature recorded in the Bragg-Brentano configuration with a non-monochromatic beam from Cu(Kα1 + Kα2) transitions. Inset: zoom of the θ ∼40–47° region displaying tiny diffraction peaks coming from disoriented hBN crystals with different stacking order.

limited by the non-monochromatic primary beam.

Interestingly, we observe a series of small diffraction peaks at 41.59°, 42.6°, 44.3° and 45.5° in C33 which are absent in AA'. A magnification of the 40–47° region is shown in inset of Fig.4.5. Based on the calculations, the peaks at 41.59° and 44.3° match indistinctly with the (100) and (101) diffraction peaks of both AA'-hBN and AB-hBN whereas the peaks at 42.6° and 45.5° match with the (101) and (102) diffraction peaks of ABC-hBN. Accordingly, the peaks in the region 40–47° arise from disoriented hBN crystals under the x-ray beam deviating from the $\theta - 2\theta$ configuration resulting in diffraction peaks from other crystal directions than the c-axis. The observation of these peaks only in C33 thus suggests a larger crystal orientation disorder than in Fe72 in agreement with the one of macroscopic morphology shown in Fig.4.4 where the granitic aspect of C33 contrasts with the flat Fe72. Therefore, the peaks at 42.6° and 45.5° induced by the crystals disorientation evidence the presence of ABC-hBN in C33 while the two other peaks result from AA' or AB-hBN. Consequently, C33 is a polytypic crystal containing AA'-hBN, ABC-hBN, and perhaps AB-hBN crystals.

The macro PL spectra measured on C33 and Fe72 are represented by the red and blue spec-

2θ(deg.)	AA	AA'/AB	ABC
26.77	001	002	003
41.65	100	100	-
42.66	–	–	101
43.91	–	101	-
45.60	–	–	102
50.20	101	102	-
55.15	002	004	006
56.17	–	–	104
59.59	–	103	-
63.28	–	–	105
71.42	102	104	-
76.01	210	210	110
80.57	–	–	107
82.27	211	212	113
85.55	–	105	-
87.96	003	006	009

Table 4.1: Table of the 2θ powder diffraction values with their corresponding diffracting planes calculated for the different hBN polytypes using copper as an x-ray source.

tra of Fig.4.6, respectively. In the region above 6 eV [delimitated by the dashed line on Fig.4.5] the PL signal has been magnified hundred times on both spectra in order to resolve the peak at 6.032 eV in C33. The PL spectra have been recorded inside a home-built macro PL setup developed by our team which uses the same laser source as our deep-UV microscope. It is focused in a 20 µm-spot on our samples with a fused silica lens of 100 mm focal length. The samples are cooled to cryogenic temperatures (6 K) inside a closed-loop He cold-finger cryostat. Then, the PL emitted by the samples is collected achromatically through a set of spherical and plane UV-enhanced aluminium mirrors and focused at the entrance slit of a Czerny-Turner spectrometer equipped with a CCD camera similar to the one used in our deep-UV microscope.

The Fe72 spectrum corresponds to the typical PL spectrum of AA'-hBN described in detail at the end of Section 1.2.4. Drastically different is the PL spectrum recorded on C33. First, the stacking fault emission below 5.7 eV in C33 shows band maxima at 5.29 eV, 5.37 eV, 5.52 eV and 5.61 eV while band maxima in AA'-hBN are typically found at 5.29 eV, 5.33 eV, 5.47 eV, 5.57 eV and 5.64 eV. Second, the phonon replicas associated to the indirect bandgap emission in the 5.75-6 eV region in AA'-hBN cannot be resolved in C33 where they are replaced by a broad emission band extending between 5.65 and 5.8 eV. Third, while no signal is observed above 6 eV in AA', a lorentzian peak is resolved at 6.032 eV with a linewidth of ∼17 meV. We thus attribute these differences to the presence of different hBN polytypes in C33, as first evidenced by XRD. As shown in Fig.1.13, calculations predict tiny variations of the hBN optical bandgap of the order of a few tens of meV for different hBN polytypes. Accordingly, the band edge emission of hBN polytypes should also lie in the deep-UV range (5.4-6.6 eV), as for AA'-hBN. Since the domains in C33 are typically smaller than the spot size, this results in an average contribution of

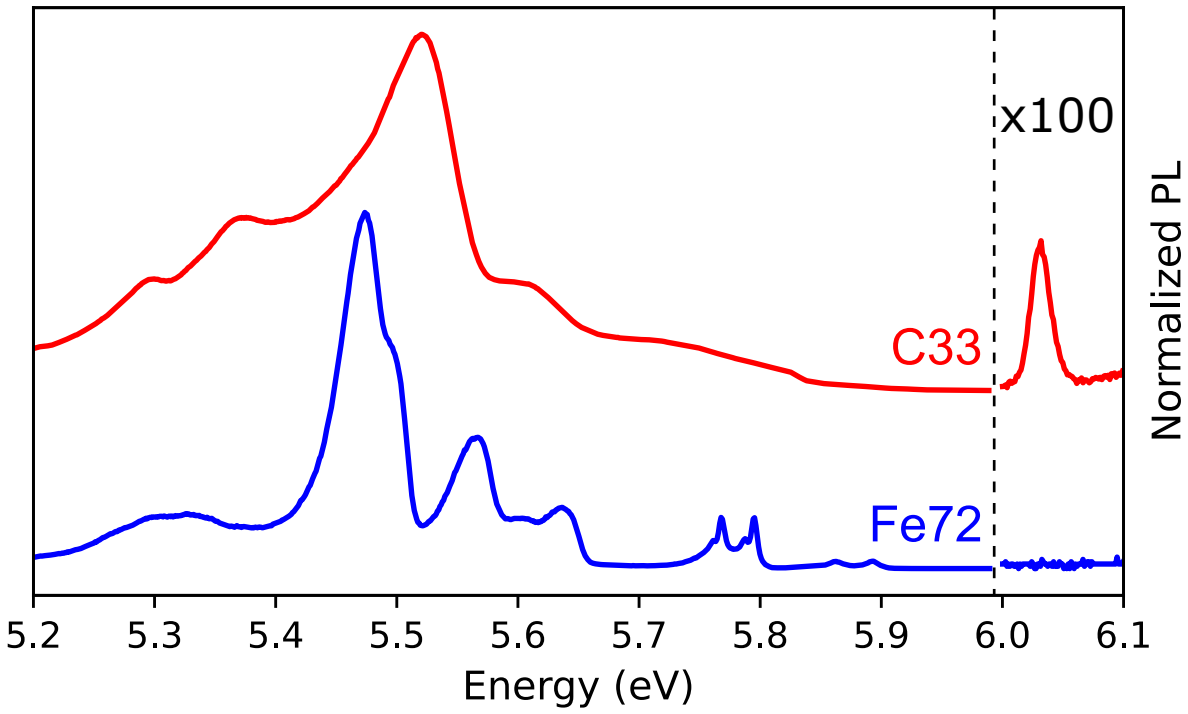

Figure 4.6: Normalized PL spectra of C33 (red line) and Fe72 (blue line) in the deep-UV recorded at 8 K and excited by a deep-UV optical excitation at 6.35 eV focused on a 20 µm spot. The signal above 6 eV is magnified 100x in order to resolve the peak at ∼6.04 eV.

the hBN polytypes by macro PL in C33. Consequently, the emission below 6 eV consists of the mixed contribution of the intrinsic and stacking faults emission of the different hBN polytypes including AA'-hBN. In contrast, the sharp peak at 6.032 eV most probably arises from a single hBN polytype distinct from AA'-hBN.

Due to the micrometer-size of the hBN crystals in C33, sub-micrometric spatial resolution is required to spatially isolate them. While the emission of hBN polytypes overlaps below 6 eV making their optical discrimination complex, the sharp emission at 6.032 eV can be used to uniquely isolate the hBN polytype at the origin of its emission. In the next part, I use deep-UV microscopy on a flake detached from C33 to spatially isolate a single hBN polytype crystal. Then, by performing a parallel study of the SHG and the 6.032 eV PL signals over the same area, I show that this polytype corresponds very likely to AB-hBN.

4.2.2 Microscopic characterization

A flake of C33 deposited over a silicon substrate covered by a 80 nm silicon oxide layer similar to the one used for exfoliated monolayer hBN (Section 3.2.1) has been obtained through mechanical exfoliation via the standard scotch tape technique. Fig.4.7 shows an optical image

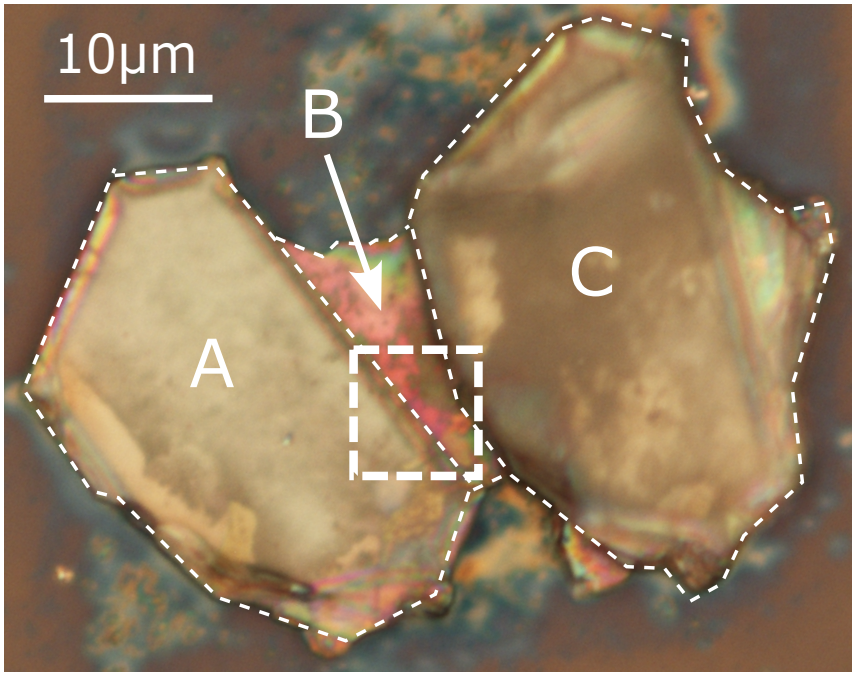

Figure 4.7: Wide field image in the visible domain of a piece of our polytypic sample C33, consisting of two AA'-hBN crystals (AA' regions) sandwiching one AB-hBN crystal (AB region). The dotted box delimitates the 6.5 µm × 6.5 µm region corresponding to Fig.4.8.

of our sample under white light illumination in a standard wide-field optical microscope. In the following, we will show that the two large colorless regions [A and C in Fig.4.7] correspond to two AA'-hBN crystals while the pink triangular region in the central part [B in Fig.4.7] corresponds to a AB-hBN crystal. The B region has a lateral size going from 2 to 7 µm and a ∼10 µm length corresponding to a surface of ∼50 µm^2. Besides, the A and C regions show similar shape with a typical lateral size and length of ∼17 µm and ∼30 µm resulting in a ∼400 µm^2 area. In that respect, the B region is almost ten times smaller than the A and C regions. The similar shape of the two A and C regions suggests that they may originate from the same hBN crystal which has been split along the basal direction during the mechanical exfoliation.

As seen in Section 3.2.1, the oxide layer on top of the substrate gives rise to Fabry-Perot interferences in the visible inducing variations of the optical contrast with the thickness of the hBN layers on top. Under white light illumination, this results in a change of the hBN color with the thickness in the thin layers regime. Therefore, the pink color of the B region corresponds to thicknesses of ∼200 nm as confirmed by AFM topography at the sample edges. The non-uniform optical contrast shifting from pink to green on the edges of the B region indicates variations in the hBN thickness. Besides, the colorless A and C regions correspond to larger hBN thicknesses leading to Fabry-Perot interferences outside the visible range. The thicknesses of the A and C regions measured by AFM are ∼500 nm and ∼1.2 µm, respectively. Even if the thickness variations result in different optical contrasts of the regions in Fig.4.7, at this

stage there is no way to identify the stacking order and to differentiate the crystalline phases from one crystal to another whatever the operating mode of the optical microscope (bright-field, darkfield, polarization-contrast). In the following, I will show how by combining SHG and PL microscopies in the deep-UV, we can discriminate the different hBN polytypes in our sample and obtain insight into the stacking order.

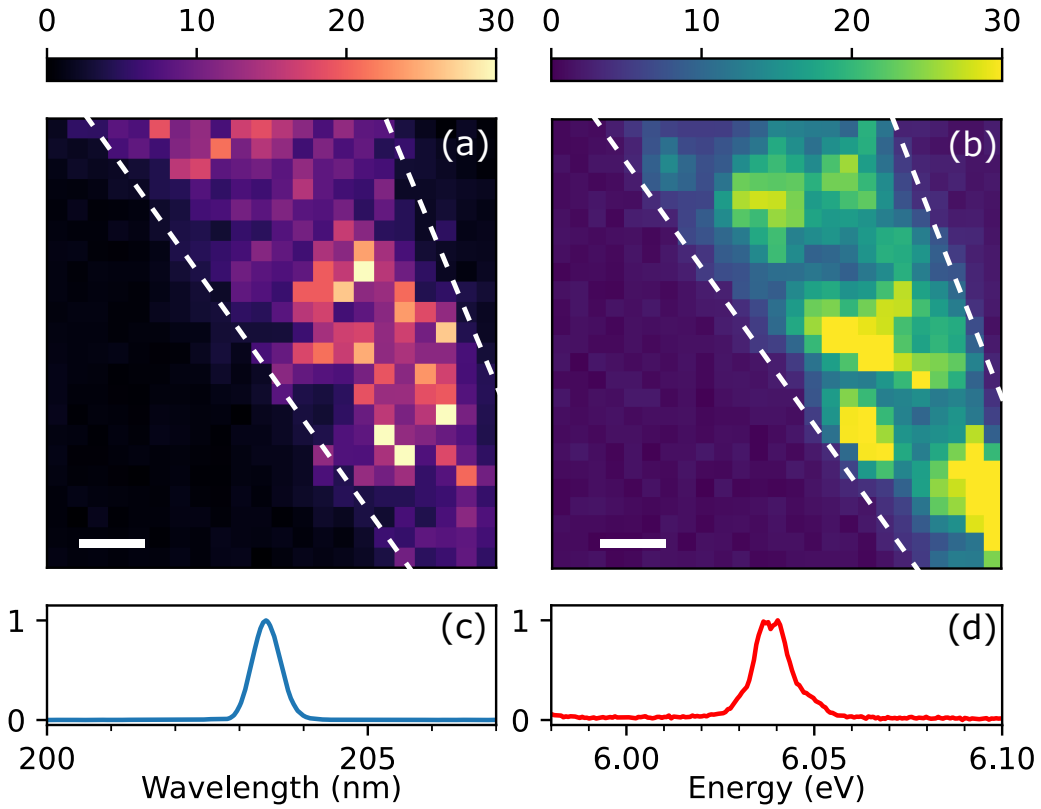

Figure 4.8: Second harmonic generation (SHG) and photoluminescence (PL) intensity maps at 6 K recorded over the same area indicated by the dotted box on Fig.4.7: (a) map of the SHG signal at 203.2 nm, (b) map of the PL signal integrated over the range 6-6.1 eV, (c) normalized SHG spectrum under excitation at 406.4 nm, (d) normalized PL spectrum above 6 eV under one-photon excitation at 6.39 eV (194 nm). Scale bar = 1 µm. The dotted lines are guides for the eyes.

Fig.4.8 shows the SHG [panel (a)] and the PL [panel (b)] intensity maps recorded at ∼6 K over the same area represented by the dotted box in Fig.4.7. The area of investigation overlaps both with the B region [delimitated by the white dashed line in Fig.4.7] and the two A and C regions on each side. For the SHG intensity map, we used a 2ω excitation at 406.4 nm and measured the intensity of the SHG signal at 203.2 nm for each pixel of the map. Panel (c) shows the normalized SHG spectrum in the deep-UV. For the PL intensity map, we used a 4ω excitation at 6.39 eV (194 nm) and measured for each pixel of the map the intensity of the PL

signal integrated over the range 6-6.1 eV. Panel (d) shows the normalized PL spectrum typically measured in this range where we only observe the peak at ∼6.038 eV which we attribute to the optical signature of a hBN polytype different from AA'-hBN.

The SHG intensity [panel (a)] varies from 0 to 30 counts/s and is only observed inside the B region while it vanishes completely in the A and C regions. Because SHG is only allowed in non-centrosymmetric crystals, this suggests that the inversion symmetry is broken in the B region but exists in the A and C regions. As shown in Section 4.2.1, the only hBN polytypes that can compose our sample are the AA'-hBN, AB-hBN and ABC-hBN polytypes as evidenced by the XRD spectrum of the C33 sample. Among the three hBN polytypes, AA'-hBN is the only centrosymmetric phase while the two others are non-centrosymmetric. We therefore unambiguously attribute the A and C regions to AA'-hBN crystals while the central region could either consist of a AB-hBN or a ABC-hBN crystal. The identification of AA'-hBN crystals is far from surprising since the growth protocol is here a variant of the well-established fabrication techniques for high-quality hBN. On the contrary, the observation of SHG is the first indication of the stabilization of another hBN polytype (AB-hBN or ABC-hBN).

Very similar is the PL intensity map shown on panel (b). As for SHG, the PL intensity varies from 0 to 30 counts/s and is localized inside the B region while it also vanishes in the A and C regions. We thus observe a one-to-one correspondence between the SHG and PL maps demonstrating that the SHG and the PL at ∼6.04 eV originate from the same non-centrosymmetric polytype. The absence of PL signal at ∼6.04 eV in the A and C regions is consistent with our previous identification of AA'-hBN crystals in which the optoelectronic properties are well-documented and only present emission below the indirect bandgap at 5.95 eV (see Section 1.2.4). First-principles calculations of the optoelectronic properties of hBN polytypes, presented in Section 1.2.4, predict a blue(red)-shift of the AB(ABC)-hBN optical bandgap relatively to the AA'-hBN bandgap, respectively. Therefore, the observation of the blue-shifted emission at ∼6.04 eV in the non-centrosymmetric region suggests that it corresponds to a AB-hBN crystal.

Although the SHG and PL signals are solely detected in the central region, we note spatial inhomogeneities in both intensity maps. This raises the question about the local order of the AB-hBN crystals and the eventuality of small AB-hBN inclusions inside a AA'-hBN phase. By using two-photon PL excitation (PLE) spectroscopy we demonstrate below the existence of a coherent AB-hBN crystal phase where the stacking order is preserved over the whole crystal.

PLE spectroscopy allows to retrieve the intrinsic optical response of a crystal through the dependence of the intensity of its PL signal with the excitation wavelength. Moreover, two-photon excitation has been demonstrated to be a powerful technique for elucidating the optoelectronic properties of hBN and, notably, two-photon PLE spectroscopy enables to resolve the sharp optical response at ∼6.06 eV in AA'-hBN [7]. Consequently, two-photon PLE spectroscopy shows

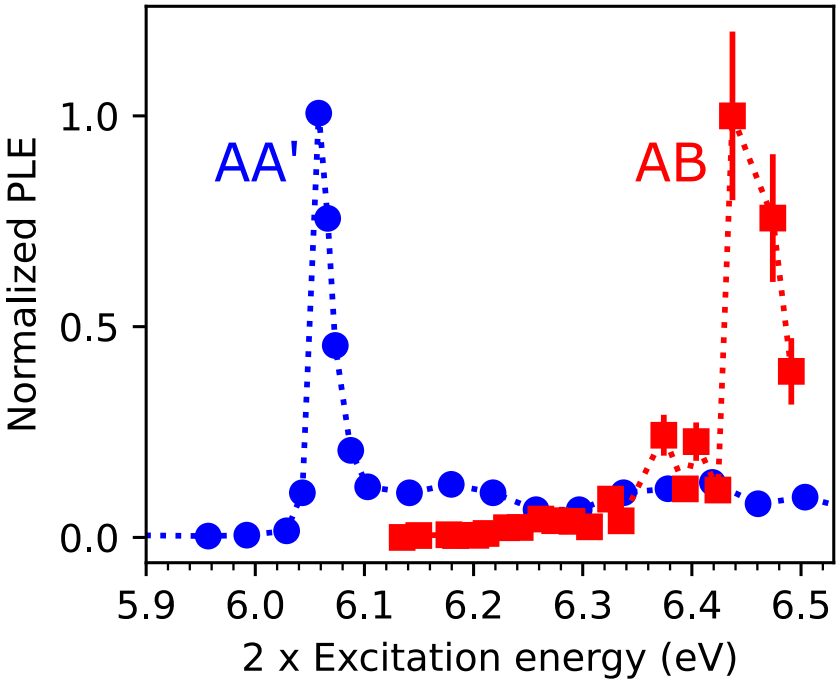

Figure 4.9: Two-photon PL excitation spectroscopy detected either on AB-hBN (red symbols) at the emission energy of ∼6.04 eV or on AA'-hBN (blue symbols) at the emission energy of ∼5.8 eV.

up as a good technique for studying the optical response of AB-hBN.

Fig.4.9 shows the two-photon PLE spectra measured either on the AA'-hBN crystal [blue circles] or the AB-hBN crystal [red squares]. For AA'-hBN, the PLE spectrum represents the intensity of the PL signal detected at ∼5.8 eV, corresponding to the TO replica of the indirect bandgap emission of AA'-hBN, for two-photon excitation energies going from 5.95 to 6.5 eV. For AB-hBN, the PLE spectrum shows the intensity of the PL signal detected at ∼6.04 eV for two-photon excitation energies going from 6.1 to 6.5 eV. Because the PLE is detected at higher energy in AB-hBN than in AA'-hBN, excitation energies below 6.1 eV are beyond reach in AB-hBN. The excitation range is further limited because of the presence of the strong SHG signal (10^4 larger than the PL for 2ω ∼3.05 eV) in AB-hBN thus preventing PLE measurements near the ∼6.04 eV resonance. Consequently, the comparison between the two PLE spectra below 6.1 eV is not possible. However, different behaviors are observed on the high-energy parts of the PLE spectra of AA'-hBN and AB-hBN. While the PLE spectrum of AA'-hBN is almost constant above 6.1 eV, two-photon excitation becomes more and more efficient in AB-hBN when increasing the energy with a first plateau after ∼6.35 eV followed by an increase up to a factor of ∼10 at ∼6.45 eV.

The different PLE spectra measured on the AA' and AB crystals rule out the existence of small AB-hBN inclusions inside a AA'-hBN matrix. Indeed, this configuration would lead to a PLE spectrum similar to AA'-hBN as commonly observed for the emission from extended defects [98]. This is due to the dominating absorption, characterized by stronger oscillator strengths, of the main hBN matrix compared to the small inclusions, then ruling the PLE spectrum of the overall crystal. The observation of a different PLE spectrum in the B region demonstrates that we are dealing with a coherent bulk AB-hBN crystal.

The limited excitation range used in the PLE spectrum of AB-hBN makes the attribution of the different plateaus difficult. However, one could tentatively assign the strong increase at ∼6.45 eV to the continuum bandgap while the plateau at lower energy could correspond to the excited states of the direct exciton in AB-hBN, the fundamental state of which probably lying near 6.04 eV being beyond reach for the reasons mentioned above. This would then imply a binding energy of ∼400 meV on the order of what is predicted by *Sponza et al.* from first-principle calculations for AB-hBN [32]. However, further investigations are required to precisely measure the binding energy of the direct exciton in AB-hBN. Besides, the nature and the value of the optical bandgap of AB-hBN can be retrieved from its PL spectrum in the deep-UV as will be shown next.

4.3 Optical properties of AB-hBN

In the last section, I demonstrated for the first time the isolation of a pure bulk AB-hBN crystal via the combination of SHG and PL microscopies in the deep-UV. In this part, I will present an in-depth study of the optical properties of AB-hBN from the previously isolated crystal using our deep-UV microscope. In Section 4.3.1, I demonstrate the simultaneous direct and indirect emissions in the deep-UV of AB-hBN which is attributed to the quasi-degeneracy of its fundamental direct and indirect excitons in accordance with the calculations of *Sponza et al.* [32]. In Section 4.3.3, I investigate the thermal broadening of the direct and indirect transitions in AB-hBN which present very different behaviors. A physical model involving light-matter coupling is then proposed to explain this difference. Finally, in Section 4.3.4, I evidence the effect of stacking on the deep-level emission of hBN in the UVB.

4.3.1 Direct and indirect bandgap emission

Fig.4.10 shows the normalized PL spectra of AB-hBN [red curve, AB] and AA'-hBN [blue curve, AA'] at ∼6 K in the region 5.7-6.1 eV measured with our deep-UV microscope using an excitation energy of 6.39 eV(194 nm). The "AA'" spectrum, recorded on a high-quality AA'-hBN crystal (see Section 4.2.1), corresponds to the indirect bandgap emission of AA'-hBN, as described in Section 1.2.4. The four main peaks at 5.77 eV, 5.8 eV, 5.86 eV and 5.89 eV are the LO_3, TO, LA and TA phonon replicas, respectively. The "AB" spectrum, recorded on the AB-hBN crystal of Section 4.2.2, consists of a narrow peak (∼10 meV linewidth) at ∼6.038 eV

previously identified as the optical signature of AB-hBN, and of a series of peaks below 6 eV never reported before.

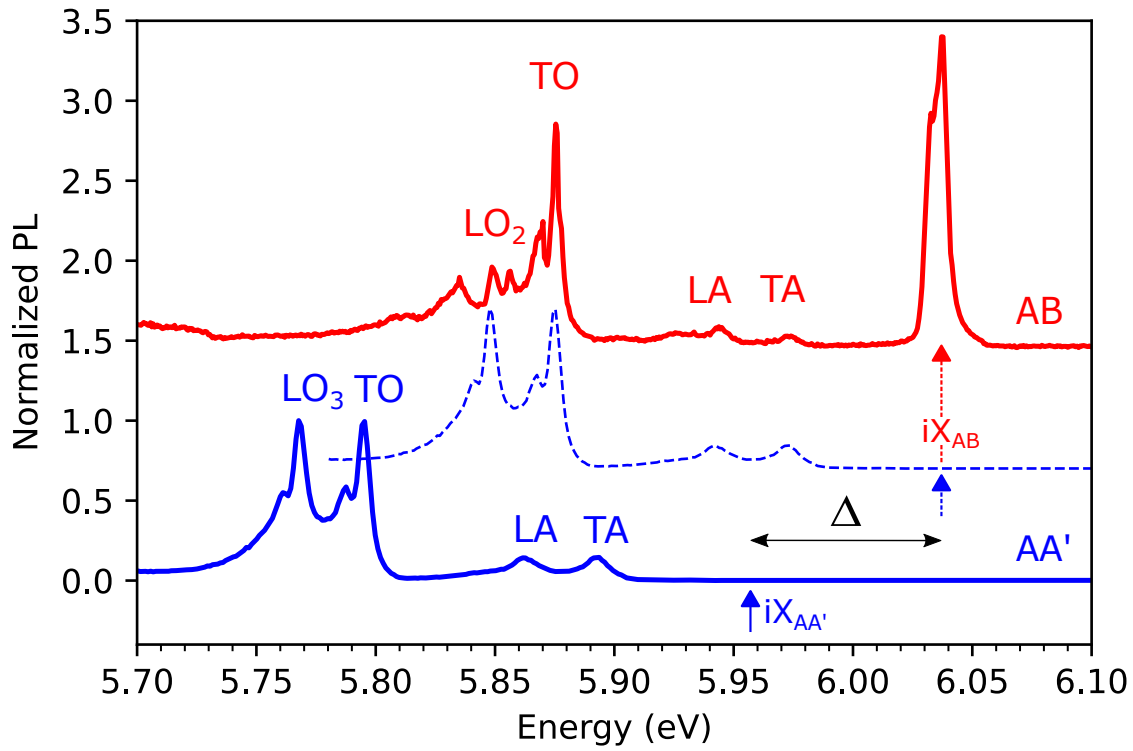

Figure 4.10: Normalized PL spectra of AB-hBN [red curve, AB] and AA'-hBN [blue curve, AA'] at ∼6 K in the region 5.7-6.1 eV measured by deep-UV microscopy. Laser excitation energy = 6.39 eV(194 nm). The dashed blue line represents the 80 meV blue-shifted AA' spectrum. Δ =80 meV.

Interestingly, the emission below 6 eV in AB-hBN is very similar to AA'-hBN as illustrated by the 80 meV blue-shifted "AA'" spectrum [blue dashed line] on Fig.4.10. We observe a one-to-one correspondence in the region 5.86-6 eV between "AB" and "AA'" where the PL lines at 5.87 eV, 5.94 eV and 5.97 eV [labeled in red TO, LA and TA on Fig.4.10] in "AB" show the same profile and energy as the TO, LA and TA replicas of the shifted "AA'" spectrum. The emission profile of the LA, TA and TO peaks in "AB" is identical to the one of the indirect bandgap emission in AA'-hBN with a sharp Boltzmannian slope on the high-energy side and a long low-energy tail induced by the 6 meV phonon overtones where the first overtone can be resolved in TO (see Section1.2.4) [7, 73, 99]. Moreover, the LA/TA replicas are one order of magnitude weaker than the TO one as in AA'-hBN. However, to the LO_3 replica in "AA'" corresponds a ∼5.850 eV/∼5.856 eV doublet, that is 8 meV blue-shifted compared to the shifted "AA'" spectrum. Remarkably, a similar 8 meV blue-shift is found between the LO_3 and LO_2 phonon modes at the T point of the Brillouin zone (BZ) in both AA'-hBN and AB-hBN [59, 100]. This suggests that the LO_3 replica in AA' is replaced by the LO_2 replica at ∼5.856 eV in AB while the peak

at ∼5.850 eV corresponds to the first phonon overtone. It should be recalled that the LO_2 and LO_3 phonon modes have the same symmetry at the T point whatever the stacking order, thus resulting in similar selection rules (see Section 1.2.2). Consequently, both LO_2 and LO_3-assisted transitions are expected to be allowed in AA'-hBN and AB-hBN for in-plane polarized photons, and the stacking should not have any effect on the selection rules. The observation of only the LO_3 replica in AA'-hBN may be attributed to the higher oscillator strength of the LO_3 transition compared to the LO_2 transition in AA'-hBN. In contrast, the observation of only the LO_2 replica in AB-hBN may come from a stronger LO_2-assisted transition compared to LO_3. This suggests the impact of the stacking on the relative strength of the phonon-assisted transitions in hBN. Accordingly, the PL signal from 5.84 to 6 eV in AB-hBN is attributed to the indirect bandgap emission of AB-hBN where the peaks at 5.85 eV, 5.87 eV, 5.94 eV and 5.97 eV correspond to the LO_2, TO, LA and TA replicas.

The energy of the indirect exciton in AB-hBN (iX_{AB}) is then extracted from the series of phonon replicas by adding the energy of the corresponding phonon involved in the phonon-assisted recombination process. iX_{AB} is found at 6.038 eV which is 80 meV blue-shifted compared to $iX_{AA'}$, as shown by the arrows on Fig.4.10. Surprisingly, iX_{AB} falls exactly at the position of the high energy peak of AB-hBN. However, because of its indirect nature, direct emission from iX_{AB} is forbidden by momentum conservation. In particular, as for $iX_{AA'}$, iX_{AB} is located at the T point of the BZ, following the same arguments as for AA'-hBN (see Section 1.2.4). Therefore, iX_{AB}, which is at the origin of the indirect bandgap emission of AB-hBN below 6 eV, can not be involved in the emission at 6.038 eV. The narrow lorentzian line at 6.038 eV stems from the direct exciton in AB-hBN (dX_{AB}). Besides, the attribution to defects is discarded since it should lie below the lowest lying exciton iX_{AB}. Finally, the peak at 5.835 eV is attributed to a phonon replica of the peak at 6.038 eV involving the emission of LO_3 phonons in Γ (see Fig.1.10). We thus conclude that simultaneous direct and indirect emissions occur in AB-hBN.

Fig.4.11 shows the excitonic dispersion of the fundamental exciton of AA'-hBN [blue points/line - AA' label] and AB-hBN [red points/line - AB label] calculated by *Sponza et al.* [32] and extracted from Fig.1.13. The direct excitons (dX), represented by the squares in Fig.4.11(a), lie inside the light cone corresponding globally to the Γ valley. Outside the light cone, the excitons are indirect [circles in Fig.4.11(a)] and the fundamental indirect excitonic states (iX), represented by the large circles in Fig.4.11(a)], are located around the T point of the BZ. As seen in Section 1.2.4, $iX_{AA'}$ is both estimated and measured ∼120 meV below $dX_{AA'}$ resulting in a purely indirect emission in AA'-hBN. Furthermore, calculations predict a blue-shift on the order of ∼120 meV and ∼10 meV for iX_{AB} and dX_{AB}, respectively. Therefore, the energy splitting dX-iX of ∼120 meV in AA'-hBN decreases to only ∼10 meV in AB-hBN resulting in quasi-degenerate optical bandgap where iX_{AB} lies at almost the same energy as dX_{AB}, thus explaining the simultaneous observation of direct and indirect bandgap emission in AB-hBN.

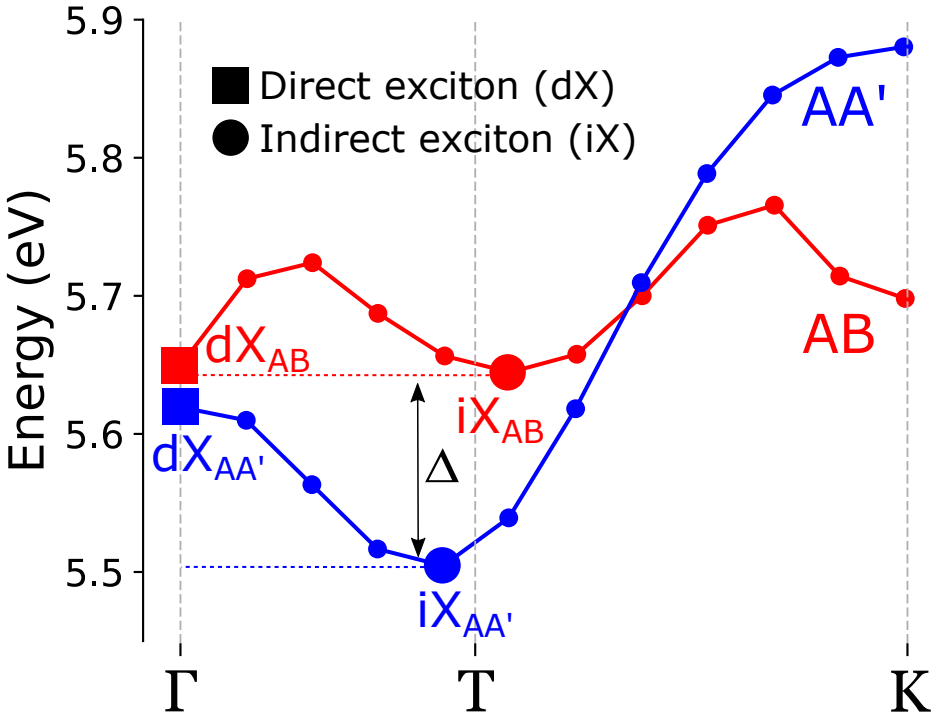

Figure 4.11: Excitonic dispersion of the fundamental exciton of AA'-hBN [blue points/line - AA' label] and AB-hBN [red points/line - AB label] calculated by *Sponza et al.* [32].

Whereas we could reach a precise estimation of the iX_{AB} energy at 6.038 eV, evaluating the energy of dX_{AB} is more difficult due to the so-called polariton effect in bulk semiconductors resulting in a direct emission at lower energy than dX_{AB}. Consequently, the 6.038 eV emission line thus provides only a lower bound for the energy of dX_{AB}. In the next section, I will introduce the polariton effect, arising from the strong light-matter coupling with excitons in bulk semiconductors, applied to the case of AB-hBN. Our model explains how the polariton effect induces a red-shift of the direct emission compared to the energy of dX_{AB} and how the energy of dX_{AB} could be estimated from future reflectivity measurements.

4.3.2 The polariton effect in AB-hBN

Due to the three-dimensional (3D) translational invariance, direct excitons in bulk crystals strongly couple to light leading to the formation of mixed exciton-photon eigenstates, the so-called exciton-polaritons [66, 101]. In Section 4.2.2, we saw the bulk nature of our AB-hBN crystal, with a thickness of 200 nm. Accordingly, direct excitons in AB-hBN are subject to the strong light-matter coupling characterized by an anti-crossing between the excitonic dispersion [red dashed curve in Fig.4.12] and the light cone [blue dashed curve in Fig.4.12] in the crystal resulting in the upper-polariton (UP) and lower-polariton (LP) branches [green solid curves on Fig.4.12 labeled UP and LP, respectively]. Since indirect excitons do not couple to light, the LP branch away from the light cone is exciton-like. However, when approaching the light cone, the

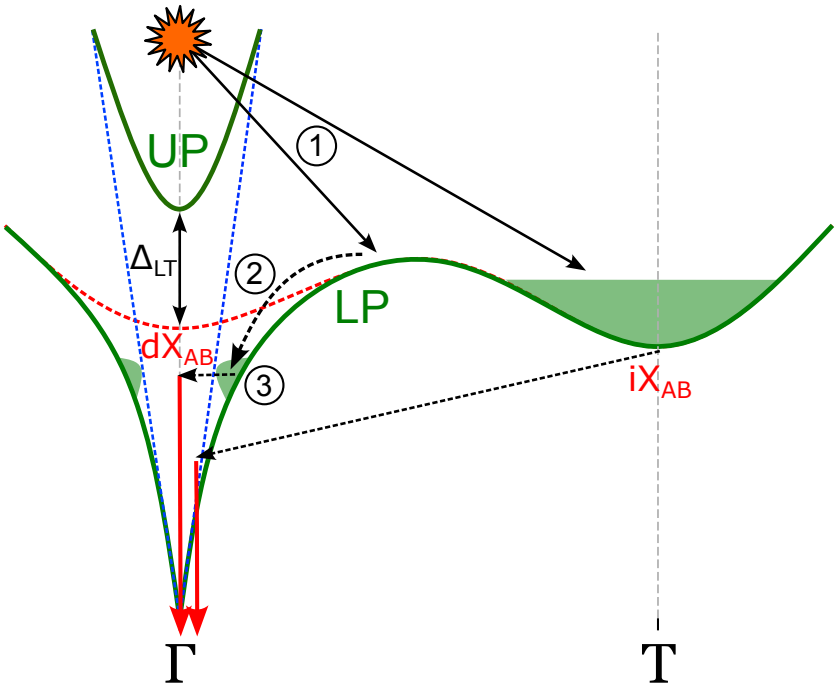

Figure 4.12: Scheme of the polariton dispersion in AB-hBN (green lines), featuring the UP branch and the LP branch, as well as the excitonic (red dotted line) and photonic (blue dashed lines) dispersions. The thermalized polariton population is represented by the green shaded areas. The black dotted (red solid) arrows represent the phonon (photon) emissions occurring in phonon-assisted radiative recombination processes of polaritons at dX_{AB} and iX_{AB}.

hybridization of excitons with photon states induces a large curvature of the LP branch, thus becoming photon-like. Correspondingly, the UP branch is a parabola inside the light cone, which is photon-like except for the minima in Γ because of the hybridization with the excitonic states. Notably, the polariton effect induces a blue-shift of the UP branch minimum with respect to dX_{AB}, namely the transverse-longitudinal splitting (Δ_{LT}), which is directly proportional to the oscillator strength of dX_{AB}. In the region of the splitting, the light cannot propagate through the crystal resulting in the so-called reststrahlen band in the reflectivity spectrum. Therefore, the reststrahlen band provides a direct way to measure Δ_{LT} from reflectivity measurements and has been used to estimate the energy of $dX_{AA'}$ (see Section 1.2.4) [54]. Because of the microscopic lateral dimensions of our AB-hBN crystal, we could not perform such reflectivity measurements in the deep-UV for dX_{AB}. Another important consequence of the polariton effect is the red-shift of the direct emission compared to dX_{AB} arising from the fact that exciton-polariton are eigenstates of the system (crystal+light) which do not intrinsically recombine through direct radiative recombinations as it will be shown next.

Following the exciton-polariton picture, the optical excitation generates a plasma of free electron-hole pairs in the energy continuum [orange star in Fig.4.12] which quickly relax into the LP branch, possibly via Auger or phonon-assisted processes, by forming bound exciton-polaritons

[black solid arrow (1) in Fig.4.12]. The hot polaritons in the LP branch then thermalize either to the energy minimum at iX_{AB} or toward the light cone through emission cascades of acoustic phonons. However, the rapidly increasing curvature of the LP branch at the vicinity of the light cone induces a drastic reduction of the density of final states for the cascading process involving quasielastic acoustic phonons at low $|\vec{k}|$ until the point where the group velocity of the dispersion is higher than the one of acoustic phonons, the so-called LP bottleneck, setting the end of the polaritons relaxation [black dashed arrow (2) in Fig.4.12]. In the case of a perfect 3D crystal, the LP population would never recombine as polaritons are the system (crystal+light) eigenstates. However, in the real case of a finite crystal, the population in the LP bottleneck may relax radiatively through quasi-elastic scattering processes because of the translational symmetry breaking induced by the crystal edges [black dashed arrow (3) in Fig.4.12]. As a result, the energy of the emitted light is red-shifted compared to dX_{AB}. This suggests that the direct bandgap emission peak at ∼6.038 eV in AB-hBN only corresponds to the energy of the LP bottleneck, and not to dX_{AB} which is expected at higher energy. Since there is no estimation of the value of Δ_{LT} for dX_{AB}, it is impossible at this stage to determine the exact energy of dX_{AB}. Incidentally, the optical bandgap of AB-hBN is marginally indirect lying at 6.038 eV, and the indirect emission is not affected by the polariton effect.

In this section, I showed how the light-matter coupling could induce a red-shift of the direct emission in AB-hBN. In the next section, I will evidence the effect of the light-matter coupling on the thermal broadening of the direct emission in AB-hBN from temperature-dependent PL spectroscopy. In particular, while direct and indirect emissions are simultaneously observed in AB-hBN, their thermal broadening are drastically different. I then attribute this contrast of broadening to the strong light-matter coupling inducing a weaker phonon dephasing for the direct emission than for the indirect one.

4.3.3 Thermal broadening

The PL spectra in the range 5.75-6.1 eV have been recorded in the AB-hBN crystal for temperatures from 10 to 240 K using an excitation energy of 6.39 eV(194 nm). Above 240 K, the PL signal becomes too weak to be studied. Fig.4.13 shows the PL spectra obtained at 10, 50, 70, 90 and 150 K in the spectral region 5.75-6.1 eV [panel (a)] and zoomed in the region 6-6.1 eV [panel (b)]. Above 6 eV, the direct bandgap emission red-shifts with the temperature from ∼6.04 (10 K) to ∼6.02 eV (240 K), together with a decrease in intensity by factor of 20 and a broadening above 50 K. Interestingly, while a single lorentzian peak at 6.04 eV is observed at 10 K, we note the existence of a weaker peak at higher energy (12-14 meV above) above 50 K which follows the red-shift of the first peak. Despite the general intensity decrease of the two peaks, the intensity ratio between the higher and lower energy peaks increases with the temperature up to ∼50 % at 150 K suggesting the thermal activation of a higher energy level. Therefore, the direct bandgap emission of AB-hBN has been fitted using the sum of two Lorentzian functions of the same width Γ_d and of amplitudes $\mathcal{A}_j$:

$$I(E) = \sum_{j=1}^{2} \mathcal{A}_j \mathcal{L}_j(E) \tag{4.2}$$

with E the energy of the emitted photon and where $\mathcal{L}_j$ is a normalized Lorentzian function :

$$\mathcal{L}_j(E) = \frac{\Gamma_d}{2\pi} \cdot \frac{1}{(\frac{\Gamma_d}{2})^2 + (E - \Omega_j)^2} \tag{4.3}$$

The parameters ($\mathcal{A}_{1,2}$, $\Omega_{1,2}$, Γ_d) have been adjusted for each temperature to fit our experimental data. The results of the fits are shown by the dotted lines in Fig.4.13(b).

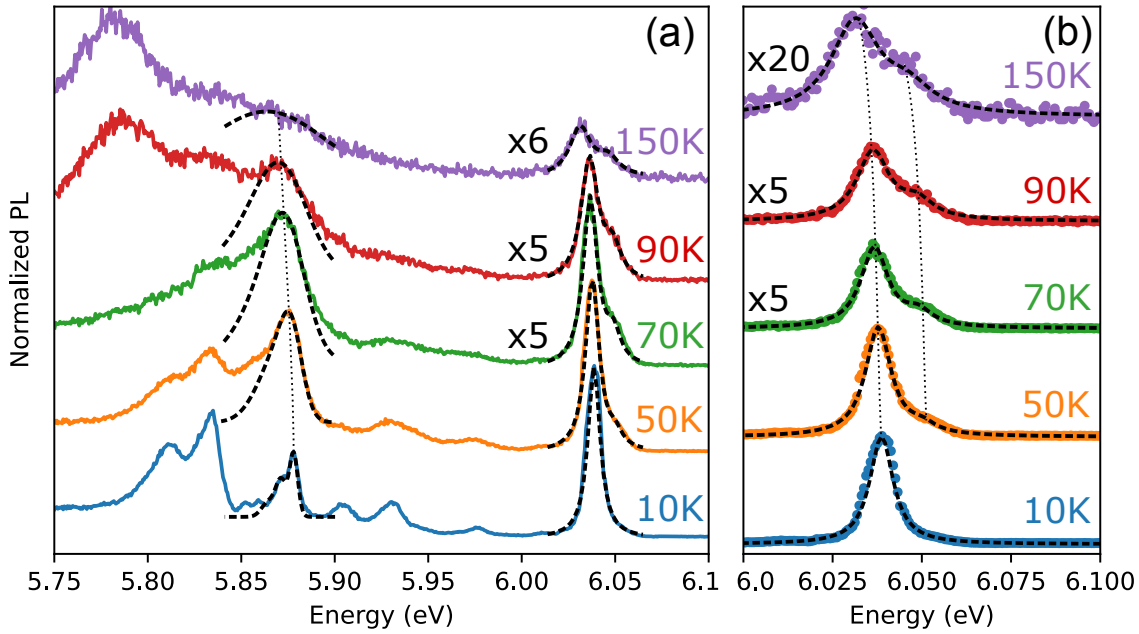

Figure 4.13: PL spectra recorded in the AB-hBN crystal (Section 4.2.2) using an excitation energy of 6.39 eV(194 nm) at 10, 50, 70, 90 and 150 K in the spectral region 5.75-6.1 eV [panel (a)] and zoomed in the region 6-6.1 eV [panel (b)].

Below 6 eV, indirect bandgap emission of both AB-hBN and AA'-hBN (see Section 4.3.2) are observed suggesting the coexistence of the two phases at the position where the PL spectra have been recorded. The peaks at 5.82 eV, 5.84 eV, 5.90 eV, 5.93 eV correspond to the LO_3, TO, LA and TA replicas of AA'-hBN while the peaks at 5.85 eV, 5.87 eV and 5.97 eV correspond to the LO_2, TO and TA replica of AB-hBN. We observe a thermal broadening of the lines below 6 eV much more pronounced than for the emission above 6 eV. The overall intensity decreases by a factor of 6 at 240 K while the intensity of the TO replica of AB-hBN at 5.87 eV first increases between 10 and 50 K. Since the TO replica at 5.87 eV is the most intense of the phonon replicas of AB-hBN (see Section 4.3.1), we use it to quantify the thermal broadening of the indirect bandgap emission in AB-hBN, following the cumulative Gaussian broadening

procedure described in Ref. [73]. First, the spectral profile of the phonon-assisted emission is given by the distribution function $\mathcal{F}$ defined in [7] :

$$\mathcal{F}(E)_n^{TO} = \rho(E - \delta_{TO,n}) f(E - \delta_{TO,n}) e^{-\frac{E-\delta_{TO,n}}{k_B T}} \tag{4.4}$$

with E the energy of the emitted photon and $\delta_{TO,n} = E_{iX_{AB}} + E_{TO} + nE_{LO_1}$ (E_{LO_1} =6 meV and E_{TO} =162 meV).

$$\rho(x) = \theta(x) \left(\frac{2M_n}{\hbar^2}\right)^{\frac{3}{2}} \sqrt{x} \tag{4.5}$$

represents the joint density of state with $\theta(x)$ the step function and $M_n = 1.7m_0$ the effective mass of iX_{AB} [102],

$$f(x) = \frac{1}{\left(4 + a^2 \left(k_T + \frac{x}{v_g^{TO}}\right)^2\right)^4} \tag{4.6}$$

is the matrix element of the electron-phonon interaction with $k_T = 0.8710^{-10} m^{-1}$ the wavevector in T, a =3 Å is the exciton Bohr radius and v_g^{TO} ($= 0.1810^4 m.s^{-1}$) the group velocity of the phonon at the T point. Therefore, the TO replica is fitted by the sum of the convolution of the spectral profile $\mathcal{F}$ with a Gaussian function, up to n=3, of amplitudes B_n :

$$I(E) = \sum_{n=0}^{3} B_n \mathcal{F}(E)_n^{TO} \bigotimes \mathcal{G}_n(E) \tag{4.7}$$

with $\mathcal{G}_n(E)$ a normalized Gaussian function :

$$\mathcal{G}_n(E) = \frac{1}{\Gamma_i^n \sqrt{2\pi}} exp\left(-\frac{E^2}{2(\Gamma_i^n)^2}\right) \tag{4.8}$$

where $\Gamma_i^n = \Gamma_i(1+n)$ is the width of the overtone of order n while Γ_i is the width of the indirect emission [73]. The results of the fits of the TO replica for each temperature are represented in Fig.4.14 by the black dotted lines below 6 eV. Noticeably, the thermal broadening of the indirect bandgap emission becomes rapidly much larger than the complex structure of the TO replica thus replaced by a Gaussian profile above 50 K as already observed in AA'-hBN [7, 99].

The temperature variations of Ω_1 [blue circles] and E_{iX} [orange squares] are displayed in Fig.4.14(a). Both energies display a thermal red-shift of ∼20 meV, from 6.04 (10 K) to 6.02 eV (240 K), similar to what was previously observed in AA'-hBN [103]. Moreover, the coincidence in energy between Ω_1 and E_{iX}, within the fit error, suggests a similar temperature dependence for dX_{AB} and iX_{AB}. We thus attribute this thermal red-shift to the temperature dependence of the optical bandgap of AB-hBN.

Fig.4.14(b) shows the energy splitting $\Delta\Omega = \Omega_2 - \Omega_1$ as a function of temperature. The energy splitting $\Delta\Omega$, of about ∼14 meV, is approximately constant with temperature within the

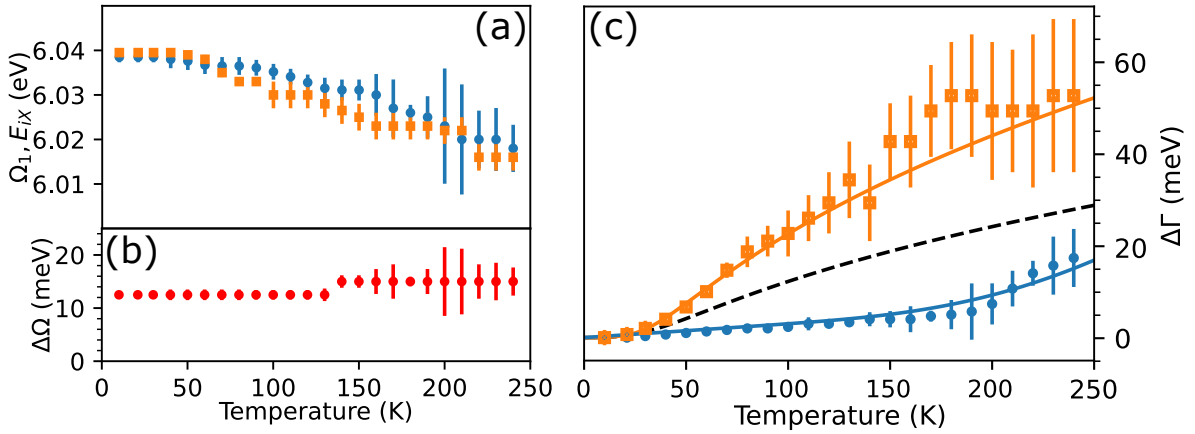

Figure 4.14: Temperature variations of (a) the energies Ω_1 (blue circles) and E_{iX} (orange squares), (b) the energy splitting $\Delta\Omega = \Omega_2 - \Omega_1$ and (c) the thermal broadening $\Delta\Gamma(T) = \Gamma_\alpha(T)$-$\Gamma_\alpha(10K)$ where α =i (orange squares), d (blue circles). The dashed line in (c) represents the thermal broadening of the indirect bandgap emission in AA'-hBN, from Ref. [99].

fit error. The discontinuity observed at ∼130 K could be due to a spatial drift of the sample when changing the temperature. Therefore, both components of the direct emission above 6 eV show the same temperature dependence. Since the high-energy component of the PL spectrum centered at Ω_2 is more and more intense when raising the temperature [Fig.4.13(b)], the ratio $\mathcal{A}_2/\mathcal{A}_1$ increases with temperature, suggesting a thermal activation. We found that $\mathcal{A}_2/\mathcal{A}_1$ follows a Boltzmann law $exp(\frac{-E_0}{k_B T})$, where E_0 is on the order of the energy splitting $\Omega_2 - \Omega_1$ between the two Lorentzian functions. More precisely, the best fit to the experimental data is obtained by taking, for E_0, the energy splitting $\Omega_2 - \Omega_1$, but with a small correction of −2 meV. Therefore, the existence of two peaks in the direct bandgap emission of AB-hBN could originate from a two-component distribution of thermalized exciton-polaritons at the LP bottleneck. At this stage, we have no clear interpretation of the origin of these two peaks, which will require further investigation.

Finally, Fig.4.14 shows the variations of the broadening with respect to 10 K [$\Delta\Gamma_\alpha(T) = \Gamma_\alpha(T)$-$\Gamma_\alpha(10K)$ where $\alpha = i, d$] for the direct [blue circles] and indirect [orange squares] transition in AB-hBN. The thermal broadening of the indirect bandgap emission in AA'-hBN [black dashed line in Fig.4.14], adapted from Ref. [99], is shown for the sake of comparison. Very different are the thermal broadenings of the direct and indirect transitions in AB-hBN. For the indirect bandgap emission, the thermal broadening reaches values as high as ∼20 meV at 100 K with a slower increase to ∼50 meV at 240 K. Moreover, $\Delta\Gamma_i(T)$ shows the same unusual curvature as for AA'-hBN [dashed line in Fig.4.14]. In contrast, much smaller is $\Delta\Gamma_d(T)$, only reaching ∼20 meV at 240 K. Moreover, it shows the usual curvature corresponding to the standard phenomenology in most of the semiconductors.

The unusual curvature of $\Delta\Gamma_i(T)$ stems from the so-called slow modulation limit of the

phonon-assisted broadening predicted by Toyozawa in his seminal paper [104], and first observed in hBN [99]. In the slow modulation limit, each contribution to the phonon-assisted broadening scales like the square root of the phonon occupation number, so that the total phonon dephasing is written as [99] :

$$\Gamma_i(T) - \Gamma_i(0) = \sqrt{\Delta_A^2 + \Delta_O^2} - \sqrt{S_A E_A} \tag{4.9}$$

where Δ_A and Δ_O are the contributions of acoustic and optical phonons, respectively, given by [104] :

$$\Delta_A^2 = S_A E_A coth\left(\frac{E_A}{2k_B T}\right) \tag{4.10}$$

$$\Delta_O^2 = S_O E_O \frac{1}{e^{\frac{E_O}{k_B T}} - 1} \tag{4.11}$$

where E_A and E_O represent the mean energy of the acoustic and optical phonons involved in the dephasing processes, respectively, S_A and S_O are the corresponding coupling strengths, and k_B is the Boltzmann constant. A fair agreement with our data is obtained by taking E_A =4 meV, E_O =15 meV, S_A =4.5 meV, and S_O =200 meV [orange line on Fig.4.14]. The phonon dephasing is in the slow modulation limit in AB-hBN, as in AA'-hBN, because of the weak dispersion of the excitonic band around iX_{AB}, fulfilling Toyozawa's criterion of "flat bands" [104]. Remarkably, an enhancement by a factor ~ 2 is observed in AB-hBN in comparison to AA'-hBN. We interpret this effect as a result of the weaker in-plane excitonic dispersion along $\Gamma - K$ in AB-hBN predicted by *Sponza et al.* (see Fig.4.11) and witnessed by the quasi-degeneracy of dX_{AB} and iX_{AB}.

For the direct bandgap emission, the thermal broadening could not be explained by the slow modulation limit but, on the contrary, by the fast modulation limit for which the linewidth increases linearly with the phonon occupation number $n(T)$. Such a difference comes from the motional narrowing regime of the exciton-phonon interaction that is quasi-universal in semiconductor physics [99, 104, 105] :

$$\Gamma_d(T) - \Gamma_d(0) = \Delta_A + \Delta_O \tag{4.12}$$

where $\Delta_A = aT$ and $\Delta_O = b\frac{1}{e^{\frac{\Lambda}{k_B T}} - 1}$ are the contributions of acoustic and optical phonons, respectively, given by Ref. [105], where a and b characterize the coupling to acoustic and optical phonons, respectively, and Λ is the typical optical phonon energy. An excellent agreement with our data is obtained with $a = 0.03\,\text{meVK}^{-1}$, $b = 600$ meV, and $\Lambda = 90$ meV.

The dramatic modification of the thermal broadening with respect to the indirect bandgap emission originates from the strong light-matter coupling for dX_{AB}. Fig.4.15 gives a schematic representation of the UP and LP branches in AB-hBN both along the in-plane ($k_\parallel$) and out-of-plane ($k_\perp$) directions. In the calculations of phonon dephasing within the Fermi's golden

rule [105], one has to consider the density of polaritonic states, and not the density of excitonic states. Accordingly, the curvature of the polaritonic dispersions near Γ leads to a reduction of the density of final states for the phonon dephasing processes of the direct emission, where the polaritons at the LP bottleneck are quasielastically scattered at high **k** by acoustic phonons, resulting in a reduction of the phonon dephasing efficiency in the fast modulation limit [Eq. 4.12]. In contrast, the flat polaritonic dispersion around the T point leads to a very high density of final states for the phonon dephasing processes of the indirect emission inducing an efficient phonon dephasing in the slow modulation limit [Eq. 4.9]. Therefore, the light-matter interaction, via the modification of the polaritonic dispersion curvature, has a dramatic effect on the phonon dephasing efficiency both qualitatively and quantitatively. First, there is a transition from the slow modulation limit [Eq. 4.9] to the fast one [Eq. 4.12], with different curvatures of the broadening as a function of temperature [Fig.4.14(c)], because Toyozawa's criterion of "flat bands" is no longer fulfilled. Second, there is an overall decrease of the phonon dephasing efficiency, by approximately one order of magnitude below 200 K [Fig.4.14(c)], when quasi-elastic acoustic phonon scattering dominates. Above 200 K, the broadening processes assisted by optical phonons become more and more important. Such scattering mechanisms are no longer quasi-elastic so that they involve other final states than the LP. As a consequence, the thermal broadenings only differ by a factor ∼3 at 240 K.

Although the impact of the light-matter interaction on the phonon dephasing was predicted by calculations [105], we are not aware of any experimental observation of this effect. Our results give the first experimental demonstration of this effect enabled by the simultaneous direct and indirect bandgap emission in AB-hBN which appears as a model system.

While the effect of stacking has been studied so far for the intrinsic optical properties of hBN, it is of particular interest to determine how the stacking affects the deep-level emission in hBN. In the next section, I will present the effect of stacking on the deep-level emission associated to the well-known "4 eV defect" in hBN through the simultaneous inspection of the PL signal in the deep-UV and the UVB spectral range.

4.3.4 Deep levels emission in the UVB

Using our deep-UV microscope, we have recorded in a single hyperspectral acquisition, simultaneously the PL signal in the deep-UV and UVB spectral ranges over a 24x24 µm^2 area of our exfoliated sample shown in Fig.4.7. The acquisition has been performed at 6 K using an excitation energy of 6.39 eV(194 nm). In Fig.4.16, panels (a) and (b) show the PL intensity maps integrated in the spectral range 6.02-6.06 eV and 4.14-4.17 eV, respectively. On both panels, the contour of the sample with the A, B and C regions, extracted from Fig.4.7, is depicted by the white dashed lines. Finally, panel (c) shows the PL spectra in the UVB (3.85 and 4.2 eV) recorded for AB-hBN [red spectrum on Fig.4.16] and AA'-hBN [blue spectrum on Fig.4.16] at the position indicated by the white squares on panels (a) and (b). The shaded region in panel

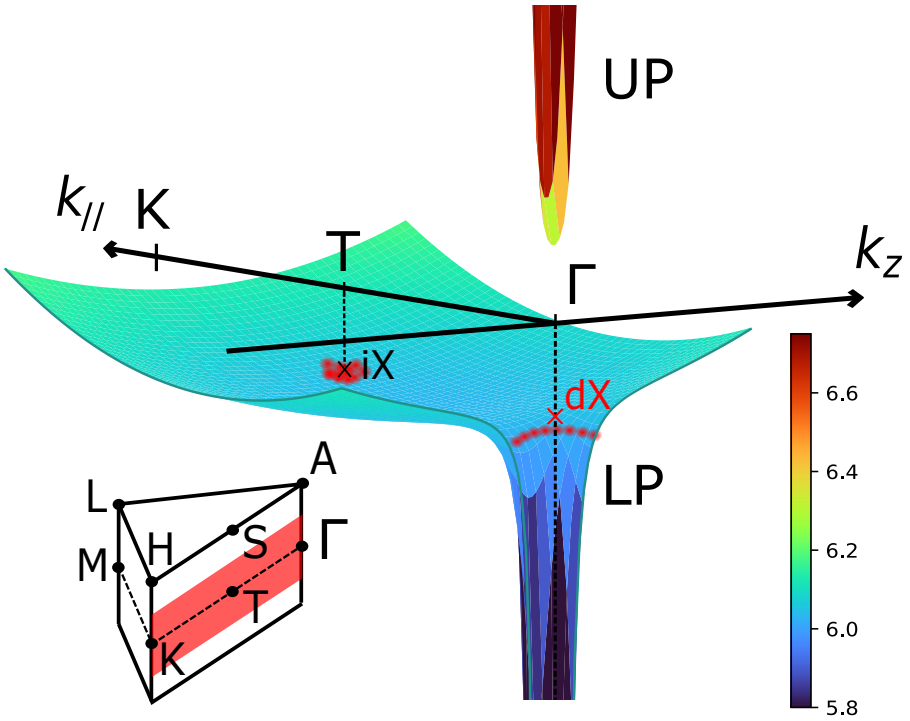

Figure 4.15: Schematic representation of the dispersion of the upper (UP) and lower (LP) polaritons in AB-hBN along the in-plane ($k_{\parallel}$) and out-of-plane ($k_{\perp}$) directions. The red dots indicate the thermalized populations of LP (i) at the minimum of the excitonic dispersion (iX$_{AB}$) around the T point and (ii) at the LP bottleneck around Γ. Inset: irreducible part of the first Brillouin zone, where the red area indicates the landscape of the dispersion plot.

(c) represents the integration range of the PL intensity map in the UVB of panel (b).

Following Section 4.2.2, the peak at ∼6.04 eV can be used as a spectral signature in the deep-UV to evidence the presence of AB-hBN crystals. Therefore, the PL intensity map of panel (a) [Fig.4.16], integrated around the ∼6.04 eV peak, provides the spatial distribution of the AB-stacking order over a larger area in our sample compared to our previous 10x10 µm^2 map of Section 4.2.2. Surprisingly, the signal at ∼6.04 eV is not only observed in the B region, as shown in Section 4.2.2, but also on the edges of the A and C regions. Remarkably, the bright areas in Fig.4.16(a) coincide with the colored (pink/green/yellow) areas in Fig.4.7. Furthermore, the signal at ∼6.04 eV vanishes completely inside the white/grey areas of the A and C regions in Fig.4.7 previously identified as pure AA'-hBN crystal in Section 4.2.2. Accordingly, our larger PL mapping allows us to unravel the presence of AB-hBN crystals over the whole sample which seems to systematically coincide with the colored areas of Fig.4.7 characteristic of thinner layers.

The deep-level emission of the well-known "4eV defect" recorded in AA'-hBN at the position of the white square "AA'" is displayed in Fig.4.16(c). The emission features a sharp line at ∼4.09 eV(∼303 nm), corresponding to the zero-phonon line (ZPL) of the defect, i.e., the direct recombination without any net energy transfer with the phonon bath. The structured emission below the ZPL comes from phonon-assisted recombination in the defect. This vibronic band

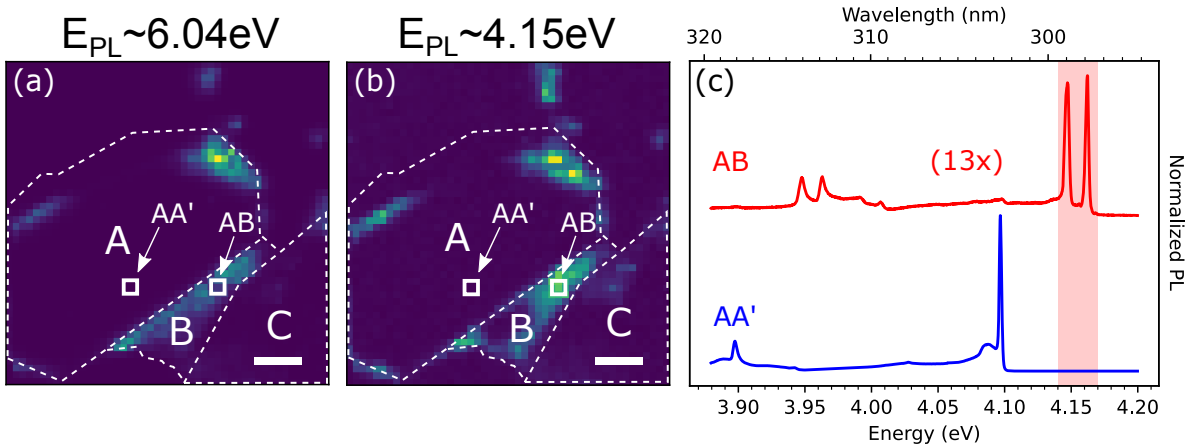

Figure 4.16: (a, b) PL intensity maps integrated in the spectral range 6.02-6.06 eV (a) and 4.14-4.17 eV (b) recorded at 6 K over a 24x24 µm^2 area of our exfoliated sample, shown in Fig.4.7, using an excitation energy of 6.39 eV(194 nm). Scale bar = 4 µm. The sample contour extracted from Fig.4.7 is represented by the white dotted line along with the labeling of the corresponding A, B and C regions. (c) PL spectra in the UVB (3.85 and 4.2 eV) of AB-hBN (in red) and AA'-hBN (in blue) recorded at the position represented by the white squares on panels (a) and (b). The red shaded region represents the integration range used for panel (b).

involves low-energy acoustic phonons, for the emission at ∼4.08 eV close to the ZPL, zone-center optical phonons of 200 meV, for the replica at ∼3.9 eV, and phonons spanning the full band structure as evidenced by phonon-photon mapping [106]. Surprisingly, the deep-level emission recorded in AB-hBN at the position of the white square "AB", displayed in Fig.4.16(c), is duplicated into two identical spectra globally blue-shifted by 55 and 70 meV, respectively, as evidenced by the two ZPL at 4.147 eV and 4.162 eV and their phonon replicas at 3.947 eV and 3.963 eV. Therefore, the vibronic band is almost unaffected by the change of stacking displaying exactly the same 200 meV phonon replicas. However, the ZPL linewidth is broadened from 2 meV in AA' to 4 meV in AB. Because of this broadening, it is difficult to conclude on a possible modification of the low-energy acoustic phonon band not resolved in the AB spectrum. Remarkably, while the overall signal is 13 times weaker in AB, the integrated intensity of the ZPL is only three times higher in AA' compared to AB because of the different linewidth. Moreover, by taking into account the two ZPLs in AB-hBN we obtain a 2:3 ratio between the integrated ZPL intensity of AA' and AB, thus suggesting a similar defect density at the origin of the deep-level emission in both AA'-hBN and AB-hBN crystals.

The PL intensity map in the UVB of Fig.4.16(b) represents the PL signal integrated over the two ZPLs of AB-hBN [red shaded region in Fig.4.16(c)]. We therefore observe an almost one-to-one correspondence between the PL maps in the UVB [Fig.4.16(b)] and in the deep-UV [Fig.4.16(a)] thus demonstrating that the deep-level emission displayed by the AB spectrum coincides with the presence of AB-hBN crystals. Consequently, the PL signal around 4.15 eV appears as another spectral signature of AB-hBN in the UVB.

Remarkably, the 55 and 70 meV blue-shift of the ZPL in the AB spectrum is smaller than the bandgap shift of 80 meV in AB-hBN (see Section 4.3.1). However, this difference in the shifts is far from surprising since the deep levels at the origin of the emission correspond to Wannier-type electronic states built from the combination of the crystal Bloch states from several electronic bands inside a volume $\mathcal{V}^*_{defect} = \frac{(2\pi)^3}{\mathcal{V}_{defect}}$ in the reciprocal space inversely proportional to the defect volume $\mathcal{V}_{defect}$. As a consequence, the deep-level energy is less influenced by the variation of the bandgap since it averages out over all the electronic states of different bands and $\mathbf{k}$ involved in the Wannier decomposition.

More importantly, the two ZPLs in AB-hBN have been observed independently in previous measurements [107], thus ruling out their origin as different levels of the same microscopic defect, but rather suggesting that they come from different atomistic configurations of the "4eV defect". Furthermore, the ~ 2 fold decrease of the integrated intensity of the ZPL from AA' to AB stacking suggests the existence of 2 configurations. In AA', these configurations are likely degenerated so that their emission overlap leading to the two-fold increase of the integrated intensity of the ZPL. In AB, these configurations become non-degenerated thus leading to a splitting of the ZPL along with a two-fold decrease of the integrated intensity. As a matter of fact, AB-hBN consists of nonequivalent layers where either B or N atoms are at the center of the hexagons of the surrounding layers resulting in two distinct lattice sites that are surrounded by different atoms. In contrast, the layers of AA'-hBN are well aligned along the c-axis resulting in similar lattice sites surrounded by the same atoms.

The potential candidates for the "4eV defect" in hBN have been predicted to be the carbon dimer (2C), tetramer (4C), and hexamer (6C) as well as the Stone-Wales (SW) [108, 109]. However, the emission spectra of these 4 defects are found to be fairly similar in AA'-hBN. Nonetheless, recent calculations have computed the emission spectra of these defects for different stackings, including AA' and AB stackings [110]. Interestingly, the spectra of each defect also display a blue-shift between AA' and AB stackings and a duplication of the ZPL in AB. Tab.4.2 summarizes the shift in energy (ΔE) of the lowest lying ZPL between the AA' and AB stacking as well as the ZPL splitting (δ) occurring in the AB stacking extracted from the emission spectra of each defect [110]. We then found the best agreement with our experimental values [Expt. in Tab.4.2] for both 2C and SW defects. Moreover, a strong increase of "4eV defect" emission has been reported in hBN crystals with a high carbon concentration [111]. Accordingly, the "4eV defect" may be tentatively attributed to the 2C defects, although further investigations are required.

In Fig.4.17 I analyze in more details the spatial distribution of the ZPLs in AB-hBN and AA'-hBN by plotting the intensity maps of the PL signal at $\sim$4.1 eV [panel (a)], $\sim$4.15 eV [panel (b)] and $\sim$4.16 eV [panel (c)] where the first one corresponds to the ZPL in AA'-hBN and the

meV	2C	4C	6C	SW	**Expt.**
δ	30	110	180	40	**15**
ΔE	120	130	140	20	**55**

Table 4.2: Table summarizing the energy shift (ΔE) of the lowest lying ZPL between the AA' and AB stacking as well as the ZPL splitting (δ) occurring in the AB stacking extracted from the emission spectra of each potential candidates for the "4eV defect" in hBN (2C, 4C, 6C, SW) [110]. Our experimental values extracted from Fig.4.16(c) are shown (Expt.) for comparison.

two others to AB-hBN. The integration range of each map is represented by the shaded region in the spectrum below, which is spatially integrated over the whole map. The white solid lines in Fig.4.17 outline the AA'-hBN domains corresponding to the grey/white areas in Fig.4.7.

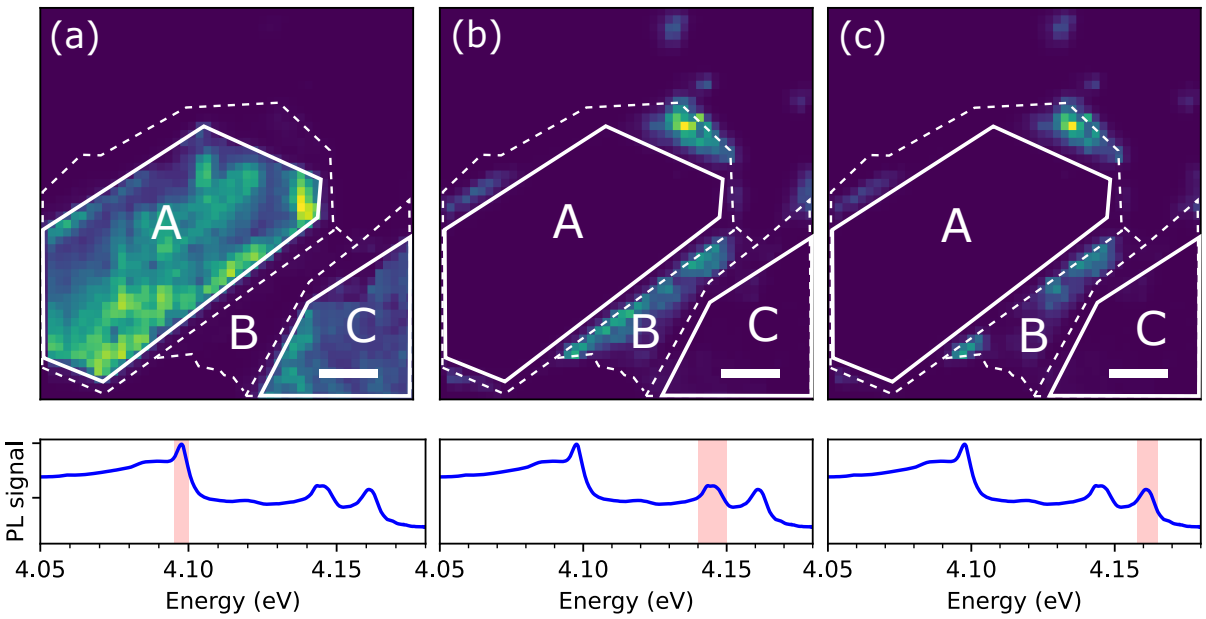

Figure 4.17: Maps of the PL signal in the spectral domain indicated by the shaded area in the PL spectra plotted below: (a) around ∼4.09 eV, (b) around ∼4.15 eV, and (c) around ∼4.16 eV. The white dashed lines show the sample contour as in Fig.4.16 whereas the white solid lines outline the AA'-hBN crystals corresponding to the white areas in Fig.4.7. Scale bar = 4 µm.

In panel (a), the ZPL intensity [Fig.4.17(a)] is observed only inside the areas delimitated by the white dashed lines corresponding to AA'-hBN domains. Drastically different, the intensity maps of Fig.4.17(b,c) are anti-correlated with the first one and the intensity of the ZPLs at ∼4.15 eV and ∼4.16 eV vanishes completely inside the AA'-hBN domains while it is observed at the position of the AB-hBN crystals identified in Fig.4.16(a). The two maps of panels (b) and (c) are almost identical with an intensity ratio of nearly 1 thus indicating the

quasi-equal distribution of the atomistic configurations of the defect at the origin of the two ZPLs in AB-hBN. However, a tiny difference between the two maps is observed at the left edge of the AB region where the ZPL at 4.162 eV decreases by a factor of ∼10 compared to the one at 4.147 eV. This independent variation of the two ZPLs in AB-hBN, previously reported by *Pelini et al.*, is consistent with the existence of two inequivalent atomistic configurations of the defect in AB-hBN. This could be due to the preferential formation of one of the two atomistic configurations possibly induced by the presence of local strains caused by the crystal boundaries.

Our results regarding the impact of stacking on the deep-level emission bring important insight toward the determination of the atomic structure, yet undetermined, of the "4.1eV defect" in hBN which should fuel future theoretical investigations. Importantly, we point out the importance of including the hBN stacking in the calculations of the electronic and optical properties of this defect. Furthermore, while the existence of polytypism is an important question in the context of the epitaxial growth of hBN layers, the identification of hBN polytypes requires advanced structural characterization like Raman spectroscopy, x-ray diffraction or TEM (see Section 4.1). The identification of hBN polytypes using these techniques can be ambiguous or demanding in terms of experimental configuration. In the previous part, I have demonstrated the identification of AB-hBN using the direct emission peak at ∼6.04 eV as its spectral signature in the deep-UV, free from any parasitic signal from other hBN polytypes. However, while this specific signature of AB-hBN in the deep-UV could be used as a direct optical technique to evidence the presence of AB-hBN in hBN layers, optical spectroscopy in the deep-UV is far from a routine method and is not easily accessible by crystal growers. In this section we thus demonstrate another specific signature in the UVB from the deep-level emission of AB-hBN which can be used as an alternative to identify the presence of AB-hBN, opening a way for an easier investigation. The PL of this deep level can be excited by the third harmonic of a Ti:Sa laser or by standard 266 nm lasers based on nonlinear generation from a YAG laser. Furthermore, detection of the PL signal at ∼300 nm is simpler than at ∼200 nm because optical spectroscopy in the UV-B is much less constrained than in the UV-C. We thus expect the "4.1eV defect" emission to become a probe of the stacking order in hBN polytypes.

4.4 Conclusion

This chapter is focused on the optical properties of AB-hBN. In Section 4.2, I have demonstrated the first isolation of a micrometer-sized AB-hBN crystal intercalated between two larger AA'-hBN crystals. The identification of the AB stacking has been made from the combination of PL and SHG microscopy recorded over the same area of the crystal where the SHG spatially coincides with the PL signal at ∼6.04 eV. On the one hand, recent theoretical calculations predict a blue-shift of the optical bandgap in AB-hBN compared to AA'-hBN [32]. On the other hand, the observation of SHG is the signature of a non-centrosymmetric polytype like AB-hBN. This lead me to the conclusion that the isolated crystal corresponds to AB-hBN, from which the PL signal at ∼6.04 eV is a specific signature in the deep-UV emission spectrum.

In Section 4.3, I benefited from the isolation of a pure AB-hBN crystal to study its optical properties both in the deep-UV and UVB spectral ranges. In the deep-UV, I evidenced the simultaneous observation of direct and indirect emissions in AB-hBN. The lines between 5.7 and 6 eV are attributed to the phonon-assisted radiative recombination of the indirect exciton in AB-hBN (iX_{AB}), estimated at ∼6.04 eV. Besides, the narrow line at ∼6.04 eV, although overlapping with iX_{AB}, is rather attributed to the radiative recombination of the direct exciton in AB-hBN (dX_{AB}). These results are in agreement with *ab-initio* calculations of the excitonic dispersion in AB-hBN which predict a quasi-degeneracy of iX_{AB} and dX_{AB} [32]. We then studied the thermal broadening of the direct and indirect transitions in AB-hBN which present different behaviors. The thermal broadening of the indirect exciton presents a curvature similar to the one of AA'-hBN, characteristics of the slow modulation limit associated to efficient phonon dephasing processes early described in the seminal work of *Toyozawa* [104]. In contrast, the thermal broadening of the direct transition shows the standard curvature of the fast modulation limit of the phonon dephasing processes usually observed in semiconductors [105]. These different behaviors are interpreted by the influence of the strong light-matter coupling, modifying the curvature of the polariton dispersion near the light cone, thus preventing any efficient phonon-assisted dephasing processes of the direct transition. Our results provide the first experimental demonstration of the detrimental effect of the light-matter coupling on the phonon dephasing at the origin of the thermal broadening. Finally, I demonstrated the impact of stacking on the deep-level emission in the UVB of the "4.1eV defect" in hBN which is duplicated and globally blue-shifted in AB-hBN. The blue-shift of the deep-level emission is linked to the blue-shift of the bandgap of AB-hBN, although attenuated due to the Bloch states mixing in the electronic states of the defect. Besides, I suggested the existence of two atomistic configurations of the defect which would be equivalent in AA'-hBN and become inequivalent in AB-hBN leading to a duplication of the deep-level emission. Therefore, the ZPLs in AB-hBN can be used as a specific signature in the UVB range allowing easier optical characterization compared to the deep-UV. Moreover, our work paves the way to the determination of the atomic structure of the "4.1eV defect" in hBN.

Finally, AB-hBN shows up as a promising material for future optoelectronic applications in the deep-UV because of its simultaneous direct and indirect emission, absent in AA'-hBN, and for the SHG allowing frequency-doubling up to the deep-UV. Furthermore, this work paves the way for many fundamental questions on the effect of stacking on the physical properties of 2D materials in line with the recent results on twisted bilayer hBN and, more generally, on Moiré materials [17, 91, 92, 112].

General conclusion

In this thesis, the optical properties of hBN monolayers and hBN polytypes have been studied using deep-UV hyperspectral microscopy.

To do so, I have developed an original deep-UV microscope which is an upgraded version of a microscope operating in the UVB spectral range developed by the former PhD student. This microscope features unique performances allowing hyperspectral acquisitions in the deep-UV down to cryogenic temperatures ($\sim$4 K) with a high spatial resolution of $\sim$250 nm. Additionally, the tunability of the light sources in the UVB and UVC spectral ranges enables a broad diversity of possible experiments, such as one- and two-photon photoluminescence (PL) spectroscopy or second-harmonic generation (SHG) spectroscopy, that can be combined to gain better insight about the properties of the samples. Importantly, I have achieved the development of a *Python* software that enables complex and modular hyperspectral data acquisitions as well as a *Python* software dedicated to the exploration of the hyperspectral images.

First, I performed a systematic study of the optical properties of monolayer hBN for both exfoliated and epitaxial hBN monolayers for different conditions of excitation using our deep-UV microscope. Notably, the hyperspectral imaging allowed me to separate the different spectral components that compose the emission spectrum in the deep-UV and study their spatial distribution. I could then isolate and identify the intrinsic emission of exfoliated hBN monolayers which is found at 6.08 eV closed to the energy of the PL doublet measured by *Elias et al.* on epitaxial monolayers [13]. By studying the dependence of the indirect emission with the thickness of hBN in the few-layer regime, I then demonstrated a substantial modification of the intensity ratio of the phonon replicas in indirect bandgap few-layer hBN, where LA/TA phonon replicas decrease with the thickness. However, the origin of the line broadening of the phonon replicas commonly observed in few-layer hBN is still undetermined. Next, I studied two epitaxial samples differing by the hBN coverage and displaying completely different topography in AFM. In these two samples, either a multiplet or a singlet is distinctly observed above 6 eV which I attributed to the coexisting Raman and PL signal, respectively, induced by the quasi-resonant excitation. I then developed a quantitative model based on the linear combination of functions representing the Raman and PL signals in order to perform a quantitative analysis of my results. By fitting at each point of the different maps, I then extracted the PL and Raman contributions as well as the energy and the broadening of the PL lines at each point of the maps. From the

spatial analysis of the PL and Raman contributions in the two epitaxial samples, I concluded on the enhancement of the Raman signal at the HOPG edges while both signals are systematically observed in hBN monolayers. By applying the same model to the PL spectrum recorded in an exfoliated monolayer, I evidenced the presence of a PL doublet at similar energies to the one observed by *Elias et al.* [13]. Finally, the conversion of the PL emission from a singlet in epitaxial monolayers to a doublet in exfoliated monolayer hBN is attributed to the selective excitation induced by the quasi-resonant excitation. This leads me to conclude that the origin of the PL doublet arises from the two direct excitons dX and dX' built from carriers in K and K' valleys, respectively.

Second, I have demonstrated the isolation of a micrometer-sized bernal boron nitride (AB-hBN) polytype intercalated between two larger AA'-hBN crystals which allowed me to study for the first time its optical properties. The identification of the AB stacking has been made from the combination of PL and SHG microscopy recorded over the same area of the crystal where the SHG spatially coincides with the PL signal at ∼6.04 eV. On the one hand, recent theoretical calculations predict a blue-shift of the optical bandgap in AB-hBN compared to AA'-hBN [32]. On the other hand, the observation of SHG is the signature of a non-centrosymmetric polytype like AB-hBN. This leads me to the conclusion that the isolated crystal corresponds to AB-hBN, from which the PL signal at ∼6.04 eV is a specific signature in the deep-UV emission spectrum. I then benefited from the isolation of a pure AB-hBN crystal to study its optical properties both in the deep-UV and UVB spectral ranges. In the deep-UV, I evidenced the simultaneous observation of direct and indirect emissions in AB-hBN. The lines between 5.7 and 6 eV are attributed to the phonon-assisted radiative recombination of the indirect exciton in AB-hBN (iX_{AB}), estimated at ∼6.04 eV. Besides, the narrow line at ∼6.04 eV, although overlapping with iX_{AB}, is rather attributed to the radiative recombination of the direct exciton in AB-hBN (dX_{AB}). These results are in agreement with *ab-initio* calculations of the excitonic dispersion in AB-hBN which predict a quasi-degeneracy of iX_{AB} and dX_{AB} [32]. We then studied the thermal broadening of the direct and indirect transitions in AB-hBN which presents different behaviors. The thermal broadening of the indirect exciton presents a curvature similar to the one of AA'-hBN, characteristics of the slow modulation limit associated to efficient phonon dephasing processes early described in the seminal work of *Toyozawa* [104]. In contrast, the thermal broadening of the direct transition shows the standard curvature of the fast modulation limit of the phonon dephasing processes usually observed in semiconductors [105]. These different behaviors are interpreted by the influence of the strong light-matter coupling, modifying the curvature of the polariton dispersion near the light cone, thus reducing efficient phonon-assisted dephasing processes of the direct transition. Our results provide the first experimental demonstration of the detrimental effect of the light-matter coupling on the phonon dephasing at the origin of the thermal broadening. Finally, I demonstrated the impact of stacking on the deep-level emission in the UVB of the "4.1eV defect" in hBN which is duplicated and globally blue-shifted in AB-hBN. The blue-shift of the deep-level emission is linked to the blue-shift of the bandgap

of AB-hBN, although attenuated due to the Bloch states mixing in the electronic states of the defect. Besides, I suggested the existence of two atomistic configurations of the defect which would be equivalent in AA'-hBN and become inequivalent in AB-hBN leading to a duplication of the deep-level emission. Therefore, the ZPLs in AB-hBN can be used as a specific signature in the UVB range allowing easier optical characterization compared to the deep-UV. Moreover, our work paves the way to the determination of the atomic structure of the "4.1eV defect" in hBN.

Outlook

This thesis paves the way for significant fundamental and technological outlooks. First, the identification of specific optical signatures in the UVB and UVC spectral ranges characteristic of the deep-level and intrinsic emission of AB-hBN, respectively, can be used to monitor the formation of AB-hBN polytypes during the growth of hBN crystals. This would enable a direct, non-destructive, and *in-situ* characterization of the hBN stacking. Additionally, deep-UV microscopy appears as a promising platform to study the microscopic properties of hBN crystals that can be used to understand growth processes. Therefore, a better understanding of the optical properties of hBN polytypes would lead to improvements in the growth of large-area high-quality hBN crystals by monitoring the formation of different polytypes. Nevertheless, while my results on the optical properties of AB-hBN contribute to this goal, complementary investigations on the optical properties of other hBN polytypes are further required. Importantly, significant efforts have to be put into understanding the growth of polytypes in epitaxial hBN layers that could allow a large-scale control of the formation of hBN polytypes to enable tailoring the properties of hBN crystals. This could lead to the large-scale fabrication of hBN crystals with exotic properties such as ferroelectricity and superlubricity [91–93]. The controlled growth of polytypes could also allow tunability of the optical properties of hBN crystals with promising applications for UV optoelectronics. First, the UVB emission from the so-called "4.1eV defect" in hBN could be tuned with the stacking offering potential application for the development of UVB LEDs as well as a potential quantum emitter with tunable emission. Secondly, the intrinsic emission of hBN in the UVC can also be tuned with the stacking which influences both the nature and the energy of the optical bandgap of hBN. High-level control of polytypism in hBN crystals could then lead to the growth of hBN polytype heterostructures allowing the fabrication of quantum wells (QW) and superlattices for the development of hBN-based deep-UV emitters.

Bibliography

[1] N. Atari, H. Mamane, A. Silberbush, N. Zuckerman, M. Mandelboim, et Y. Gerchman. "Disinfection of SARS-CoV-2 by UV-LED 267 nm: comparing different variants." *Scientific Reports*, **13**, 8229 (2023).

[2] V. K. Sharma et H. V. Demir. "Bright Future of Deep-Ultraviolet Photonics: Emerging UVC Chip-Scale Light-Source Technology Platforms, Benchmarking, Challenges, and Outlook for UV Disinfection." *ACS Photonics*, **9**, 1513 (2022).

[3] M. Biasin, *et al.* "UV-C irradiation is highly effective in inactivating SARS-CoV-2 replication." *Scientific Reports*, **11**, 6260 (2021).

[4] M. Raeiszadeh et B. Adeli. "A Critical Review on Ultraviolet Disinfection Systems against COVID-19 Outbreak: Applicability, Validation, and Safety Considerations." *ACS Photonics*, **7**, 2941 (2020).

[5] M. Kneissl, T.-Y. Seong, J. Han, et H. Amano. "The emergence and prospects of deep-ultraviolet light-emitting diode technologies." *Nature Photonics*, **13**, 233 (2019).

[6] K. Watanabe, T. Taniguchi, et H. Kanda. "Direct-bandgap properties and evidence for ultraviolet lasing of hexagonal boron nitride single crystal." *Nature Materials*, **3**, 404 (2004).

[7] G. Cassabois, P. Valvin, et B. Gil. "Hexagonal boron nitride is an indirect bandgap semiconductor." *Nature Photonics*, **10**, 262 (2016).

[8] L. Schué, *et al.* "Bright Luminescence from Indirect and Strongly Bound Excitons in h-BN." *Physical Review Letters*, **122**, 067401 (2019).

[9] B. Gil, G. Cassabois, R. Cusco, G. Fugallo, et L. Artus. "Boron nitride for excitonics, nano photonics, and quantum technologies." *Nanophotonics*, **9**, 3483 (2020).

[10] A. Raja, *et al.* "Coulomb engineering of the bandgap and excitons in two-dimensional materials." *Nature Communications*, **8**, 15251 (2017).

[11] K. F. Mak, C. Lee, J. Hone, J. Shan, et T. F. Heinz. "Atomically Thin MoS 2 : A New Direct-Gap Semiconductor." *Physical Review Letters*, **105**, 136805 (2010).

[12] A. Chaves, *et al.* "Bandgap engineering of two-dimensional semiconductor materials." *npj 2D Materials and Applications*, **4**, 29 (2020).

[13] C. Elias, *et al.* "Direct band-gap crossover in epitaxial monolayer boron nitride." *Nature Communications*, **10**, 2639 (2019).

[14] P. Wang, *et al.* "Scalable Synthesis of Monolayer Hexagonal Boron Nitride on Graphene with Giant Bandgap Renormalization." *Advanced Materials*, **34**, 2201387 (2022).

[15] P. Lechifflart, F. Paleari, et C. Attaccalite. "Excitons under strain: light absorption and emission in strained hexagonal boron nitride." *SciPost Physics*, **12**, 145 (2022). ArXiv:2112.12417 [cond-mat].

[16] Z. Zheng, *et al.* "Unconventional ferroelectricity in moiré heterostructures." *Nature*, **588**, 71 (2020).

[17] E. Y. Andrei, *et al.* "The marvels of moiré materials." *Nature Reviews Materials*, **6**, 201 (2021).

[18] Z. Hennighausen et S. Kar. "Twistronics: a turning point in 2D quantum materials." *Electronic Structure*, **3**, 014004 (2021).

[19] S. Shabani, *et al.* "Deep moiré potentials in twisted transition metal dichalcogenide bilayers." *Nature Physics*, **17**, 720 (2021).

[20] F. Lévy, editor. *Crystallography and Crystal Chemistry of Materials with Layered Structures*. Springer Netherlands, Dordrecht (1976). ISBN 978-94-010-1435-9 978-94-010-1433-5.

[21] A. A. Lebedev, *et al.* "A study of n +-6H/n-3C/p +-6H-SiC heterostructures grown by sublimation epitaxy." *Semiconductors*, **40**, 1398 (2006).

[22] F. Boutaiba, A. Belabbes, M. Ferhat, et F. Bechstedt. "Polytypism in ZnS, ZnSe, and ZnTe: First-principles study." *Physical Review B*, **89**, 245308 (2014).

[23] L. Pachayappan, S. Nagendran, et P. V. Kamath. "Reappraisal of Polytypism in Layered Double Hydroxides: Consequences of Cation Ordering in the Metal Hydroxide Layer." *Crystal Growth & Design*, **17**, 2536 (2017).

[24] Y. Liang, J. Yang, X. Yuan, W. Qiu, Z. Zhong, J. Yang, et W. Zhang. "Polytypism in superhard transition-metal triborides." *Scientific Reports*, **4**, 5063 (2014).

[25] T. Lu, *et al.* "Synthesizability of transition-metal dichalcogenides: a systematic first-principles evaluation." *Materials Futures*, **2**, 015001 (2023).

[26] I. Song, C. Park, et H. C. Choi. "Synthesis and properties of molybdenum disulphide: from bulk to atomic layers." *RSC Advances*, **5**, 7495 (2015).

[27] S. S. Atri, *et al.* "Spontaneous Electric Polarization in Graphene Polytypes."

[28] Y. Shi, *et al.* "Electronic phase separation in multilayer rhombohedral graphite." *Nature*, **584**, 210 (2020).

[29] Y. Henni, *et al.* "Rhombohedral Multilayer Graphene: A Magneto-Raman Scattering Study." *Nano Letters*, **16**, 3710 (2016).

[30] G. Constantinescu, A. Kuc, et T. Heine. "Stacking in Bulk and Bilayer Hexagonal Boron Nitride." *Physical Review Letters*, **111**, 036104 (2013).

[31] N. Ohba, K. Miwa, N. Nagasako, et A. Fukumoto. "First-principles study on structural, dielectric, and dynamical properties for three BN polytypes." *Physical Review B*, **63**, 115207 (2001).

[32] L. Sponza, *et al.* "Direct and indirect excitons in boron nitride polymorphs: a story of atomic configuration and electronic correlation." *Physical Review B*, **98**, 125206 (2018). ArXiv: 1806.06201.

[33] T. Pelini. "Optical properties of point defects in hexagonal boron nitride." page 139.

[34] P. Lechifflart, F. Paleari, D. Sangalli, et C. Attaccalite. "First-principles study of luminescence in hexagonal boron nitride single layer: Exciton-phonon coupling and the role of substrate." *Physical Review Materials*, **7**, 024006 (2023).

[35] K. Watanabe, T. Taniguchi, K. Miya, Y. Sato, K. Nakamura, T. Niiyama, et M. Taniguchi. "Hexagonal boron nitride as a new ultraviolet luminescent material and its application—Fluorescence properties of hBN single-crystal powder." *Diamond and Related Materials*, **20**, 849 (2011).

[36] A. V. Kurdyumov, V. L. Solozhenko, et W. B. Zelyavski. "Lattice Parameters of Boron Nitride Polymorphous Modifications as a Function of Their Crystal-Structure Perfection." *Journal of Applied Crystallography*, **28**, 540 (1995).

[37] L. Xu, *et al.* "High-Yield Synthesis of Rhombohedral Boron Nitride Triangular Nanoplates." *Advanced Materials*, **19**, 2141 (2007).

[38] M. Chubarov, H. Pedersen, H. Högberg, Z. Czigány, M. Garbrecht, et A. Henry. "Polytype Pure sp ^{2} -BN Thin Films As Dictated by the Substrate Crystal Structure." *Chemistry of Materials*, **27**, 1640 (2015).

[39] J. Liu, Y. K. Vohra, J. T. Tarvin, et S. S. Vagarali. "Cubic-to-rhombohedral transformation in boron nitride induced by laser heating: *In situ* Raman-spectroscopy studies." *Physical Review B*, **51**, 8591 (1995).

[40] S. M. Gilbert, *et al.* "Alternative stacking sequences in hexagonal boron nitride." *2D Materials*, **6**, 021006 (2019).

[41] S.-P. Gao. "Crystal structures and band gap characters of h-BN polytypes predicted by the dispersion corrected DFT and GW method." *Solid State Communications*, **152**, 1817 (2012).

[42] F. Bassani et G. P. Parravicini. "Band structure and optical properties of graphite and of the layer compounds GaS and GaSe." *Il Nuovo Cimento B Series 10*, **50**, 95 (1967).

[43] K. H. Michel et B. Verberck. "Phonon dispersions and piezoelectricity in bulk and multilayers of hexagonal boron nitride." *Physical Review B*, **83**, 115328 (2011).

[44] R. V. Gorbachev, *et al.* "Hunting for Monolayer Boron Nitride: Optical and Raman Signatures." *Small*, **7**, 465 (2011).

[45] G. Cassabois, *et al.* "Exciton and Phonon Radiative Linewidths in Monolayer Boron Nitride." *Physical Review X*, **12**, 011057 (2022).

[46] R. Taylor et C. A. Coulson. "Studies in Graphite and Related Compounds III: Electronic Band Structure in Boron Nitride." *Proceedings of the Physical Society. Section A*, **65**, 834 (1952).

[47] E. Doni et G. P. Parravicini. "Energy bands and optical properties of hexagonal boron nitride and graphite." *Il Nuovo Cimento B Series 10*, **64**, 117 (1969).

[48] T. Galvani, *et al.* "Excitons in boron nitride single layer." *Physical Review B*, **94**, 125303 (2016).

[49] D. Wickramaratne, L. Weston, et C. G. Van De Walle. "Monolayer to Bulk Properties of Hexagonal Boron Nitride." *The Journal of Physical Chemistry C*, **122**, 25524 (2018).

[50] J. Koskelo, G. Fugallo, M. Hakala, M. Gatti, F. Sottile, et P. Cudazzo. "Excitons in van der Waals materials: From monolayer to bulk hexagonal boron nitride." *Physical Review B*, **95**, 035125 (2017).

[51] R. J. P. Román, *et al.* "Band gap measurements of monolayer h-BN and insights into carbon-related point defects." *2D Materials*, **8**, 044001 (2021). ArXiv:2107.07950 [cond-mat].

[52] X. Blase, A. Rubio, S. G. Louie, et M. L. Cohen. "Quasiparticle band structure of bulk hexagonal boron nitride and related systems." *Physical Review B*, **51**, 6868 (1995).

[53] F. Paleari, T. Galvani, H. Amara, F. Ducastelle, A. Molina-Sánchez, et L. Wirtz. "Excitons in few-layer hexagonal boron nitride: Davydov splitting and surface localization." (2018). ArXiv:1803.00982 [cond-mat].

[54] C. Elias, *et al.* "Flat Bands and Giant Light-Matter Interaction in Hexagonal Boron Nitride." *Physical Review Letters*, **127**, 137401 (2021).

[55] C. Guo, J. Xu, et Y. Ping. "Substrate effect on excitonic shift and radiative lifetime of two-dimensional materials." *Journal of Physics: Condensed Matter*, **33**, 234001 (2021).

[56] C. Elias. "Optical spectroscopy of hexagonal boron nitride: from bulk to monolayer." page 159.

[57] K. Shima, *et al.* "Cathodoluminescence spectroscopy of monolayer hexagonal boron nitride."

[58] L. Wirtz, A. Marini, et A. Rubio. "Excitons in Boron Nitride Nanotubes: Dimensionality Effects." *Physical Review Letters*, **96**, 126104 (2006).

[59] B. Gil, *et al.* "Polytypes of sp2-Bonded Boron Nitride." *Crystals*, **12**, 782 (2022).

[60] T. Mosuang et J. Lowther. "Relative stability of cubic and different hexagonal forms of boron nitride." *Journal of Physics and Chemistry of Solids*, **63**, 363 (2002).

[61] L. Liu, Y. P. Feng, et Z. X. Shen. "Structural and electronic properties of *h* -BN." *Physical Review B*, **68**, 104102 (2003).

[62] M. L. Hu, J. L. Yin, C. X. Zhang, Z. Yu, et L. Z. Sun. "Electronic structures and optical properties of hexagonal boron nitride under hydrostatic pressures." *Journal of Applied Physics*, **109**, 073708 (2011).

[63] T. Haga, Y. Matsuura, Y. Fujimoto, et S. Saito. "Electronic states and modulation doping of hexagonal boron nitride trilayers." *Physical Review Materials*, **5**, 094003 (2021).

[64] J. Furthmüller, J. Hafner, et G. Kresse. "*Ab initio* calculation of the structural and electronic properties of carbon and boron nitride using ultrasoft pseudopotentials." *Physical Review B*, **50**, 15606 (1994).

[65] K. Albe. "Theoretical study of boron nitride modifications at hydrostatic pressures." *Physical Review B*, **55**, 6203 (1997).

[66] C. F. Klingshirn. *Semiconductor optics*. Advanced texts in physics. Springer, Berlin ; New York (2005). ISBN 978-3-540-21328-4.

[67] R. J. Nemanich, S. A. Solin, et R. M. Martin. "Light scattering study of boron nitride microcrystals." *Physical Review B*, **23**, 6348 (1981).

[68] R. Geick, C. H. Perry, et G. Rupprecht. "Normal Modes in Hexagonal Boron Nitride." *Physical Review*, **146**, 543 (1966).

[69] A. Segura, R. Cuscó, T. Taniguchi, K. Watanabe, G. Cassabois, B. Gil, et L. Artús. "High-Pressure Softening of the Out-of-Plane A $_{2u}$ (Transverse-Optic) Mode of Hexagonal Boron Nitride Induced by Dynamical Buckling." *The Journal of Physical Chemistry C*, **123**, 17491 (2019).

[70] G. Fugallo, *et al.* "Exciton energy-momentum map of hexagonal boron nitride." *Physical Review B*, **92**, 165122 (2015). ArXiv:1508.01769 [cond-mat].

[71] T. Q. P. Vuong, *et al.* "Phonon symmetries in hexagonal boron nitride probed by incoherent light emission." *2D Materials*, **4**, 011004 (2016).

[72] M. Scholz, *et al.* "A bright continuous-wave laser source at 193 nm." *Applied Physics Letters*, **103**, 051114 (2013).

[73] T. Q. P. Vuong, G. Cassabois, P. Valvin, V. Jacques, R. Cuscó, L. Artús, et B. Gil. "Overtones of interlayer shear modes in the phonon-assisted emission spectrum of hexagonal boron nitride." *Physical Review B*, **95**, 045207 (2017).

[74] G. Cassabois, P. Valvin, et B. Gil. "Intervalley scattering in hexagonal boron nitride." *Physical Review B*, **93**, 035207 (2016).

[75] R. Bourrellier, *et al.* "Nanometric Resolved Luminescence in h-BN Flakes: Excitons and Stacking Order." *ACS Photonics*, **1**, 857 (2014).

[76] L. Schué, B. Berini, A. C. Betz, B. Plaçais, F. Ducastelle, J. Barjon, et A. Loiseau. "Dimensionality effects on the luminescence properties of hBN." *Nanoscale*, **8**, 6986 (2016).

[77] K. Watanabe et T. Taniguchi. "Far-UV photoluminescence microscope for impurity domain in hexagonal-boron-nitride single crystals by high-pressure, high-temperature synthesis." *npj 2D Materials and Applications*, **3**, 40 (2019).

[78] R. Ishii, M. Funato, et Y. Kawakami. "Pushing the limits of deep-ultraviolet scanning near-field optical microscopy." *APL Photonics*, **4**, 070801 (2019).

[79] P. Valvin, T. Pelini, G. Cassabois, A. Zobelli, J. Li, J. H. Edgar, et B. Gil. "Deep ultraviolet hyperspectral cryomicroscopy in boron nitride: Photoluminescence in crystals with an ultra-low defect density." *AIP Advances*, **10**, 075025 (2020).

[80] J. M. Binder, *et al.* "Qudi: A modular python suite for experiment control and data processing." *SoftwareX*, **6**, 85 (2017).

[81] M. Amani, *et al.* "Near-unity photoluminescence quantum yield in MoS2." *Science*, **350**, 1065 (2015).

[82] C. M. Chow, *et al.* "Phonon-assisted oscillatory exciton dynamics in monolayer MoSe2." *npj 2D Materials and Applications*, **1**, 33 (2017).

[83] L. Schue. "Propriétés optiques et structurales du nitrure de bore en hybridation sp2: des cristaux massifs aux feuillets atomiques." page 181.

[84] T. Q. P. Vuong, *et al.* "Deep ultraviolet emission in hexagonal boron nitride grown by high-temperature molecular beam epitaxy." *2D Materials*, **4**, 021023 (2017).

[85] A. Summerfield, *et al.* "Moiré-Modulated Conductance of Hexagonal Boron Nitride Tunnel Barriers." *Nano Letters*, **18**, 4241 (2018).

[86] S. Reich, A. C. Ferrari, R. Arenal, A. Loiseau, I. Bello, et J. Robertson. "Resonant Raman scattering in cubic and hexagonal boron nitride." *Physical Review B*, **71**, 205201 (2005).

[87] G. Kern, G. Kresse, et J. Hafner. " ***Ab initio*** calculation of the lattice dynamics and phase diagram of boron nitride." *Physical Review B*, **59**, 8551 (1999).

[88] A. Rousseau, *et al.* "Monolayer Boron Nitride: Hyperspectral Imaging in the Deep Ultraviolet." *Nano Letters*, **21**, 10133 (2021).

[89] R. S. Pease. "An X-ray study of boron nitride." *Acta Crystallographica*, **5**, 356 (1952).

[90] V. Solozhenko. "Thermodynamics of dense boron nitride modifications and a new phase P,T diagram for BN." *Thermochimica Acta*, **218**, 221 (1993).

[91] C. R. Woods. "Charge-polarized interfacial superlattices in marginally twisted hexagonal boron nitride." page 7.

[92] M. Vizner Stern, *et al.* "Interfacial ferroelectricity by van der Waals sliding." *Science*, **372**, 1462 (2021).

[93] K. Yasuda, X. Wang, K. Watanabe, T. Taniguchi, et P. Jarillo-Herrero. "Stacking-engineered ferroelectricity in bilayer boron nitride." *Science*, **372**, 1458 (2021).

[94] T. Hoffman, B. Clubine, Y. Zhang, K. Snow, et J. Edgar. "Optimization of Ni–Cr flux growth for hexagonal boron nitride single crystals." *Journal of Crystal Growth*, **393**, 114 (2014).

[95] S. Liu, *et al.* "Large-Scale Growth of High-Quality Hexagonal Boron Nitride Crystals at Atmospheric Pressure from an Fe–Cr Flux." *Crystal Growth & Design*, **17**, 4932 (2017).

[96] J. Li, *et al.* "Hexagonal Boron Nitride Crystal Growth from Iron, a Single Component Flux." *ACS Nano*, **15**, 7032 (2021).

[97] J. Li, *et al.* "Hexagonal Boron Nitride Single Crystal Growth from Solution with a Temperature Gradient." *Chemistry of Materials*, **32**, 5066 (2020).

[98] S.-B. Song, *et al.* "Deep-ultraviolet electroluminescence and photocurrent generation in graphene/hBN/graphene heterostructures." *Nature Communications*, **12**, 7134 (2021).

[99] T. Q. P. Vuong, G. Cassabois, P. Valvin, S. Liu, J. H. Edgar, et B. Gil. "Exciton-phonon interaction in the strong-coupling regime in hexagonal boron nitride." *Physical Review B*, **95**, 201202 (2017).

[100] R. Cuscó, B. Gil, G. Cassabois, et L. Artús. "Temperature dependence of Raman-active phonons and anharmonic interactions in layered hexagonal BN." *Physical Review B*, **94**, 155435 (2016).

[101] P. Y. Yu et M. Cardona. *Fundamentals of Semiconductors: Physics and Materials Properties*. Graduate Texts in Physics. Springer Berlin Heidelberg, Berlin, Heidelberg (2010). ISBN 978-3-642-00709-5 978-3-642-00710-1.

[102] Y.-N. Xu et W. Y. Ching. "Calculation of ground-state and optical properties of boron nitrides in the hexagonal, cubic, and wurtzite structures." *Physical Review B*, **44**, 7787 (1991).

[103] T. Q. P. Vuong, *et al.* "Isotope engineering of van der Waals interactions in hexagonal boron nitride." *Nature Materials*, **17**, 152 (2018).

[104] Y. Toyozawa. "Theory of Line-Shapes of the Exciton Absorption Bands." *Progress of Theoretical Physics*, **20**, 53 (1958).

[105] S. Rudin, T. L. Reinecke, et B. Segall. "Temperature-dependent exciton linewidths in semiconductors." *Physical Review B*, **42**, 11218 (1990).

[106] T. Vuong, G. Cassabois, P. Valvin, A. Ouerghi, Y. Chassagneux, C. Voisin, et B. Gil. "Phonon-Photon Mapping in a Color Center in Hexagonal Boron Nitride." *Physical Review Letters*, **117**, 097402 (2016).

[107] T. Pelini, *et al.* "Shallow and deep levels in carbon-doped hexagonal boron nitride crystals." *Physical Review Materials*, **3**, 094001 (2019).

[108] S. Li, A. Pershin, G. Thiering, P. Udvarhelyi, et A. Gali. "Ultraviolet Quantum Emitters in Hexagonal Boron Nitride from Carbon Clusters." *The Journal of Physical Chemistry Letters*, **13**, 3150 (2022).

[109] H. Hamdi, G. Thiering, Z. Bodrog, V. Ivády, et A. Gali. "Stone-Wales defects in hexagonal boron nitride as ultraviolet emitters." *npj Computational Materials*, **6**, 178 (2020). ArXiv:2008.06857 [cond-mat, physics:quant-ph].

[110] S. Li, A. Pershin, P. Li, et A. Gali. "Exceptionally strong coupling of defect emission in hexagonal boron nitride to stacking sequences." (2023). ArXiv:2307.10401 [cond-mat, physics:physics, physics:quant-ph].

[111] T. Taniguchi et K. Watanabe. "Synthesis of high-purity boron nitride single crystals under high pressure by using Ba–BN solvent." *Journal of Crystal Growth*, **303**, 525 (2007).

[112] S. Zhang, *et al.* "Nano-spectroscopy of excitons in atomically thin transition metal dichalcogenides." *Nature Communications*, **13**, 542 (2022).

Abstract

In the current context of pandemic crises and the imperative to phase out mercury-based lamps from the market due to their high toxicity, there is an urgent need to develop ultraviolet (UV) emitting devices for effective and harmless bacterial and viral disinfection for humans. Hexagonal boron nitride (hBN) presents itself as a potential candidate for this type of application, emitting at a typical wavelength of 210 nm in the deep UV. hBN is a lamellar material made up of atomic honeycomb layers that are weakly stacked to each other. Like other 2D materials, its lamellar structure offers great versatility, allowing the isolation of a single atomic layer as well as the formation of different stacks, known as polytypes. These structural modifications can affect the optical properties of hBN. However, the optical properties of the hBN monolayer are still poorly understood and have not yet been reported for hBN polytypes due to the difficulty of luminescence microscopy in the deep UV. During my thesis, I developed a hyperspectral photoluminescence (PL) microscope operating in the deep UV at cryogenic temperatures (4 K) to study the optical properties of hBN monolayers and polytypes. In particular, this enabled me to measure the optical properties of an hBN polytype for the first time. My results contribute to a better understanding of the impact of stacking on the optical properties of hBN, which until now had never been demonstrated experimentally.